



**Calhoun: The NPS Institutional Archive**  
**DSpace Repository**

---

Theses and Dissertations

1. Thesis and Dissertation Collection, all items

---

1978

Self generated magnetic fields in  
laser-produced shock waves.

Parlar, Cem Yildirim

Monterey, California. Naval Postgraduate School

---

<http://hdl.handle.net/10945/18541>

---

*Downloaded from NPS Archive: Calhoun*



Calhoun is the Naval Postgraduate School's public access digital repository for research materials and institutional publications created by the NPS community. Calhoun is named for Professor of Mathematics Guy K. Calhoun, NPS's first appointed -- and published -- scholarly author.

**Dudley Knox Library / Naval Postgraduate School**  
**411 Dyer Road / 1 University Circle**  
**Monterey, California USA 93943**

<http://www.nps.edu/library>



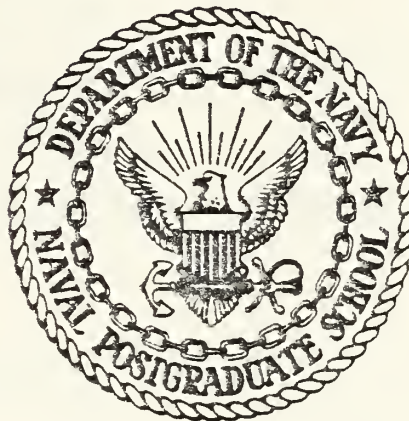
DUDLEY KNOX LIBRARY  
NAVAL POSTGRADUATE SCHOOL  
MONTEREY, CA 93940





# NAVAL POSTGRADUATE SCHOOL

Monterey, California



## THESIS

SELF GENERATED MAGNETIC FIELDS  
IN LASER-PRODUCED SHOCK WAVES

by

Cem Yildirim Parlar

December 1978

Thesis Advisor:

F. Schwirzke

Approved for public release; distribution unlimited.

T187395





REPORT DOCUMENTATION PAGE		READ INSTRUCTIONS BEFORE COMPLETING FORM
1. REPORT NUMBER	2. GOVT ACCESSION NO.	3. RECIPIENT'S CATALOG NUMBER
4. TITLE (and Subtitle) Self Generated Magnetic Fields in Laser-Produced Shock Waves		5. TYPE OF REPORT & PERIOD COVERED Master's Thesis; December 1978
		6. PERFORMING ORG. REPORT NUMBER
7. AUTHOR(s) Cem Yildirim Parlar		8. CONTRACT OR GRANT NUMBER(s)
9. PERFORMING ORGANIZATION NAME AND ADDRESS Naval Postgraduate School Monterey, California 93940		10. PROGRAM ELEMENT, PROJECT, TASK AREA & WORK UNIT NUMBERS
11. CONTROLLING OFFICE NAME AND ADDRESS Naval Postgraduate School Monterey, California 93940		12. REPORT DATE December 1978
		13. NUMBER OF PAGES 107
14. MONITORING AGENCY NAME & ADDRESS (if different from Controlling Office)		15. SECURITY CLASS. (of this report) Unclassified
		15a. DECLASSIFICATION/DOWNGRADING SCHEDULE
16. DISTRIBUTION STATEMENT (of this Report) Approved for public release; distribution unlimited.		
17. DISTRIBUTION STATEMENT (of the abstract entered in Block 20, if different from Report)		
18. SUPPLEMENTARY NOTES		
19. KEY WORDS (Continue on reverse side if necessary and identify by block number) Laser-Produced Shock Waves Self-Generated Magnetic Fields		
20. ABSTRACT (Continue on reverse side if necessary and identify by block number)  The generation of spontaneous magnetic fields in a plasma produced by a 5.0 Joule, 22 nanosecond laser pulse and the generation of the reversed magnetic fields after several hundred nanoseconds due to the interaction between the laser produced plasma and a background plasma was investigated.  The generation of the reversed magnetic fields coincides with the steepening of the expanding plasma front. This steepening		





## ABSTRACT (Cont'd)

is caused by a collisional shock wave which is formed during the interaction of the expanding laser-produced plasma with the photoionized background gas. The analysis of the source term for magnetic field production indicates that the generation of the reverse fields is due to an axial temperature gradient and a radial density gradient. This axial temperature gradient is a result of the heating of the plasma in the collisional shock wave.

The width of the shock was measured to be 0.2 cm. The magnitude of the maximum reverse field was measured at 5.0 Torr ( $H_2$ ) background pressure to be 150 Gauss.



Approved for public release; distribution unlimited.

Self Generated Magnetic Fields  
in Laser-Produced Shock Waves

by

Cem Yıldırım Parlar  
Lieutenant, Turkish Navy  
B.S., Naval Postgraduate School, 1978

Submitted in partial fulfillment of the  
requirements for the degree of

MASTER OF SCIENCE IN PHYSICS

from the  
NAVAL POSTGRADUATE SCHOOL  
December 1978



## ABSTRACT

The generation of spontaneous magnetic fields in a plasma produced by a 5.0 Joule, 22 nanosecond laser pulse and the generation of the reversed magnetic fields after several hundred nanoseconds due to the interaction between the laser produced plasma and a background plasma was investigated.

The generation of the reversed magnetic fields coincides with the steepening of the expanding plasma front. This steepening is caused by a collisional shock wave which is formed during the interaction of the expanding laser-produced plasma with the photoionized background gas. The analysis of the source term for magnetic field production indicates that the generation of the reverse fields is due to an axial temperature gradient and a radial density gradient. This axial temperature gradient is a result of the heating of the plasma in the collisional shock wave.

The width of the shock was measured to be 0.2 cm. The magnitude of the maximum reverse field was measured at 5.0 Torr ( $H_2$ ) background pressure to be 150 Gauss.





## TABLE OF CONTENTS

I.	INTRODUCTION -----	12
II.	PREVIOUS RESEARCH -----	15
III.	THEORY -----	18
	A. LASER PRODUCED PLASMAS -----	18
	B. INTERACTION BETWEEN COUNTERSTREAMING PLASMAS -----	22
	C. INITIAL PRODUCTION OF SPONTANEOUS MAGNETIC FIELDS -----	25
	D. FIELD REVERSAL -----	31
	E. SHOCK WAVES IN A PLASMA -----	33
IV.	EXPERIMENTAL METHODS -----	44
	A. LASER -----	44
	B. LASER MONITORING TECHNIQUES -----	44
	C. TEMPORAL REFERENCE FRAME -----	45
	D. PLASMA CHAMBER -----	46
	E. MAGNETIC PROBES -----	47
	1. Probe Calibration -----	47
	2. Probe Signal Reliability and Sensitivity -----	47
	3. Probe Signal Integration -----	48
	F. ELECTRIC DOUBLE PROBES -----	49
	G. DATA COLLECTION AND ERROR ESTIMATES -----	50
V.	EXPERIMENTAL RESULTS -----	52
VI.	COMPARISON OF THEORY AND EXPERIMENTAL RESULTS --	57
VII.	SUMMARY AND CONCLUSIONS -----	63
VIII.	RECOMMENDATION FOR FURTHER STUDY -----	65



APPENDIX A -----	66
FIGURES -----	67
BIBLIOGRAPHY -----	104
INITIAL DISTRIBUTION LIST -----	107



## LIST OF FIGURES

1.	Cylindrical-polar coordinate system -----	67
2.	Block diagram of experimental layout -----	68
3.	Top view of vacuum chamber -----	69
4.	Circuit layout for magnetic probe calibration -----	70
5.	The electric double probe circuit -----	71
6.	Geometry of a laser produced plasma and the spontaneous magnetic field -----	72
7.	Arrangement of the target, glass plate and probes -----	73
8.	Relation of $\partial B/\partial t$ to the plasma density as a function of time at the point $r = 0.4$ cm, $\theta = 0^\circ$ and $z = 1.0$ cm for a vacuum pressure of $2 \times 10^{-6}$ Torr (plate at $z = 1.15$ cm) -----	74
9.	Relation of $\partial B/\partial t$ to the plasma density as a function of time at the point $r = 0.4$ cm, $\theta = 0^\circ$ and $z = 1.0$ cm for a vacuum pressure of $2 \times 10^{-6}$ Torr (plate at $z = 7.5$ cm) -----	75
10.	Relation of $\partial B/\partial t$ to the plasma density as a function of time at the point $r = 0.4$ cm, $\theta = 0^\circ$ and $z = 1.0$ cm for a background pressure of 0.5 Torr $H_2$ (Plate at $z = 1.15$ cm) -----	76
11.	Relation of $\partial B/\partial t$ to the plasma density as a function of time at the point $r = 0.4$ cm, $\theta = 0^\circ$ and $z = 1.0$ cm for a background pressure of 0.5 Torr $H_2$ (Plate at $z = 7.5$ cm) -----	77
12.	Relation of $\partial B/\partial t$ to the plasma density as a function of time at the point $r = 0.4$ cm, $\theta = 0^\circ$ and $z = 1.0$ cm for a background pressure of 5.0 Torr $H_2$ (plate at $z = 1.15$ cm) -----	78
13.	Relation of $B_\theta$ to the plasma density as a function of time at the point $r = 0.4$ cm, $\theta = 0^\circ$ and $z = 1.0$ cm for a background pressure of 5.0 Torr $H_2$ (plate at $z = 1.15$ cm) -----	79





14.	Relation of $\partial B/\partial t$ to the plasma density as a function of time at the point $r = 0.4$ cm, $\theta = 0^\circ$ and $z = 1.0$ cm for a background pressure of 5.0 Torr $H_2$ (plate at $z = 7.5$ cm) -----	80
15.	Relation of $B_\theta$ to the plasma density as a function of time at the point $r = 0.4$ cm, $\theta = 0^\circ$ and $z = 1.0$ cm for a background pressure of 5.0 Torr $H_2$ (plate at $z = 7.5$ cm) -----	81
16.	Plasma density as a function of time at the point $r = 0.4$ cm, $\theta = 0^\circ$ and $z = 1.0$ cm for a vacuum pressure of $2 \times 10^{-6}$ Torr -----	82
17.	Plasma density as a function of time at the point $r = 0.4$ cm, $\theta = 0^\circ$ and $z = 1.0$ cm for a background pressure of 0.5 Torr $H_2$ -----	83
18.	Plasma density as a function of time at the point $r = 0.4$ cm, $\theta = 0^\circ$ and $z = 1.0$ cm for a background pressure of 5.0 Torr $H_2$ -----	84
19.	Plasma density as a function of time at the point $r = 0.4$ cm, $\theta = 0^\circ$ and $z = 1.0$ cm for two different background pressures. The plate is at $z = 1.15$ cm (0.5 Torr and $2 \times 10^{-6}$ Torr) -----	85
20.	Plasma density as a function of time at the point $r = 0.4$ cm, $\theta = 0^\circ$ and $z = 1.0$ cm for two different background pressures. The plate is at $z = 7.5$ cm (0.5 Torr $H_2$ and $2 \times 10^{-6}$ Torr) -----	86
21.	Plasma density as a function of time at the point $r = 0.4$ cm, $\theta = 0^\circ$ and $z = 1.0$ cm for two different background pressures. The plate is at $z = 1.15$ cm (5.0 Torr $H_2$ and $2 \times 10^{-6}$ Torr) -----	87
22.	Plasma density as a function of time at the point $r = 0.4$ cm, $\theta = 0^\circ$ and $z = 1.0$ cm for two different background pressures. The plate is at $z = 7.5$ cm (5.0 Torr $H_2$ and $2 \times 10^{-6}$ Torr) -----	88
23.	Plasma density as a function of time at the point $r = 0.4$ cm, $\theta = 0^\circ$ and $z = 1.0$ cm for two different background pressures. The plate is at $z = 1.15$ cm (5.0 Torr $H_2$ and 0.5 Torr $H_2$ ) -----	89
24.	Plasma density as a function of time at the point $r = 0.4$ cm, $\theta = 0^\circ$ and $z = 1.0$ cm for two different background pressures. The plate is at $z = 7.5$ cm (5.0 Torr $H_2$ and 0.5 Torr $H_2$ ) -----	90



25.	Magnetic probe signal ( $\partial B/\partial t$ ) as a function of time at the point $r = 0.4$ cm, $\theta = 0^\circ$ and $z = 1.0$ cm for a vacuum pressure of $2 \times 10^{-6}$ Torr -----	91
26.	Magnetic probe signal ( $\partial B/\partial t$ ) as a function of time at the point $r = 0.4$ cm, $\theta = 0^\circ$ and $z = 1.0$ cm for a background pressure of 0.5 Torr $H_2$ -----	92
27.	Magnetic probe signal ( $\partial B/\partial t$ ) as a function of time at the point $r = 0.4$ cm, $\theta = 0^\circ$ and $z = 1.0$ cm for a background pressure of 5.0 Torr $H_2$ -----	93
28.	Magnetic field signal ( $B_\theta$ ) as a function of time at the point $r = 0.4$ cm, $\theta = 0^\circ$ and $z = 1.0$ cm for a background pressure of 5.0 Torr $H_2$ -----	94
29.	Magnetic probe signal ( $\partial B/\partial t$ ) as a function of time at the point $r = 0.4$ cm, $\theta = 0^\circ$ and $z = 1.0$ cm for two different background pressures. The plate is at $z = 1.15$ cm (0.5 Torr $H_2$ and $2 \times 10^{-6}$ Torr) -----	96
30.	Magnetic probe signal ( $\partial B/\partial t$ ) as a function of time at the point $r = 0.4$ cm, $\theta = 0^\circ$ and $z = 1.0$ cm for two different background pressures. The plate is at $z = 7.5$ cm (0.5 Torr $H_2$ and $2 \times 10^{-6}$ Torr) -----	97
31.	Magnetic probe signal ( $\partial B/\partial t$ ) as a function of time at the point $r = 0.4$ cm, $\theta = 0^\circ$ and $z = 1.0$ cm for two different background pressures. The plate is at $z = 1.15$ cm (5.0 Torr $H_2$ and $2 \times 10^{-6}$ Torr) -----	98
32.	Magnetic probe signal ( $\partial B/\partial t$ ) as a function of time at the point $r = 0.4$ cm, $\theta = 0^\circ$ and $z = 1.0$ cm for two different background pressures. The plate is at $z = 7.5$ cm (5.0 Torr $H_2$ and $2 \times 10^{-6}$ Torr) -----	99
33.	Magnetic probe signal ( $\partial B/\partial t$ ) as a function of time at the point $r = 0.4$ cm, $\theta = 0^\circ$ and $z = 1.0$ cm for two different background pressures. The plate is at $z = 1.15$ cm (5.0 Torr $H_2$ and 0.5 Torr $H_2$ ) -----	100



34. Magnetic probe signal ( $\partial B/\partial t$ ) as a function of time at the point  $r = 0.4$  cm,  $\theta = 0^\circ$  and  $z = 1.0$  cm for two different background pressures. The plate is at  $z = 7.5$  cm (5.0 Torr  $H_2$  and 0.5 Torr  $H_2$ ) -----100
35. Plasma density as a function of time at two different points for a background pressure of 5.0 Torr  $H_2$  (Plate at  $z = 1.15$  cm) ---101
36. Plasma density as a function of time at two different points for a background pressure of 5.0 Torr  $H_2$  (Plate at  $z = .75$  cm) ----102
37. Plasma density as a function of time at the point  $r = 0.8$  cm,  $\theta = 0^\circ$  and  $z = 1.0$  cm for a background pressure of 5.0 Torr  $H_2$  -----103





## ACKNOWLEDGEMENT

I would like to acknowledge the valuable technical assistance of Bob Sanders whose rapid response and cooperative attitude made the experiment run smoothly.

Special thanks to Professor Schwirzke for his obvious concern and readiness to discuss ideas and problems.

I would like to thank the Turkish Naval Forces for giving me this opportunity to work in this area.

To my wife, Hülya, I wish to convey my deep appreciation for her patience and understanding.



## I. INTRODUCTION

A dense, energetic plasma can be produced by focusing the pulse from a powerful laser onto a solid target. Associated with this laser-produced plasma (hereafter referred to as laser plasma) spontaneously generated magnetic fields have been reported and investigated [Refs. 22,24]. These investigations imply that spontaneously generated magnetic fields arise generally during the production of a laser plasma. The strength of these fields may vary with target geometry [Ref. 31], background gas pressure [Ref. 3] and amount of energy delivered to the target by the laser. In a computer simulation experiment, Widner [Ref. 30] has observed a spontaneous field intensity of the order of 1 Megagauss.

Stamper et. al. [Ref. 25] have reported spontaneous magnetic fields, of the order of 0.6 Megagauss, generated in the plasma near the focus of a high-irradiance Nd-laser beam. They used a Raman-shifted, three channel Faraday-rotation diagnostic system and observed that the spontaneously produced magnetic fields depend on a variety of experimental parameters, such as target material and geometry, laser irradiance and polarization, focal position, and prepulse effect.

The influence of magnetic fields on laser plasmas is an important topic in laser-fusion research. The presence of



such fields in a plasma has effects on electronic heat conduction and the generation of plasma instabilities.

After laser shut-off, generation of reverse fields has been observed at the front of the expanding plasma for ambient pressures above a certain critical value [Refs. 3 and 21].

This project contains the study of field reversal in an expanding laser plasma.

The spontaneous and reversed fields were detected using magnetic probes (inductive loops). The probe coils consisted of five turns of #40 FormVar copper wire.

The plasma density profiles were diagnosed with electric double probes. The double probes were maintained at a fixed bias of sufficient magnitude (20 volts) to insure collection of saturation ion current. Since the expansion velocity of the laser plasma was greater than the ion thermal velocity, the probe current was proportional to the product of the ion density and the plasma expansion velocity. The expansion velocity was obtainable from the probe signals so that the relative density of the plasma could be calculated.

This thesis is divided into 7 more sections. Section II contains the previous experimental work connected with the field reversal. Section III discusses the basic theory of spontaneous magnetic fields in laser produced plasmas, field reversal and shock waves in a plasma. Section IV contains





the details of the experimental methods. The experimental results are presented in Section V. In Section VI, the experimental results are compared with the theory. Section VII contains the summary and conclusions. Recommendations for further study are contained in Section VIII.



## II. PREVIOUS RESEARCH

During the latter part of 1970, as part of a study of the interaction between a laser plasma and the ambient background plasma, Stamper et. al. [Ref. 24] discovered that magnetic fields were spontaneously generated in the laser plasma. They explained the generation of these fields in terms of thermoelectric currents associated with large temperature and density gradients near the target.

The spontaneous magnetic fields of the order of a kilogauss, were observed with magnetic probes. After this discovery, McKee [Ref. 18] made extensive studies of such fields at the Naval Postgraduate School. During McKee's investigation the following observations were made:

- (1) The maximum fields detected at a fixed position showed a systematic dependence on the ambient gas pressure.
- (2) The fields were symmetric about the target normal.
- (3) After several hundred nanoseconds, a relatively small magnitude field in a direction opposite to the direction of the initial field appeared behind the initial fields. This reverse field appeared sooner in time for a background pressure of 250 m Torr than for 0.1 or 5 m Torr.

McKee developed a model to explain spontaneous magnetic fields. According to McKee's model: If a background plasma is present, the expanding laser plasma will couple to it. If the density of the background plasma is high



enough so that the mean free path for binary collisions between the laser plasma ions and the background plasma ions is smaller than the dimension of the laser plasma, the coupling will be collisional in nature. At lower background pressures collisionless coupling will arise because the presence of the spontaneously generated magnetic field at the front of the laser plasma will lead to coupling via the ion-ion two stream instability in the presence of a magnetic field. As a result of the coupling ambient plasma will be swept-up at the front of the expanding plasma and a density shell will form. The shell contains a density gradient in the z-direction (see Figure 1); then field generation can occur in the density shell if a radial temperature gradient arises (see Section III for details).

After McKee, Bird developed another model (interaction model) to explain the pressure dependence of spontaneous magnetic fields. This model attributes the increase in the magnitude of the initial spontaneous magnetic fields with increasing background gas pressure, to the interaction which occurs between the laser plasma and the ambient background plasma. The interaction increases the axial density gradients of the front of the expanding plasma and this, in turn, increases the rate at which spontaneous magnetic fields are generated in the interaction region.

During Bird's investigation no density shell was detected. Also the shell model could not explain the field reversal.



The following observations on reverse field generation have been reported by Bird:

(1) Field reversal is coincident with a strong interaction between the laser plasma and the background plasma as is evidenced by a steepening and slowing of the front of the expanding plasma.

(2) The onset of field reversal occurs at the front of the expanding laser plasma and it occurs earlier in space and time at higher pressures.

(3) Reverse field can be produced long after laser shut-off if the laser plasma encounters a barrier.

(4) Reverse field is initially produced at the front of the laser plasma streaming into a background of  $H_2$  at pressures above 450 m Torr before any significant pile-up of the laser plasma has occurred. This narrow component of reverse field appeared to be generated in the swept-up hydrogen background plasma and it was followed by the appearance of a broad component of reverse field as the plasma front steepens and slows down due to the interaction between the laser plasma piston and the background.

These results suggest that the generation of the reverse magnetic fields can be explained by formation of a shock wave driven by the expanding laser plasma piston. Such a shock wave compresses and heats the plasma. The formation and the effects of the shock waves in a plasma are discussed in the following section.





### III. THEORY

#### A. LASER PRODUCED PLASMAS

The production of plasma by irradiation of a solid target was first treated theoretically by Basov and Krokhin [Ref. 1].

The plasma is created by heating, vaporization and ionization of the target material. The overdense plasma ( $n_e > n_c$ )<sup>1</sup> at the surface of the target expands until the electron density in the front drops below the critical density  $n_c$ . Strong absorption occurs when the density is near the critical density  $n_c$  and the plasma is heated to a high temperature and the pressure gradient accelerates the plasma. After the laser shut-off, the plasma front expands at a constant velocity. Thus, three distinct states can be observed during the course of the expansion of the laser plasma.

When the expansion is into an ambient background gas rather than into vacuum, the last stage looks quite different.

---

<sup>1</sup>The critical density  $n_c$  for the laser plasma is the density at which the electron plasma frequency is equal to the frequency of laser radiation ( $n_c = \omega^2 m_e \epsilon_0 / e^2$ ). At electron densities above this critical value, the laser plasma reflects most of the incident radiation. The critical density for 1.06  $\mu\text{m}$  radiation is about  $10^{21} \text{ cm}^{-3}$ .



At this stage, for a background gas pressure greater than 0.2 Torr, Bobin et. al. [Ref. 2] observed a luminous sheet ahead of the expanding plasma. This luminous sheet lasted more than 150 nsec after the laser pulse peak value. Its velocity decreased with time. The authors attributed the origin of the luminous sheet to a shock wave driven by the plasma acting as a piston, because their observed time evolution of the luminous front agreed both qualitatively and quantitatively with a simple shock wave model.

A one-dimensional, simplified model treating the expansion of the laser plasma into vacuum has been given by Ready [Ref. 20]. In this treatment it is assumed that:

- (1) The plasma expands in the z-direction.
- (2) Incident radiation is absorbed via the inverse Bremsstrahlung process (free-free absorption by electrons in the laser plasma.
- (3) The target is initially a cold fully ionized plasma.
- (4) Radiation losses can be neglected.
- (5) The electrons and ions have a common temperature.<sup>2</sup>
- (6) Temperature is independent of position.

---

<sup>2</sup>The equipartition time for transfer of absorbed energy from electrons to ions can be approximated by

$$\tau_{ei}^{\epsilon} \approx 25 \left( \frac{m_i}{m_p} \right) T_e^{3/2} (^{\circ}K) [\eta_c (\text{cm}^{-3}) Z]^{-1}$$

where  $m_i$  is the ion mass and  $m_p$  is the proton mass. For  $\eta = 10^{21}$  and  $T_e = 100$  ev,  $\tau_{ei}^{\epsilon} \lesssim 1$  nsec.



(7) The plasma expansion velocity is of the form

$$v = \frac{dz}{dt} \left( \frac{z}{Z} \right)$$

physically, the pressure gradients within the laser plasma are driving the expansion. The form of the pressure variation can be approximated by

$$P = P_s \left( 1 - \frac{z}{Z} \right) \quad z \leq Z$$

where  $P_s$  is the pressure near the surface of the target, and  $Z$  is the distance of the plasma front from the target surface.

The temperature of the plasma can be determined by equating the rate at which the laser beam deposits energy in the plasma, to the rate of change of plasma thermal energy plus the rate at which work  $W$  is done by the plasma. For one dimensional plasma of area  $A$ , expanding in the  $z$ -direction this gives:

$$\frac{1}{A} \frac{dW}{dz} = \frac{1}{2} \frac{d}{dt} (\eta_e + \eta_i) kT - \frac{\partial P}{\partial z} \cdot \frac{dz}{dt} \quad (1)$$

From the plasma equation of state:

$$P = (\eta_i + \eta_e) kT \quad (2)$$

one can obtain the variations of electron and ion densities:



$$\eta_i = \eta_{is} (1 - \frac{z}{Z}) ; \quad \eta_e = \eta_{es} (1 - \frac{z}{Z}) \quad (3)$$

where  $\eta_{is}$  and  $\eta_{es}$  are the ion and electron densities at the target surface. The work done by the plasma in the expansion increases the plasma kinetic energy so that:

$$- \frac{\partial P}{\partial z} \cdot \frac{dz}{dt} = \frac{d}{dt} \left[ \frac{1}{2} (\eta_i m_i + \eta_e m_e) \left( \frac{dz}{dt} \right)^2 \right] \quad (4)$$

By integrating Equations (1) and (4) from zero to  $Z$  and the result,

$$N = A \int_0^Z \eta_s (1 - \frac{z}{Z}) dz = A \eta_s Z/2 ,$$

where  $N$  is the total number of ions or electrons in the plasma and  $\eta_s$  is the corresponding number density at the target surface, Ready obtained the equations

$$T = \left[ \frac{(N_i m_i + N_e m_e) Z}{6K(N_i + N_e)} \right] \cdot \frac{d^2 z}{dt^2} \quad (5)$$

$$\frac{d^3 z}{dt^3} = [24(N_i m_i + N_e m_e)] W \quad (6)$$

These two coupled equations were solved numerically by McKee for the conditions of this experiment. The maximum temperature obtained was of the order of 100 eV and this maximum occurred a few nanoseconds after the arrival of the maximum laser intensity at the target.





In the above treatment, it was assumed that the expansion of the plasma is into a vacuum. The presence of a background gas (pressures above 1 m Torr) influences the expansion dynamics.

#### B. INTERACTION BETWEEN COUNTERSTREAMING PLASMAS

The optical radiation from a dense, hot laser plasma is known to be rich in the far ultraviolet and near x-ray regions of spectrum. Line radiation and Bremsstrahlung radiation from a plasma of  $T = 100$  eV is energetically capable of ionizing an ambient background gas.

Koopman [Ref. 16] has investigated the photoionization produced from a plane copper target by an 8-Joule, 20 nsec laser pulse at  $6943 \text{ \AA}$  from a Ruby laser. He found that the ambient gas was almost completely ionized to distances of the order of a centimeter for a background gas pressure of the order of 0.2 Torr and at large radii the degree of photoionization fell as  $r^{-2}$ . Total optical energy emitted between 1000-2000  $\text{\AA}$  was estimated as approximately  $1 \pm 0.5$  Joule. Therefore, when a laser plasma expands into a photoionized ambient background gas, plasma-plasma interaction must be considered on the expansion dynamics.

According to Dean [Ref. 7] during the period of the laser irradiation of the target (early time), the dynamics of the laser plasma expansion corresponds to the propagation of a radiation-driven detonation wave. After the end of the laser pulse (late time) the plasma expands as a blast



wave. This model assumes that at early times of the expansion phase, there is momentum transfer between the expanding front and the ambient background plasma and that as the front propagates into the background plasma, further energy from the laser is absorbed behind the front in which the density is near the critical density and is transported to the front by electron heat conduction. After the end of the laser pulse, all the momentum in the driving laser plasma piston is assumed transferred to the swept-up background plasma which propagates as a blast wave.

Hall [Ref. 12] investigated the dynamics of the expansion of the laser plasma into an ambient background of argon. During his investigation, a 0.5 Joule, 20 nsec Ruby laser was used. The target was a Tantalum slab. Using an image-converter camera and double probes for diagnostics, he found that the late time expansion dynamics of the laser plasma could be explained by blast wave theory.

Koopman [Ref. 16] has suggested that the observed momentum coupling is the result of multi-coulomb collisions occurring between particles of the two plasmas. If a strong momentum transfer interaction occurs, one would expect "snowplowing" or displacement of the ambient plasma by the leading edge of the laser plasma piston, with a corresponding pile-up of piston plasma behind the interface between the laser plasma and the background plasma. The ambient and piston plasmas would be intermixed in the region of



interface, that is, the model is one in which the background plasma is "captured" at the front of the expanding plasma, increasing the total mass of the streaming plasma and, by conservation of momentum decreasing the expansion velocity.

A one dimensional expansion model can be justified on the basis of the following considerations. At the target surface the laser beam diameter is about 1.5 mm and the laser radiation is absorbed within a distance of the order of 0.01-0.1 mm from the target [Ref. 20]. Therefore, the ablated target material initially will have larger dimensions in the radial direction than in the axial direction. Since the expansion of the laser plasma is driven by pressure gradients;

$$|(\nabla P)_z| \sim \frac{P}{\delta_z} \quad \text{and} \quad |(\nabla P)_r| \sim \frac{P}{\delta_r}$$

from the above discussion,  $\delta_r \gg \delta_z$ , therefore

$|(\nabla P)_z| \gg |(\nabla P)_r|$  where  $\delta_r$  and  $\delta_z$  are characteristic radial and axial scale distances. From the above inequality, a one dimensional laser plasma expansion can be approximated.

When the laser plasma expands into an ambient background plasma, the axial position of the expanding front will be governed by the interaction between the two plasmas. An empirical expression for the late time (after laser shut-off) dependence of the axial position of the plasma front on time and on the ambient (nitrogen) plasma density,  $\rho_0$ ,



is given by Bird [Ref. 3]:

$$z \propto \left(\frac{1}{\rho_0}\right)^{0.1} t^{0.5} \quad (7)$$

### C. INITIAL PRODUCTION OF SPONTANEOUS MAGNETIC FIELDS

In the presence of electric and magnetic fields, the equation of motion for the electron fluid is given by generalized Ohm's law.

$$n_e m_e \left[ \frac{\partial \mathbf{V}_e}{\partial t} + (\mathbf{V}_e \cdot \nabla) \mathbf{V}_e \right] = -en_e [E + \mathbf{V}_e \times \mathbf{B}] - \nabla \cdot \bar{\mathbf{P}}_e + \mathbf{P}_{ei} \quad (8)$$

where  $\mathbf{V}_e(r,t)$  is the fluid velocity of electrons,  $E(r,t)$  and  $\mathbf{B}(r,t)$  are the averaged electric and magnetic fields,  $\bar{\mathbf{P}}_e$  is the kinetic stress tensor and  $\mathbf{P}_{ei}$  represents the collisional momentum transfer between electrons and ions per unit volume and unit time.

If one assumes that the electron-electron collision time  $\tau_{ee}$  is much less than the characteristic time for field production which is of the order of duration of the laser pulse, then  $\nabla \cdot \bar{\mathbf{P}}_e$  reduces to the electron pressure gradient,  $\nabla P_e$ . If the macroscopic flow velocity of the electron fluid element is small compared to the random thermal velocity of the electrons then the  $(\mathbf{V}_e \cdot \nabla) \mathbf{V}_e$  term can be neglected. For the aluminum laser plasma, the expansion velocity of the front is of the order of  $\sim 10^7$  cm/sec [Ref. 5]. If one assumes an electron temperature of 100 eV,





then

$$\frac{|v_e|}{[kT_e/m_e]^{1/2}} \sim 0.01 .$$

Therefore the above approximation is justified.

If the frequencies of interest are much less than the electron plasma frequency, i.e.,  $\omega \ll \omega_{pe}$  the electrons can be considered massless and react instantaneously to applied fields.

$P_{ei}$  can be approximated by the resistive drag term,  $\frac{\eta_e e J}{\sigma}$ , where  $\sigma$  is the conductivity of plasma. Finally, eq. (8) can be written

$$E = \frac{J}{\sigma} - v_e \times B - \frac{1}{\eta_e e} \nabla P_e \quad (9)$$

By taking the curl of E and using the Maxwell equations, eq. (9) becomes

$$-\nabla \times E = \frac{\partial B}{\partial t} = -\frac{1}{\sigma} \nabla \times J + \nabla \times (v_e \times B) + \nabla \times \frac{1}{\eta_e e} \nabla P_e \quad (10)$$

Also, from the Maxwell equations,

$$\nabla \times B = \mu_0 J + \frac{1}{c^2} \frac{\partial E}{\partial t} \quad (11)$$

The ratio of the two terms on the right hand side of eq. (11) is of the order



$$\frac{\frac{1}{c^2} \dot{E}}{\mu_0 J} \approx \frac{\frac{1}{c^2} \frac{E}{\tau_0}}{\mu_0 \sigma E}, \quad (\dot{E} = \frac{\partial E}{\partial t}) \quad (12)$$

where  $\tau_0$  is the duration of the laser pulse ( $\tau_0 \approx 5 \times 10^{-8}$  sec) for all situations of interest  $\sigma > 1$  mho. Therefore, eq. (12) becomes:

$$\frac{1}{c^2 \mu_0 \sigma \tau_0} = \frac{\epsilon_0}{\sigma \tau_0} < \frac{\epsilon_0}{\tau_0} < \frac{10^{-11}}{\tau_0} < 10^{-4} \ll 1$$

The above inequality shows that

$$\frac{\frac{1}{c^2} \cdot \frac{\partial E}{\partial t}}{\mu_0 J} \ll 1$$

i.e., the displacement current can be neglected in comparison to the conduction current. In doing so, equation (11) becomes

$$\nabla \times B = \mu_0 J \quad (13)$$

using eq. (13), the first term in eq. (10) becomes

$$-\frac{1}{\sigma} \nabla \times J = -\frac{1}{\mu_0 \sigma} \nabla \times (\nabla \times B) = -\frac{1}{\mu_0 \sigma} [\nabla (\nabla \cdot B) - \nabla^2 B] \quad (13)$$

since



$$\nabla \cdot \mathbf{B} = 0, \quad -\frac{1}{\sigma} \nabla \times \mathbf{J} = \frac{1}{\mu_0 \sigma} \nabla^2 \mathbf{B} \quad (14)$$

The third term in eq. (10) can be written:

$$\begin{aligned} \nabla \times \frac{1}{\eta_e} \nabla P_e &= \nabla \times \frac{1}{\eta_e} \nabla (\eta_e k T_e) = \nabla \times \left( \frac{k}{e} \nabla T_e + \frac{k T_e}{\eta_e} \nabla \eta_e \right) \\ &= \nabla \times \left( \frac{k T_e}{\eta_e} \nabla \eta_e \right) \end{aligned} \quad (15)$$

The density gradient is a vector;  $\frac{\nabla \eta_e}{\eta_e} \equiv \mathbf{A}$  but the temperature is a scalar quantity;  $\frac{k T_e}{e} \equiv \phi$  then, using the vector identity;

$$\nabla \times (\phi \mathbf{A}) = \phi \nabla \times \mathbf{A} + (\nabla \phi) \times \mathbf{A} \quad (16)$$

Eq. (15) becomes:

$$\nabla \times \left( \frac{k T_e}{\eta_e} \nabla \eta_e \right) = \frac{k}{e} \nabla T_e \times \frac{1}{\eta_e} \nabla \eta_e \quad (17)$$

putting all terms in their final form together, eq. (10) becomes

$$\frac{\partial \mathbf{B}}{\partial t} = \frac{1}{\mu_0 \sigma} \nabla^2 \mathbf{B} + \nabla \times (\mathbf{V}_e \times \mathbf{B}) + \left[ \left( \frac{k}{e} \nabla T_e \right) \times \left( \frac{1}{\eta_e} \nabla \eta_e \right) \right] \quad (18)$$

The first two terms on the right hand side of eq. (18) are the diffusion and convection terms. There is no external magnetic field applied, i.e., initially  $\mathbf{B} = 0$ . Therefore the generation of an initial magnetic field requires that



the last term, the thermal source term (S) be non-zero due to non-parallel temperature and density gradients.

The initial configuration of magnetic field will decay away in a diffusion time  $\tau$  [Ref. 14],

$$\tau = \frac{4\pi\sigma L^2}{c^2} \quad (19)$$

where  $L$  is a length, characteristic of the spatial variation of  $B$ . For times short compared to the diffusion time or, in other words, when the conductivity is so large that the first term in eq. (18) can be neglected, equation (18) can be reduced to:

$$\frac{\partial B}{\partial t} = \nabla \times (V_e \times B) + \left( \frac{\nabla kT_e}{e} \right) \times \left( \frac{\nabla \eta_e}{\eta_e} \right) \quad (20)$$

This equation expresses the fact that the rate at which the fields vary in a region, depends on the rate at which the fields are created in the region and the rate at which the field flows in or out of the region.

For adiabatic expansion of the electrons,  $PV^\gamma = \text{const.}$  or  $\eta_e kT_e \left( \frac{M_e}{m_e \eta_e} \right)^\gamma = \text{const.}$  (where  $M_e$  is the total electron mass in a given volume  $V$ ) or  $kT_e \eta_e^{1-\gamma} = \text{const.}$  and the source term vanishes ( $\nabla T_e \times \nabla \eta_e \propto \nabla \eta_e \times \nabla \eta_e = 0$ ). Thus, non-adiabatic conditions are necessary for the generation of magnetic fields by the thermal source term.

If the laser energy is supplied to the electrons at a sufficiently high rate, then the magnetic source term is





non-zero in the resulting non-adiabatic state. Stamper [Ref. 26] analyzed the problem by means of the electron heat equation.

$$\frac{dW_H}{dt} = \frac{\eta k}{\gamma-1} \cdot \frac{dT}{dt} - k T \frac{d\eta}{dt} \quad (21)$$

where  $W_H$  is the energy supplied to the electrons per unit time. The first term on the right hand side of equation (21)  $\frac{\eta k}{\gamma-1} \cdot \frac{dT}{dt} = \frac{dW_I}{dt}$  where  $W_I$  is the internal energy and the second term on the right hand side of equation (21)

$kT \frac{d\eta}{dt} = \frac{dW_W}{dt}$  where  $W_W$  is the work done by the electrons.

According to Stamper, the ratio  $\dot{W}_H/\dot{W}_I$  is the measure of non-adiabatic conditions. Stamper approximated  $W_H$  by the product of the absorption coefficient  $k_\nu$  ( $\text{cm}^{-1}$ ) and the radiation intensity  $I$  ( $\text{Watt}/\text{cm}^2$ ), while  $W_I$  was approximated by  $\frac{\eta_e kT}{\tau_h}$  where  $\tau_h$  is an average electron heating time. If one assumes  $k_\nu$  is due to inverse Bremsstrahlung absorption, in the underdense region, that gives:

$$\frac{\dot{W}_H}{\dot{W}_I} = \frac{\tau_{ei}^\epsilon}{\tau_{ei}} \cdot \frac{I/c\bar{n}}{\eta_e kT} \quad (22)$$

where  $T_{ei}$  is the electron-ion collision time,<sup>4</sup>  $\bar{n}$  is the

---


$$^4 \tau_{ei} = \frac{2.7 \times 10^{-2}}{\eta_i (\text{cm}^{-3})} \cdot T_e^{3/2} (^\circ\text{K}) \text{ for } \eta_i \sim 10^{21} \text{ cm}^{-3}$$

and  $T_e \sim 100 \text{ eV}$ . From footnote (2),  $\tau_{ei} \sim 3 \times 10^{-14} \text{ sec}$ .  
 $\tau_{ei}^\epsilon \sim 8.1 \times 10^{-10} \text{ sec}$ , and the ratio  $\tau_{ei}^\epsilon/\tau_{ei} \approx 9.25 \times 10^2 \frac{m_i}{m_p} \gg 1$ .



index of refraction of plasma ( $\bar{n} \sim 1$ ). Actually near the cut-off, the index of refraction goes to zero, thus the ratio  $\dot{W}_H/\dot{W}_I \gg 1$  and the plasma appears non-adiabatic. During the time the plasma is absorbing the laser radiation, for the conditions of this investigation, the ratio  $\dot{W}_H/\dot{W}_I$  is of the order of one and the plasma appears non-adiabatic. But if  $\dot{W}_H \ll \dot{W}_I$  and  $\dot{W}_W$  then the plasma appears adiabatic.

The direction of magnetic field is determined by the geometry of the laser plasma. At early times, the laser plasma, as justified before, will expand in the axial direction and create an axial density gradient. The temperature gradient is due to the finite radial extent of the laser beam and is in the negative radial direction. The cross product of these two gradients will generate azimuthal and axisymmetric magnetic fields [Fig. 6] as observed.

#### D. FIELD REVERSAL

At later times, after cessation of the laser pulse, the gradients become smaller and field production becomes insignificant. However if the laser plasma expands into a background plasma of sufficient density, shock heating at the front will produce an axial temperature gradient [Ref. 21]. Since a radial density gradient always exists in the plume-shaped laser plasma, magnetic field in a direction opposite to the initial field will be generated. The equation describing this field is:

$$\frac{\partial B}{\partial t} = \left( \nabla_z \frac{kT_e}{e} \right) \times \left( \frac{\nabla_r \eta_e}{\eta_e} \right) \quad (23)$$



Schwirzke [Ref. 21] and Bird [Ref. 3] observed this magnetic field reversal several hundred nanoseconds after laser shut-off. The production of reverse field at the front of the laser plasma requires that the ratio:

$$\frac{|\nabla_z T_e| |\nabla_r \eta_e|}{|\nabla_r T_e| |\nabla_z \eta_e|}$$

be greater than one.

The gradients in this ratio can be approximated by:

$$\nabla_z T_e \approx \frac{T_e}{\delta_{zT}}, \quad \nabla_z \eta_e \approx \frac{\eta_e}{\delta_{z\eta}}, \quad \nabla_r T_e \approx \frac{T_e}{\delta_{rT}}, \quad \nabla_r \eta_e \approx \frac{\eta_e}{\delta_{r\eta}}$$

where the  $\delta$ 's are the characteristic gradient scale lengths. The ratio becomes  $\delta_{z\eta} \cdot \delta_{rT} / \delta_{zT} \cdot \delta_{r\eta}$ . For a one dimensional adiabatic compression or shock compression in the z-direction,  $\delta_{zT} \approx \delta_{z\eta}$  and  $\delta_{zT} \ll \delta_{rT}$ . The large electron heat conduction provides that  $\delta_{rT} > \delta_{r\eta}$  and thus the ratio becomes greater than one ie., reverse field production is possible under these conditions.

The production of reverse field appears to be a consequence of the interaction between the laser plasma and the ambient background plasma. The interaction results in slowing down and a steepening of the front of the laser plasma (pile-up).

Equation (23) predicts that the field reversal will occur sooner and grow to a larger magnitude as the background pressure increases. Bird [Ref. 5] justified this prediction



and also observed that

(1) The mechanism for production of reverse fields is "turned-on" sooner at higher background pressures.

(2) Field reversal is coincident with a strong interaction between the laser plasma and the ambient background as is evidenced by a steepening and slowing of the front of the expanding plasma.

The electron temperature required to produce a given field reversal can easily be estimated by dimensional analysis of eq. (23). From that equation

$$\frac{K T_e}{e} \approx \frac{B_{\theta \max} \cdot \delta_r \cdot \delta_z}{\tau} \quad (24)$$

where  $\delta_r$  and  $\delta_z$  are radial and axial characteristic scale lengths and  $\tau$  is the characteristic time for reverse magnetic field production. Bird estimated the required temperature to be of the order of 1 eV for the parameters of his investigation which were similar to the ones of the present investigation.

#### E. SHOCK WAVES IN A PLASMA

If a large concentration of energy in a continuous medium is suddenly released, it will spread into the medium and at its forefront will be a shock wave. A shock wave is a sudden but continuous change in the state of medium, heats, compresses and accelerates the medium through which it





propagates. The shock wave may propagate through a plasma.

The normal process of shock formation is the pressure dependence of wave velocity, so that a finite amplitude disturbance with increasing pressure steepens as the higher pressure portions move faster than the smaller ones in front. In order to obtain a steady profile wave, some mechanism must exist to limit the steepening. This limitation on steepening can be provided by either dissipation or dispersion. A steady state shock occurs when a diffusion process balances the steepening. Jump conditions are then obtainable from the conservation of mass, momentum and energy. In gas dynamics, the flows are properly described by the Navier-Stokes equations. Any shock wave present in the flow must therefore also be contained in the solutions of the Navier-Stokes equations, under appropriate initial and boundary conditions [Ref. 3]. However if the thickness of the shock wave becomes so small as to be comparable to the mean free path, the Navier-Stokes equations become invalid in describing the flow in the shock. One must then use the Boltzmann equation or similar kinetic equations for the description of the shock structure.

The basic features of the shock structure in a plasma are related to the slow character of the energy exchange between ions and electrons and to the high electron mobility, as a result of which the electron heat conduction greatly



exceeds the ion heat conduction. Maxwellian distributions in the electron and ion fluids are established quite rapidly, in a time of the order of the time between particle collisions [Ref. 33]. On the other hand the equilibration of the temperatures of ion and electron fluids takes place much more slowly, because of the large difference between the electron and ion masses. This relaxation process determines the shock front thickness in a plasma.

A qualitative discussion of the consequences of the low rate of energy exchange between electrons and ions is given by Zel'dovich and Raizer [Ref. 33]. In this simplified discussion it is assumed that:

(1) electron heat conduction does not differ from ion heat conduction

(2) ionization does not take place in the shock wave; the wave is propagated through a gas which is already ionized

In a reference frame moving with the wave a considerable part of the kinetic energy of the gas entering the compression shock, is irreversibly converted into heat through the action of ion viscous forces. The increase in ion temperature across the compression shock is of the order  $\Delta T_i \sim \frac{m_i V^2}{k}$  where  $V$  is the velocity of the incident gas, equal to the shock front velocity and  $m_i$  is the mass of an ion. The thickness of the viscous shock is determined by the time between ion collisions,  $\tau_i$ ; it is of the order of



an ion-ion collision mean free path  $\ell_i \sim \bar{v}_{th} \tau_i$  where  $v_{th}$  is the thermal velocity of the ions in the compression shock. During the compression time  $\tau_i$  the ions do not succeed in transferring any appreciable thermal energy to the electrons, since the characteristic exchange time  $\tau_{ei}^\varepsilon \sim (\frac{m_i}{m_e})^{1/2} \tau_i$  is very large compared to the ion collision time  $\tau_i$ .

The increase in electron temperature across the shock due to the conversion of the kinetic energy of the electrons into heat through the action of electron viscous forces is negligibly small. It is of the order of  $\Delta T_e \sim \frac{mev^2}{k}$ , that is smaller by a factor of  $m_e/m_i$  than  $\Delta T_i$ . The electron gas in the compression shock is heated by some other process. Since the dissipation of energy due to electron viscous force is very small, Zel'dovich and Raizer [Ref. 33] suggested that the compression and heating of the electron gas in the compression shock is adiabatic:

$$\frac{T_{e2}}{T_{e1}} = \left(\frac{\rho_2}{\rho_1}\right)^{\gamma-1} \quad (25)$$

where  $T_{e1}$  and  $T_{e2}$  are the electron temperatures in State I and State II,  $\rho_1$  and  $\rho_2$  are the electron densities in State I and State II and  $\gamma$  is the ratio of specific heats. For a strong shock wave, the ratio  $\frac{\rho_2}{\rho_1}$  is of the order of 4. Thus  $\frac{T_{e2}}{T_{e1}} \sim 2.5$  for  $\gamma = 1.4$ . Therefore in a strong shock wave propagating through a plasma with equal ion and electron



temperatures, behind the shock there is considerable difference in the temperatures of the two gases. After a small portion has undergone the shock compression it begins to transfer thermal energy from the ions to the electrons and this leads to an equilibration of the temperatures in a time of the order of the energy exchange time  $\tau_{ei}^{\epsilon}$ . The final temperature  $T_1$  ( $= T_e = T_i$ ) is determined by the general equations of conservation for shock fronts. The thickness of the relaxation region behind the shock in which plasma approaches equilibrium ( $T_e = T_i = T_1$ ) is of the order of

$$\Delta x \sim v_1 \tau_{ei}^{\epsilon} \quad \text{where} \quad v_1 = \frac{\rho_1}{\rho_2} v.$$

Jaffrin and Probstein [Ref. 15] investigated the structure of a one dimensional shock wave in a fully ionized plasma consisting of electrons and singly ionized ions in the absence of any applied external electric or magnetic fields.

The analysis of the shock structure is based on a two-fluid continuum approach in which they took as a "model" the Navier-Stokes equation, including the electric field and transfer terms. In so doing the overall width of the shock transition region turns out to be considerably larger than the characteristic mean free path. They found that

(1) for mach number  $M < 1.12$  (weak shock) the shock profile is monotonic, with the shock thickness of the order of  $\ell_2/\epsilon$  where  $\ell_2$  is the down stream (behind shock) mean free





path of ion-ion collisions and  $\epsilon = (\frac{m_e}{m_i})^{1/2}$ . The important dissipative mechanisms are electron thermal conduction and the energy exchange between ions and electrons.

(2)  $M > 1.12$  (moderate to strong shocks). There is still a thermal shock layer whose approximate thickness is  $\ell_2/\epsilon$ . In this layer the electron temperature increases and approaches its downstream value while the ion temperature and velocity changes are relatively small. However, imbedded in this first layer there exists a second inner shock whose thickness is of the order of the downstream ion-ion collision mean free path  $\ell_2$ . In this second layer, the dissipations are due to the ion viscosity and thermal conduction. The heating and compression of ions occur mainly in this second shock layer. However, because of the ions' much heavier mass, the ions do not have time to exchange energy with the electrons in a few mean free paths and the electron temperature is essentially unaffected. The ion and electron temperatures then equilibrate in the downstream continuation of the thermal layer. The thickness of this downstream layer is of the order of  $\ell_2/\epsilon$ .

(3) Debye length of the order of the mean free path ( $\lambda_D \sim \ell_2$ ). In this case spatial oscillations of wavelengths which are of the order of the Debye length are present. The charge separation is no longer small and the electrical effects interact with the flow in the two electric shock layers.



The structure of a collisional weak shock in the presence of magnetic field which is in the plane of shock was studied by Hu [Ref. 13]. He found that the shock thickness depends on four parameters, the electron mean free path  $\lambda_e$ , the electron larmor radius  $r_e$  based on thermal speed, the electron penetration length  $r_p = \frac{m_e c^2}{(4\pi n_e e^2)^{1/2}}$ , and the electron-ion mass ratio  $\varepsilon^2$ . Hu discovered two important features of the shock structure.

(1) It is possible to have collisional shocks with oscillatory structure due to electron inertia.

(2) It is possible to have collisionless shock with collisions whose thickness is smaller than the collision mean free path due to the complicated interactions between electromagnetic fields and the plasma. Often in interpreting experiments, shocks exhibiting these two features are considered as collision-free shocks.

In general, the mean free path for collisions in a plasma determines the type of the shock. A shock layer, which depends on the interaction length, can be thinner than a mean free path. These shocks provide examples for studying the mechanism of collisionless dissipation. A similar definition of the collisionless property was given by Friedman [Ref. 10]. For a given shock structure, the dissipation provided by classical collisions (ordinary momentum transfer collisions) must be less than the dissipation which is required to form a steady shock.

The first conclusive evidence of the collisionless shocks come from astrophysics. The plasma flow from sun,



the solar wind, is highly supersonic when encountering the magnetic field of the earth, and a shock wave must be formed. However, the density of this plasma is very low so that the mean free path for collisions is much longer than the dimensions of the obstacle itself, the earth's magnetosphere. Therefore a classical collisional shock wave cannot exist. Satellite observations showed the presence of a well-defined shock transition of the order of 100 Km.

In the theory of shock waves, it is important to determine the properties of the medium after passage of the shock in terms of the unperturbed quantities before the shock such as densities, pressure and temperature. Assuming that the shock profile is (quasi-)stationary in a certain reference frame, a number of relations between upstream and downstream quantities are given by jump conditions, which derive directly from the conservation of mass, momentum and energy. In usual gas dynamics and MHD-theory, these jump conditions are sufficient to determine the basic properties of the state behind the shock although a theory of the shock structure and the dissipation process leading to entropy production requires a kinetic description.

In case of a collision-free shock wave the plasma is, in general, not in local thermal equilibrium behind the shock transition. Electron and ion pressures may be quite different from each other, depending on the dissipation



mechanism. Here, the jump conditions do not completely describe the state behind the shock. A dissipation of the shock structure itself being needed. This would, e.g. provide information on the ion or electron thermalization length.

Plasma momentum transfer calculated to be collision free was observed only when a magnetic field was present by Friedman and Dawson [Ref. 11] during plasma gun studies.

Dean et. al. [Ref. 8] performed an experiment which was similar to this present one. A Nd-doped glass laser (8J, 30 nsec) was used. The target was 0.25 mm Lucite ( $C_5H_2O_2$ ) fiber suspended in an ambient nitrogen gas. They found collisionless interactions even in the absence of an applied field and explained this apparent discrepancy by the fact that spontaneously generated fields always existed in their experiment. They measured the thickness of the interaction front as approximately 1 mm and estimated the binary-collision momentum transfer mean free path, from a screened coulomb potential of the order of a centimeter.

Shock thicknesses in collisional plasmas are usually taken as one-to-several collisional mean free paths. The difficulty of establishing a given experimental situation as collision free has been emphasized by Wright [Ref. 32] who suggested that the results of [Ref. 8] can be explained by collisional coupling alone. Dean et. al. [Ref. 9],





after Wright's suggestion reperformed their experiments. They changed the target to pure carbon filaments to find out whether the multicomponent nature of the former target ( $C_5H_8O_2$ ) was playing a role. As a result they found the H and O in the target was inconsequential. They also changed background gas and used Helium instead of Nitrogen. The basic phenomena were qualitatively unchanged. They suggested that the momentum coupling region which was observed, was not a shock. It was merely a region of momentum coupling between interstreaming plasmas. The mean free path is the e-folding distance for momentum coupling, so that several mean free paths are required for a high degree of coupling.

The expanding plasma heats and transfers momentum to the photoionized background plasma. These interactions can be either collisional or collision-free depending on densities and velocities. During an experiment performed by Stamper et. al. [Ref. 27], the background densities have typically been such that electron processes are collisional while the ion processes are collision-free. They observed a sharply defined momentum coupling interaction region between the laser plasma and background plasma, but they have not observed the existence of a shock.

Koopman and Tidman [Ref. 17] observed a thin collisionless electrostatic shock front propagating radially at the leading edge of the plasma ball. In their investigation, granules of LiD have been irradiated by 15-nsec, 3-J pulses



from a Ruby laser. The target consisted of a cluster of 5-to-25  $\mu\text{m}$  diameter solid particles which were injected into the 400- $\mu\text{m}$  diameter laser focal region by an electro-mechanical apparatus. No magnetic fields were present. The phenomenon is analogous to a blast wave; the expanding plasma acts like a piston and sweeps up the background plasma. This swept-up plasma gives rise to a spherical ion-wave shock.

The distinction between collision-free and collisional mechanisms in counterstreaming plasma studies, and the appropriate techniques for calculating collisional cross sections for momentum transfer, have been the subject of considerable controversy. The question of the role of binary collisions is always a very complicated one in plasma experiments. There is still a need for more sophisticated treatments of collisional effects in plasmas.



#### IV. EXPERIMENTAL METHODS

##### A. LASER

The laser used in this investigation was a Korad-K-1500 Q-switched neodymium-doped glass laser. The laser consisted of an oscillator and a single amplifier stage. The laser was Q-switched with a Pockels cell. The laser system was operated at a power level of 230 MW, which was obtained with a pulse width (full width at half-maximum) of 22 nano-seconds. The output of the system varied within about 10 percent of 230 MW and no data were accepted if obtained at power levels outside this range. Other details of the laser are given by Davis [Ref. 6]. The laser focal spot size is approximately 0.15 cm in diameter after focusing with a 30 cm focal length lens.

##### B. LASER MONITORING TECHNIQUES

The laser beam was monitored with a Korad-K-D1 photodiode. This photodiode provides a signal which is proportional to the laser power and also by integrating, gives another signal which is proportional to the laser pulse energy.

About four percent of the beam was reflected by a beam splitter to a MgO diffusing block for viewing by the photodiode. The scattered light then passed through a 0.1 percent neutral density filter before entering the photodiode



as shown in Figure 2. The power signal was used to trigger a Tektronix 555 Dual-beam oscilloscope and was also displayed on that oscilloscope.

The energy signal was displayed on a Tektronix 564B storage oscilloscope.

The photodiode energy signal was calibrated by L.L. McKee [Ref. 18] by using a Westinghouse RN-1 laser radiometer. The radiometer provided an absolute measure of the energy incident at the target which allowed calibration of the diode's integrated signal.

The energy output of the laser was monitored on every shot. For energy outputs within 10 percent of 5.0 Joule, the pulse width was consistently  $22 \pm 1$  nsec. A two minutes cooling period between shots resulted in good reproducibility.

#### C. TEMPORAL REFERENCE FRAME

The temporal relation between the diagnostic probe response and the leading edge of the laser pulse was determined by taking into account the various cable delays and laser beam optical path lengths. A long (10 meter) delay line was used from the diagnostic probe to the oscilloscope in order to separate the laser power signal and early diagnostic responses which would otherwise be superimposed on each other.

By assuming that the signal travels at  $1.98 \times 10^{10}$  cm/sec in the RG-174/U coaxial cable, the delay was computed as 34 nsec.





#### D. PLASMA CHAMBER

The target was located in a chamber which was specially constructed by McKee to be used for the investigation of laser-plasma. The inside volume of the chamber was cylindrical with a diameter of 10 inches and a height of 6 inches (Figure 3).

The beam entered the chamber after passing through a 30 cm focal length lens and hit the target at an angle of  $30^\circ$  so that one can probe the plasma along the target normal which appears to be the axis of greatest symmetry of the expanding plasma.

The target used was an aluminum flat disc,  $1/4$  inches thick, and about 2 inches in diameter. It was rotated after approximately 10 shots to prevent severe cratering of the target in the laser impact area.

The chamber was pumped to a vacuum of about  $2 \times 10^{-6}$  Torr of air and then background gas was allowed in by a needle valve to fill the chamber up to the desired pressure. The vacuum of about  $1.3 \times 10^{-6}$  Torr was obtained by using an oil diffusion pump. Vacuum pressures lower than 0.1 m Torr were measured with an ionization gauge. A thermocouple gauge was used to measure pressures between 0.1 m Torr and 1000 m Torr, while, above 1 Torr pressures were monitored by a manometer filled with diffusion pump oil.



## E. MAGNETIC PROBES

### 1. Probe Calibration

The magnetic probe used in this investigation consisted of five turns of #40 Formvar copper wire. The probe coil was about 1 mm in diameter. The probe circuit response was linear, with an effective area ( $\eta A$ ) of the inductive loop of  $5.175 \times 10^{-6} \text{ m}^2$  for frequencies below about 8 MHz. The effective area ( $\eta A$ ) of the probe was measured by using Helmholtz coils. The instruments employed for this measurement were a General Radio 1330A continuous wave oscillator, Hewlett-Packard 411A r.f. VTVM, Helmholtz coils and a Tektronix 545B oscilloscope. A circuit diagram for probe calibration is shown in Figure 4.

The details of construction of Helmholtz coils and the use of these coils for calibration of a probe is described by McLaughlin [Ref. 19]. The effective probe area, according to McLaughlin is given by the equation

$$(\eta A) = k \frac{E}{V_L} \quad (1)$$

where  $K$  is a parameter which differs only from coil to coil (for the coil which was used in this investigation,  $K = 0.025 \text{ m}^2$ ),  $E$  is the voltage across the probe connection cable and  $V_L$  is the voltage applied to the Helmholtz coil.

### 2. Probe Signal Reliability and Sensitivity

To insure that the magnetic probe signals ( $\partial B / \partial t$ ) were meaningful, several steps were taken. The probe



signals were monitored under experimental conditions for which no target was in place, to verify that a null signal was obtained. Also, the probe was rotated by  $180^\circ$  about its axis and the probe signals were checked to make sure that they reverted in polarity. This demonstrated that the signals were not electrostatic in nature. Magnetic field signals were recorded on a Tektronix 555 dual-beam oscilloscope.

### 3. Probe Signal Integration

According to electromagnetic theory, the output of a coil is

$$e(t) = \eta A \frac{dB}{dt} \quad (26)$$

where  $\eta A$  is the effective coil area,  $B$  is the magnetic field, and  $e(t)$  is the voltage generated across the coil which was recorded on a Tektronix 555 dual-beam oscilloscope. Integration of equation (26) gives:

$$B = \int_0^B dB = \frac{1}{\eta A} \int_0^t e(t) dt \quad (27)$$

The integration of the probe signal ( $\int_0^t e(t) dt$ ) was performed by measuring the area under the  $e(t)$  curve.



## F. ELECTRIC DOUBLE PROBES

Double probe theory can be found in several references [Ref. 3] and [Ref. 4].

At sufficiently high bias voltage, the probe draws the ion saturation current  $I$

$$I \sim A_1 \overline{\eta_i Z_e} V_{Lp} \quad (28)$$

where  $A_1$  is the probe area perpendicular to the direction of plasma flow,  $\overline{\eta_i Z_e}$  is the average ionic charge per unit volume in the laser plasma and  $V_{Lp}$  is the magnitude of the plasma flow velocity.

In equation (28) the assumptions are:

- (1) The areas of probe tips are equal.
- (2) The plasma parameters are uniform across the probe tips.
- (3) Plasma-probe interactions such as secondary electron emission can be neglected.

The secondary electron emission coefficient ( $\epsilon$ ) due to ion bombardment ( $\gamma_i$ ), defined as the average number of electrons ejected per incident ion, has been measured by Koopman [Ref. 16] for similar experimental conditions and found to fall in the range of 0.0 - 0.5. Therefore secondary electron emission will contribute to the total current drawn between the probe tips. After taking secondary electron emission into account equation (28) becomes





$$I \sim (1+\epsilon) A_1 \overline{\eta_i Z e} V_{Lp} \quad (29)$$

The probe was biased at 20 volts to collect a saturated ion current. A large secondary emission coefficient of  $\epsilon = 0.5$  was used in obtaining a quantitative idea of plasma density.

The probe circuit is shown in Figure (5). The probe circuitry was enclosed by an aluminum housing attached to the probe and the entire system was isolated from ground. The diameter of the cylindrical tips was about 1 mil, they had a length of 1 mm and were about 1 mm apart.

The double probe signals were recorded on a Tektronix 555 dual-beam oscilloscope. To obtain an estimate of the plasma density, equation (t) is solved for  $\eta_i$  and evaluated with  $\bar{Z} = 1.5$ ,  $\epsilon = 0.5$ ,  $A_1 = 2.54 \times 10^{-4} \text{ cm}^2$ ,  $I = \frac{V}{R}$ ,  $R = 1 \Omega$

$$\eta_i = 1.09 \times 10^{22} \times \frac{V \text{ (volts)}}{V_{LP} \text{ (cm/sec)}} \quad (30)$$

where  $V$  is the voltage across a 1 ohm-resistor (see Figure 5).

#### G. DATA COLLECTION AND ERROR ESTIMATES

The magnetic probe was inserted into the vacuum chamber through a small pipe which was soldered onto a brass base plate.

The base plate could be moved about on an "O" ring seal located on the top of the chamber without breaking the vacuum seal. The base plate was scribed with reference lines.



These lines allowed positioning of the plate over a one millimeter grid attached to the top of the chamber. The position of the probe relative to the target was measured internally at the beginning of each data session to insure that the probe had not moved in its holder. This method allowed positioning of the probe to within  $\pm \frac{1}{2}$  mm of the stated position in relation to the target. The electric probe was inserted into the chamber from a side window.

The relative measure of plasma density from point to point is considered good due to the high reproducibility of the laser pulses. It is estimated that these relative values are accurate to within  $\pm 10$  percent.

The laser gave very reproducible pulses; the output energy was allowed to vary as much as  $\pm 10$  percent.

The area of probe tips is considered accurate to within 10 percent. The plasma expansion velocity is considered accurate to within 10 percent.



## V. EXPERIMENTAL RESULTS

During this investigation, hydrogen gas was used as the background gas. An electric probe was introduced from the port No. 6 (Figure 3) and the magnetic probe from the top window.

To decelerate the plasma front rapidly, a glass plate is placed into the vacuum chamber (Figure 7). The main influence of the glass plate on spontaneously produced magnetic field is displayed in Figure 28. This figure indicates that the maximum value of reverse field when the glass plate is in place (at  $z = 1.15$  cm), measured with the probe at  $r = 0.4$  cm,  $\theta = 0^\circ$  and  $z = 1.0$  cm, is greater than the maximum value of reverse field when the glass plate is not in place (at  $z = 7.5$  cm).

Figures 8 and 9 display the relation of  $\partial B/\partial t$  to the plasma density for a vacuum pressure of  $2 \times 10^{-6}$  Torr, as a function of time. When the glass plate is in place, the magnitude of  $\partial B/\partial t$  is greater than the magnitude of  $\partial B/\partial t$  when the glass plate is not in place.

Figure 16 demonstrates that the slope of the plasma density curve when the glass plate is at  $z = 1.15$  cm is not very different from the slope of the plasma density curve when the glass plate is at  $z = 7.5$  cm .

Figure 17 shows that when the background gas pressure is 0.5 Torr ( $H_2$ ), the existence of the glass plate at



$z = 1.15$  cm causes a noticeable steepening and a sudden increase in plasma density.

Figures 10 and 11 show the relation of  $\partial B/\partial t$  to the plasma density at a background pressure of 0.5 Torr ( $H_2$ ) as a function of time for two locations of the glass plate.

When the background gas pressure is 5.0 Torr ( $H_2$ ), the sudden increase in plasma density when the glass plate is in place (Figure 18) is much more pronounced (see also Figures 13, 15 and 28). For 5.0 Torr ( $H_2$ ) background pressure, the difference between the maximum value of reverse field when the glass plate is at  $z = 1.15$  cm and the maximum value of reverse field when the glass plate is at  $z = 7.5$  cm is greater than the difference between the same quantities for a background pressure of 0.5 Torr ( $H_2$ ).

Figures 12 and 14 display the relation of  $\partial B/\partial t$  to the plasma density for 5.0 Torr background gas pressure at the point  $r = 0.4$  cm,  $\theta = 0^\circ$  and  $z = 1.0$  cm for two different locational of the glass plate (note that each curve in this figure was multiplied by a different factor).

Figures 19, 21 and 23 demonstrate the comparison of two plasma density curves each for different background gas pressure, at the point  $r = 0.4$  cm,  $\theta = 0^\circ$  and  $z = 1.0$  cm with the glass plate at  $z = 1.15$  cm. The slope of each of these two curves is almost the same. The comparisons of the same curves when the glass plate is at  $z = 7.5$  cm are displayed in Figures 20, 22 and 24. From these figures, one





can notice that the slopes of the two density curves each one for different background gas pressures are different from each other.

Figures 25, 26 and 27 illustrate the comparison of the magnetic probe signals ( $\partial B/\partial t$ ) when the glass plate is located at  $z = 1.15$  cm with the magnetic probe signals ( $\partial B/\partial t$ ) when the glass plate is located at  $z = 7.5$  cm for  $2 \times 10^{-6}$  Torr, 0.5 Torr ( $H_2$ ) and 5.0 Torr ( $H_2$ ) background pressures. From these figures, one can see that the reverse field maximum is the greatest when the background gas pressure is 5.0 Torr ( $H_2$ ) and glass plate is at  $z = 1.15$  cm.

Figures 29, 31 and 33 illustrate the comparison of the two magnetic probe signals ( $\partial B/\partial t$ ), each one for a different background pressure, as a function of time at the point  $r = 0.4$  cm,  $\theta = 0^\circ$  and  $z = 1.0$  cm and the glass plate is in place. An investigation of these figures indicates that the higher the background gas pressure, the greater the area under the negative portion of the  $\partial B/\partial t$  curve, while the area under the positive portion of  $\partial B/\partial t$  curve becomes smaller. This means that as the background gas pressure is increased, the reverse field maximum becomes greater when the glass plate is in place. Figures 30, 32 and 34 illustrate the same comparison when the glass plate is at  $z = 7.5$  cm.

For a vacuum pressure of  $2 \times 10^{-6}$  Torr, the magnitude of the magnetic probe signal ( $\partial B/\partial t$ ) when the glass plate is in place is about 4 times greater than the magnitude of



the magnetic probe signal ( $\partial B/\partial t$ ) when the glass plate is not in place (see Figure 25). (Note that each curve in this figure was multiplied by a different factor.)

When the glass plate is in place, the magnitude of the magnetic probe signal ( $\partial B/\partial t$ ) at a vacuum pressure of  $2 \times 10^{-6}$  Torr is greater than the magnitude of the magnetic probe signals ( $\partial B/\partial t$ ) at 0.5 Torr ( $H_2$ ) background pressure and at 5.0 Torr ( $H_2$ ) background pressure (see Figures 29 and 31). But when the glass plate is not in place, the magnitude of the magnetic probe signal ( $\partial B/\partial t$ ) at  $2 \times 10^{-6}$  Torr vacuum pressure is smaller than the magnitude of the magnetic probe signals ( $\partial B/\partial t$ ) at 0.5 Torr ( $H_2$ ) background pressure and at 5.0 Torr ( $H_2$ ) background pressure (see Figures 30 and 32). From Figure 34, it can be seen that when the glass plate is not in place, the magnitude of the magnetic probe signal ( $\partial B/\partial t$ ) at 0.5 Torr ( $H_2$ ) background pressure is greater than the magnitude of the magnetic probe signal ( $\partial B/\partial t$ ) at 5.0 Torr ( $H_2$ ) background pressure. (Note that each curve in this figure was multiplied by a different factor.) But Figure 33 illustrates that when the glass plate is in place the magnitude of the magnetic probe signal ( $\partial B/\partial t$ ) at a background pressure of 0.5 Torr ( $H_2$ ), between 0 and 100 nsec is greater but between 100 and 450 nsec it is smaller than the magnitude of the magnetic probe signal ( $\partial B/\partial t$ ) at a background pressure of 5.0 Torr ( $H_2$ ). (Note that each curve in this figure was multiplied by a different factor.)



Figure 35 illustrates that when the glass plate is in place, for a background pressure of 5.0 Torr ( $H_2$ ), the slope of the plasma density curve at the point  $r = 0.4$  cm,  $\theta = 0^\circ$  and  $z = 1.0$  cm is greater than the slope of the plasma density curve at the point  $r = 0.8$  cm,  $\theta = 0^\circ$  and  $z = 1.0$  cm. But when the glass plate is not in place (Figure 36) the slopes of two plasma density curves are the same.

During this investigation, for a background pressure of 5.0 Torr ( $H_2$ ), the maximum value of the magnitude of the reverse magnetic field was measured as 150 gauss when the glass plate is in place at the point  $r = 0.4$  cm,  $\theta = 0^\circ$  and  $z = 1.0$  cm and at  $t = 440$  nsec, while at same background pressure, point and time but when the glass plate is not in place, the maximum value of the magnitude of the reverse magnetic field was measured as 45 gauss only.



## VI. COMPARISON OF THEORY AND EXPERIMENTAL RESULTS

As mentioned in Section III-C, the production of initial field requires a density gradient in the  $-z$  direction and a temperature gradient in the  $-r$  direction (see Figure 6). The cross product of these two vectors generates a magnetic field in the  $\theta$  direction i.e., in the clockwise direction when looking in the direction of the laser beam.

If one of the gradients is reversed to the opposite direction, a magnetic field, in the counterclockwise direction is produced. The radial temperature gradient is always in the  $-r$  direction and its direction remains unchanged, either the glass plate is in place or not. Therefore the only possible gradient which can be reversed by placing the glass plate at  $z = 1.15$  cm, is the axial density gradient. The equation of continuity is

$$\frac{\partial \eta}{\partial t} + \nabla \cdot (\eta V) = 0 \quad (31)$$

if cylindrical symmetry is assumed;

$$\frac{\partial \eta}{\partial t} + \frac{\partial \eta}{\partial z} \cdot \frac{dz}{dt} + \frac{\partial \eta}{\partial r} \cdot \frac{dr}{dt} = 0 \quad (32)$$

Also for the laser-produced plasma expanding in the  $z$ -direction

$$\frac{dz}{dt} \gg \frac{dr}{dt}$$





thus:  $\frac{\partial \eta}{\partial t} \approx - \frac{\partial \eta}{\partial t} \cdot \bar{V}$  where  $\bar{V}$  is the expansion velocity of the plasma front.

Figure 13 demonstrates the relation of  $B_\theta$  to the plasma density as a function of time at the point  $r = 0.4$  cm,  $\theta = 0^\circ$  and  $z = 1.0$  cm for a background gas pressure of 5.0 Torr ( $H_2$ ) when the glass plate is at  $z = 1.15$  cm. Between  $t \approx 100$  nsec and  $t \approx 180$  nsec.  $\frac{\partial \eta}{\partial t}$  is positive, which means that  $\frac{\partial \eta}{\partial z}$  is negative or the axial density gradient is in the  $-z$  direction. Figure 28 illustrates that at  $t \approx 150$  nsec the reverse field appears when the glass plate is in place. Since the axial density gradient at this time is in the  $-z$  direction, the production of the reverse field can not be correlated to any change of sign in the direction of the axial density gradient, since there is no such change when the reverse field is "turned on."

There always exists a radial density gradient in the  $-r$  direction, no matter where the glass plate is (see Figures 35 and 36). Therefore it requires an axial temperature gradient in the  $-z$  direction. Such an axial temperature gradient can be generated by the shock heating of the plasma.

Figure 28 demonstrates that the magnitude of the initial magnetic field, when the glass plate is in place is smaller than the magnitude of the initial magnetic field when the glass plate is not in place. This decrease



in magnitude of the initial magnetic field is caused by the decrease in axial density gradient due to pile-up of laser plasma in front of the glass plate. This piled up plasma then diffuses radially and also causes a decrease in radial density gradient. This decrease in radial density gradient can be seen if one compares Figure 35 and Figure 36.

Figure 18 displays the steepening in the plasma density between 150 and 200 nsec, when the expanding plasma impinges on a glass plate. This steepening can be related to the formation of a shock wave. Such a shock wave causes an increase in plasma temperature (see Appendix A) and this increase results in an axial temperature gradient in the  $-z$  direction, since the shock wave travels in the  $+z$  direction.

As long as the ratio,

$$\frac{\left| \frac{\partial B_z}{\partial t} \right|}{\left| \frac{\partial B_r}{\partial t} \right|} = \frac{|\nabla_r T_e| |\nabla_z n|}{|\nabla_z T_e| |\nabla_r n|}$$

is greater than one, the reverse field only reduces the magnitude of the initial magnetic field. But when this ratio decreases to a value which is less than one, the reverse field becomes the dominant field.

From Figure 18, the ratio of two densities, one at  $t = 159.37$  nsec the other at  $t = 180.83$  nsec, is:

$$\frac{\eta_e}{\eta_i} = 1.5 \quad \text{and} \quad \Delta t = 21.46 \text{ nsec}$$



in order to obtain this density ratio, the shock wave must have a Mach number of the order of 1.37. According to the classification of Jaffrin and Probst [Ref. 15] this shock is a "moderate" shock whose thickness is of the order of  $\ell/\epsilon$ , where  $\ell$  is the downstream (before shock) ion-ion collision mean free path, and  $\epsilon = (\frac{m_e}{m_i})^{1/2}$ . The electron temperature increases in this layer but the ion temperature increases in the second inner layer (see Section III-E) whose approximate thickness is the downstream ion-ion collision mean free path  $\ell$ .

For this Mach number  $M = 1.37$ , a temperature ratio,

$$\frac{T_{e2} + T_{i2}}{T_{e1} + T_{i1}} = 1.368$$

is obtained from the Rankine-Hugoniot jump conditions (see Appendix A, equation 3).

Since the shock thickness can be defined from the electric probe data as  $\delta = V\tau$ , where  $V$  is the velocity of the expanding front and  $\tau$  is the rise time of the probe signal.

If no interactions were occurring between the inter-streaming plasmas, then the plasma expansion velocity would be independent of background gas pressure. The observed dependence of expansion velocity can be seen in Figures 20, 22, 24, between 100 and 200 nsec. From these figures one can conclude that as background gas pressure increases, the expansion velocity decreases.



To have an idea about the structure of the shock one must compare the shock thickness with the collision mean free path length. The ion-ion collision mean free path can be calculated from

$$\lambda \text{ (cm)} \approx \frac{10^{13}}{\eta_i \text{ (cm}^{-3}\text{)} \times \ln \Lambda} \times T_i^2 \text{ (eV)},$$

where  $T_i$  is the ion temperature. In order to calculate  $\lambda$ , one needs to know  $\eta_i$  and  $T_i$ .

From  $kT_i = \frac{1}{2}m_i V^2$ , where  $V$  is the expansion velocity and  $m_i$  is the ion mass,  $T_i$  can be estimated. If one assumes that the Shock wave propagates in the background gas, or background gas flows into the shock relative to the frame of the shock, for hydrogen background gas,  $m_i = m = 1.673 \times 10^{-24}$  g and  $V \approx 10^7$  cm/sec. For these values of  $m_i$  and  $V$ ,  $T_i \approx 52$  eV is obtained. Assuming a fully dissociated and fully ionized background gas at 5.0 Torr the downstream ion density is

$$\eta_i \leq 2 \times 3.3 \times 5 \times 10^{16} \text{ cm}^{-3} \leq 3.3 \times 10^{17} \text{ cm}^{-3}.$$

For these values of  $\eta_i$  and  $T_i$ ,  $\lambda$  is of the order of  $8.2 \times 10^{-3}$  cm.

The shock thickness can be obtained from Figure 18, in which  $\tau = \Delta t = 21.46 \times 10^{-9}$  sec and for  $V \approx 10^7$  cm/sec  $\delta = \tau V = 21.46 \times 10^{-2} = 0.21$  cm. Since the shock thickness  $\delta$





is greater than the ion-ion collision mean free path, the formation of a collisional shock wave must be expected.

In summary it can be said that whenever the background gas pressure is high enough, the expanding laser plasma acts like a piston and sweeps up the photoionized background plasma. In front of this piston a shock is formed to drive an axial temperature gradient which is large enough to produce a reverse magnetic field.



## VII. SUMMARY AND CONCLUSIONS

The observed dependence of the plasma front expansion velocity on background gas pressure indicates the existence of an interaction between the laser plasma and the photoionized background plasma. As a result of this interaction, a collisional shock wave, driven by the laser plasma piston is formed. This shock wave heats and compresses the plasma.

Initially the spontaneously produced magnetic field is in the  $\theta$ -direction (see Figure 1) and the thermal source term for these magnetic fields consists of the cross product of the radial density gradient and the axial density gradient. When the shock wave is formed an axial temperature gradient is produced. This axial temperature gradient and the radial density gradient which always exists in the plume shaped laser plasma are the main cause of the reversal of these initial magnetic fields.

The comparison of the shock thickness and the collision mean free path determines the type of the shock. If the shock thickness is greater than the collision mean free path, the shock is collisional in nature.

Determining the mean free path length in a plasma is always a complicated undertaking and the results should be considered as crude estimates. More sophisticated treatments are necessary in order to determine the collisional effects in plasmas.



The reversal of the spontaneous magnetic field indicates the existence of a shock wave propagating through the plasma. Such generation of magnetic fields by shock waves can be a very important mechanism in astrophysics.



#### VIII. RECOMMENDATION FOR FURTHER STUDY

The electron temperature has been evaluated indirectly from the shock parameters. An experimental measurement of the electron temperature gradient is required for a further study of field reversal in shock waves. Plasma temperature, before and after the plasma front encounters the glass plate can be measured by means of x-ray diagnostic techniques or by other means. Also, more accurate data about the  $r$  dependence of the plasma density are needed to provide a quantitative comparison between experiment and theory. The data about the  $r$  dependence of the plasma density can be obtained by use of the electric probe technique.





## APPENDIX A

Rankine-Hugoniot jump conditions can be determined by using the equation of continuity, conservation of momentum density and conservation of energy density in the plasma for steady state conditions [Ref. 29].

The Mach number is defined for  $\frac{c_p}{c_v} = \gamma = \frac{5}{3}$  as:

$$M = \frac{V_1}{\sqrt{\frac{5k(T_{e1} + T_{i1})}{3M}}} \quad (1)$$

where  $V_1$  is the downstream (before shock) fluid velocity,  $T_{e1}$  is the downstream electron temperature,  $T_{i1}$  is the downstream ion temperature and  $M$  is the ion mass.

The jump conditions are:

$$\frac{n_1}{n_2} = \frac{V_2}{V_1} = \frac{1}{4} \left[ \frac{3}{M^2} + 1 \right] \quad (2)$$

$$\frac{T_{i2} + T_{e2}}{T_{i1} + T_{e1}} = \frac{(M^2 + 3)(5M^2 - 1)}{16M^2} \quad (3)$$

where the subscript "2" implies upstream (after shock) value.



FIGURES

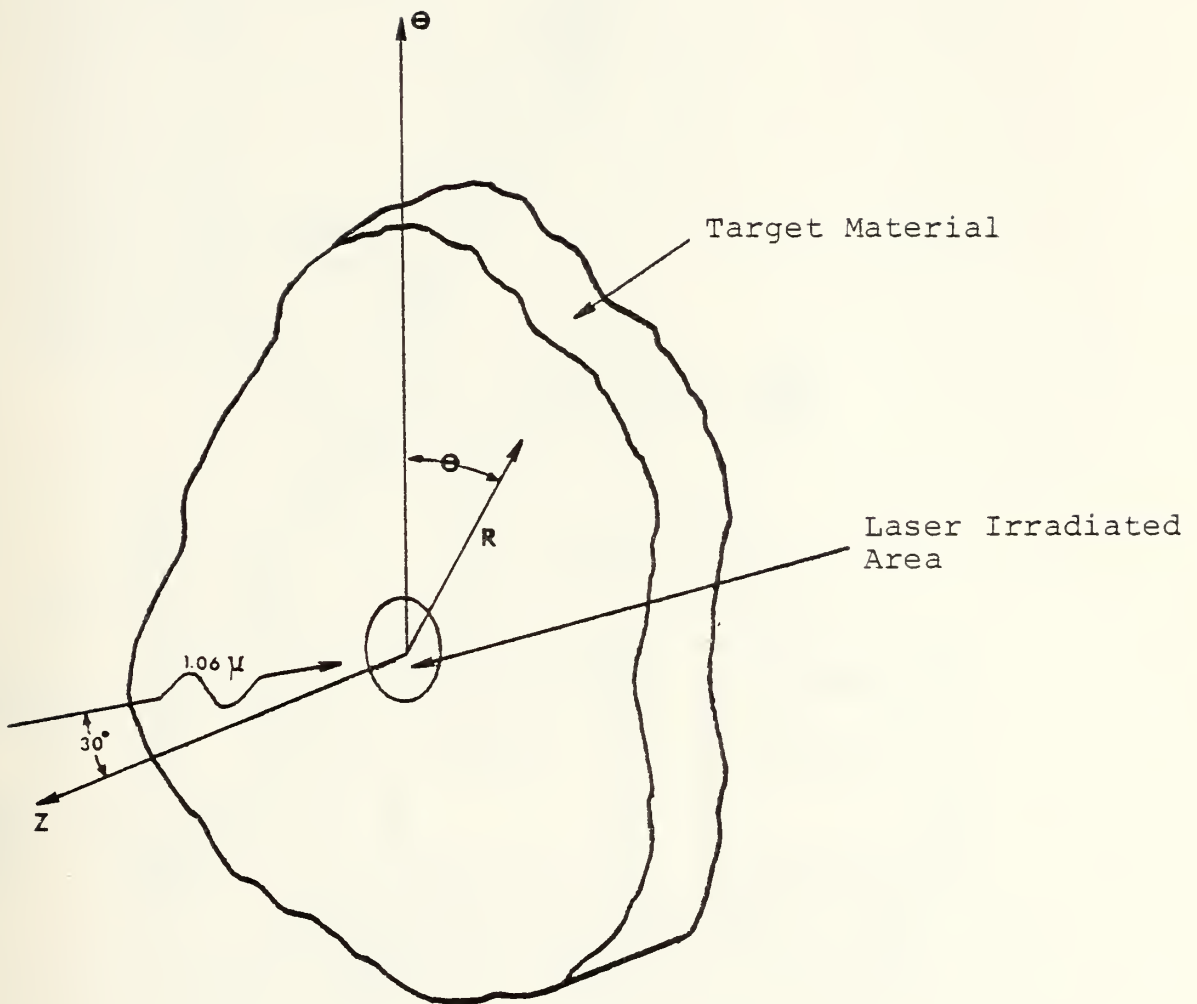


Figure 1. Cylindrical polar coordinate system



- A - Nd Amplifier Laser
- B - Beam Expansion Optics
- C - Nd Oscillator Laser
- D - Polarizer
- E - Pockels Cell
- F - CW Alignment Laser
- G - Photodiode
- H - MgO Diffuser
- I - Beam Splitter
- J - Lens
- K - Tektronix 564B  
Storage Oscilloscope
- L - Tektronix 555  
Dual Beam Oscilloscope
- M - Power Supply
- N - Electric Probe
- O - Magnetic Probe
- P - Target
- Q - Rotation Knob
- R - Glass Plate
- S - Rotation Knob
- T - Magnetic Probe Signal
- U - Electric Probe Signal
- V - Energy Signal
- W - Laser Power  
(Trigger) Signal

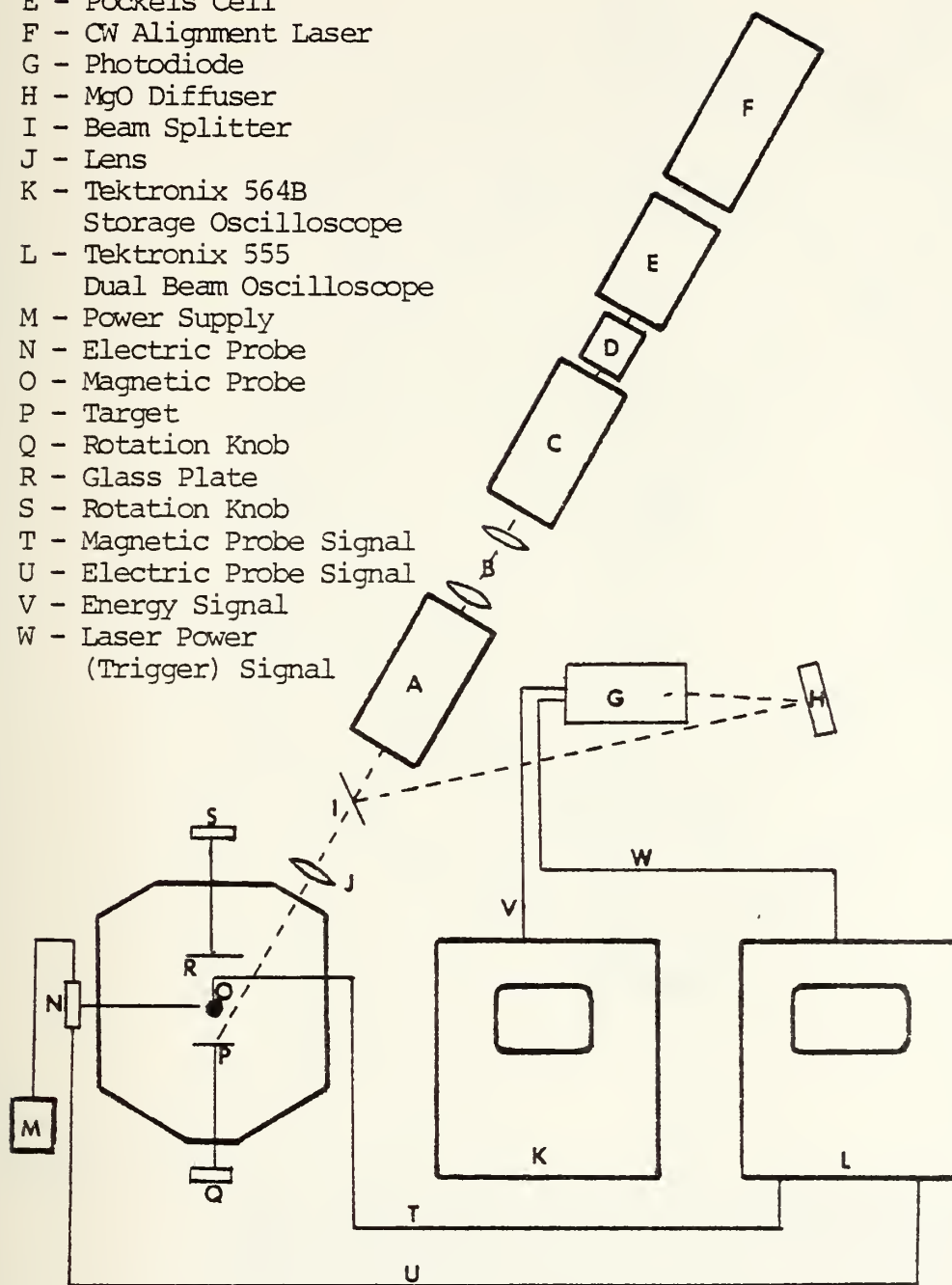


Figure 2. Block diagram of experimental layout



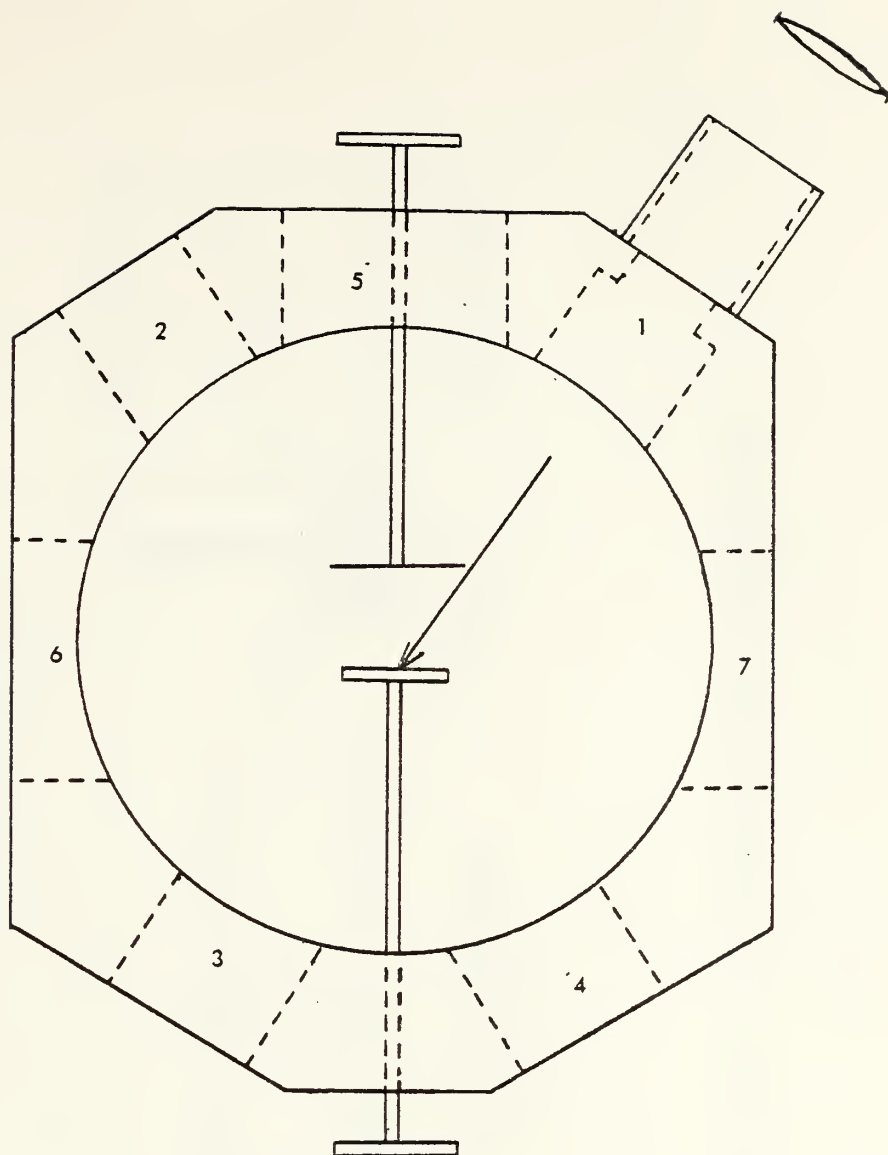


Figure 3. Top view of vacuum chamber. Port #1 is the laser beam entry port, #2 is the reflected laser beam observation port, #3 is the transmitted laser beam observation port, #4 is the optical observation port, #5 is the glass plate entry port, #6 is the electric probe entry port, #7 is the probe observation port.





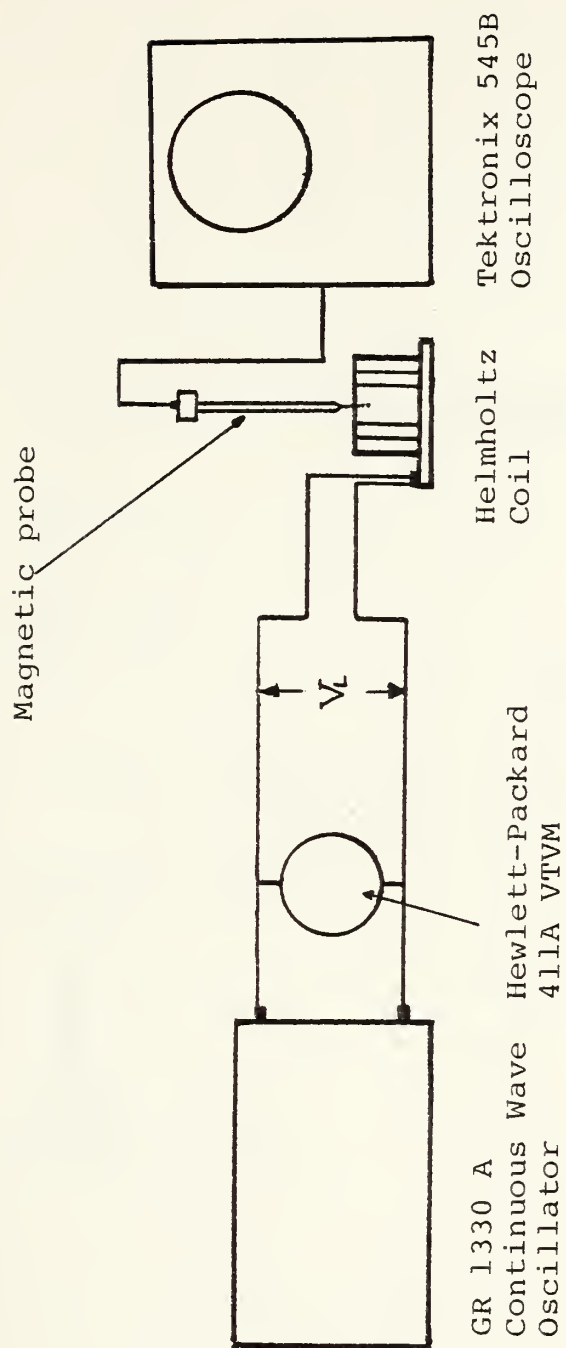


Figure 4. Circuit layout for magnetic probe calibration



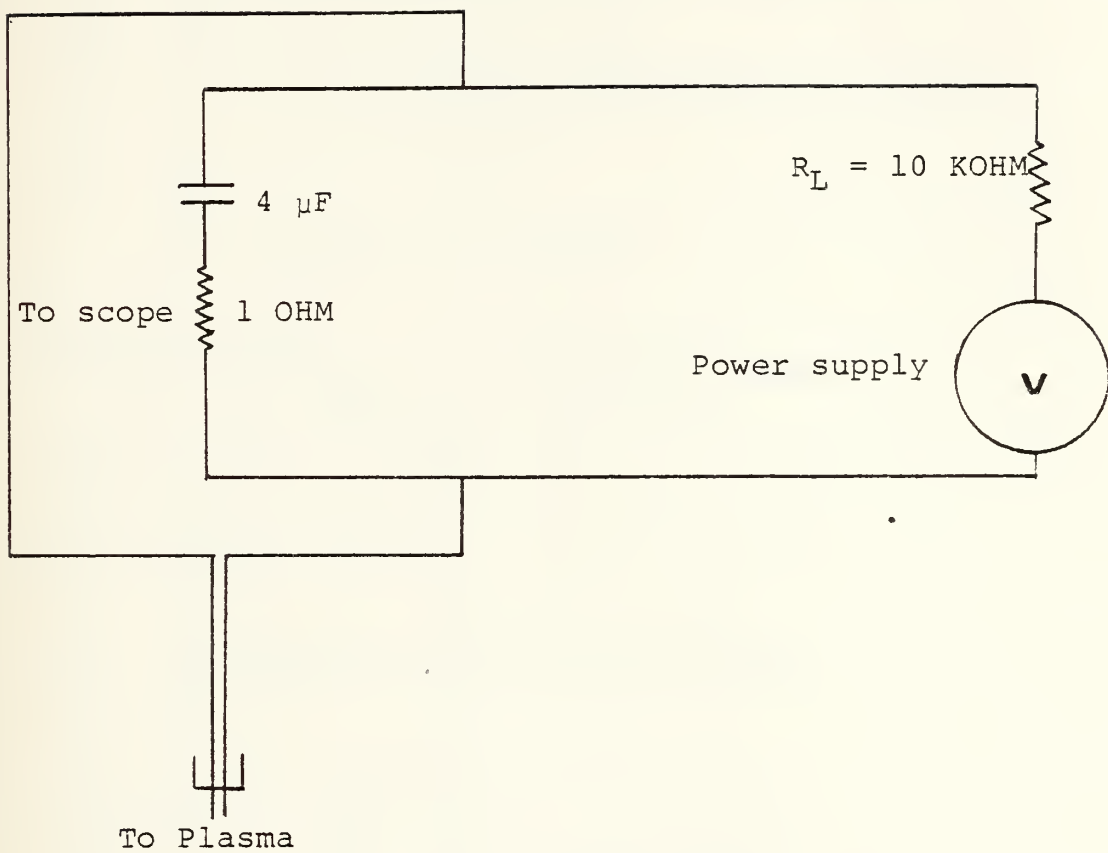
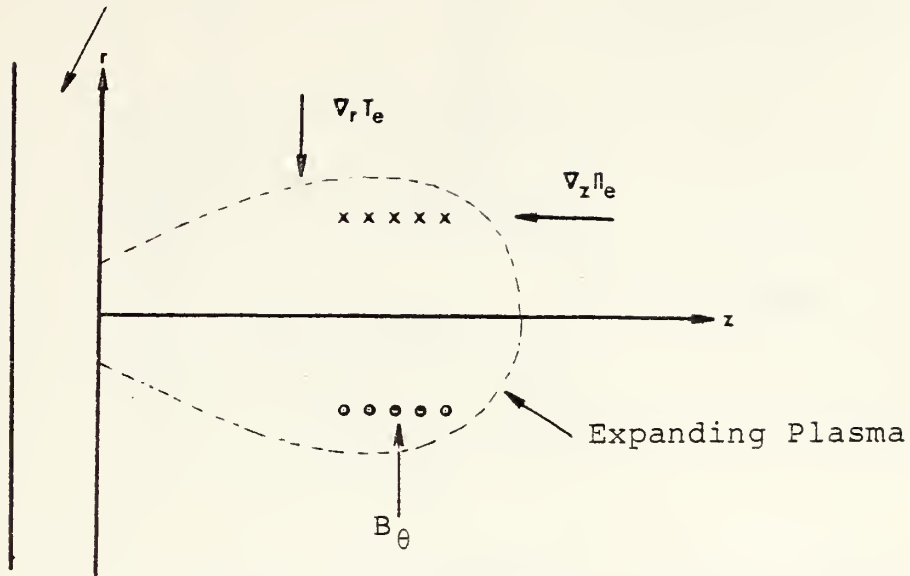


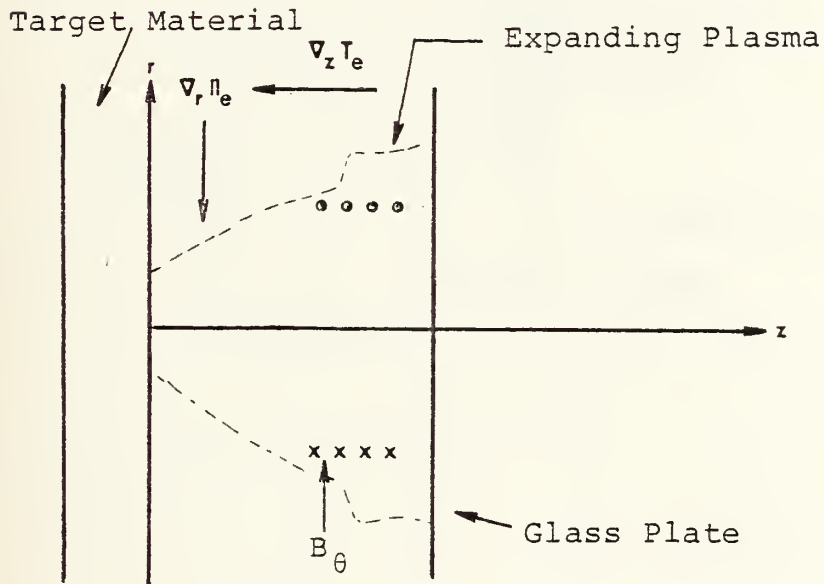
Figure 5. Electric double probe circuit



Target Material



(a) Without glass plate



(b) With glass plate

Figure 6. Geometry of a laser produced plasma and the self generated magnetic field



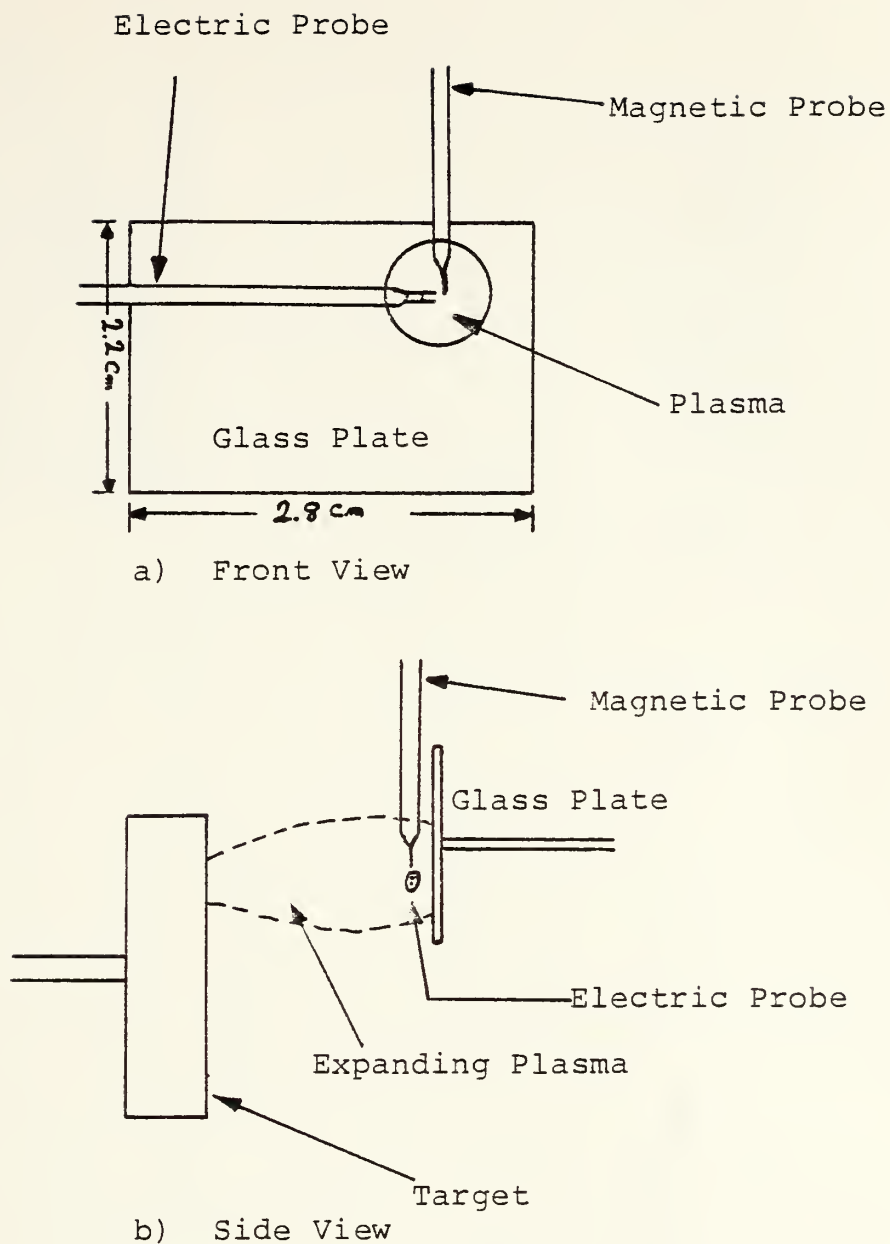


FIGURE 7. Arrangement of the target, glass plate and probes





Figure 8.

Relation of  $\partial B / \partial t$  to the plasma density as a function of time at the point  $r = 0.4$  cm,  $\theta = 0^\circ$  and  $z = 1.0$  cm for a vacuum pressure of  $2 \times 10^{-6}$  Torr. Plate at  $z = 1.15$  cm.

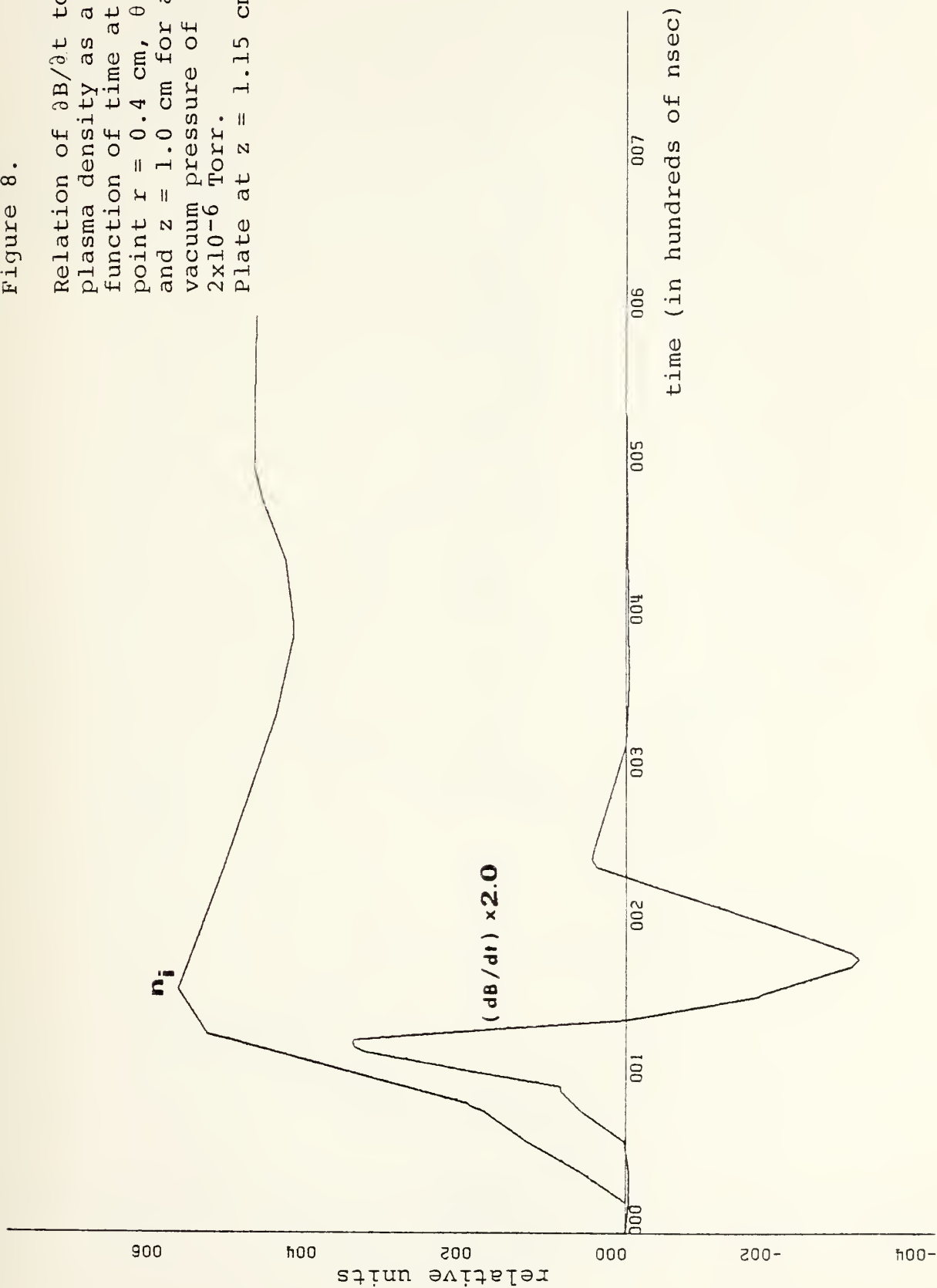




Figure 9

Relation of  $\partial B / \partial t$   
to the plasma density  
as a function of time  
at the point  $r = 0.4$  cm,  
 $\theta = 0^\circ$  and  $z = 1.0$  cm  
for a vacuum pressure  
of  $2 \times 10^{-6}$  Torr.  
Plate at  $z = 7.5$  cm.

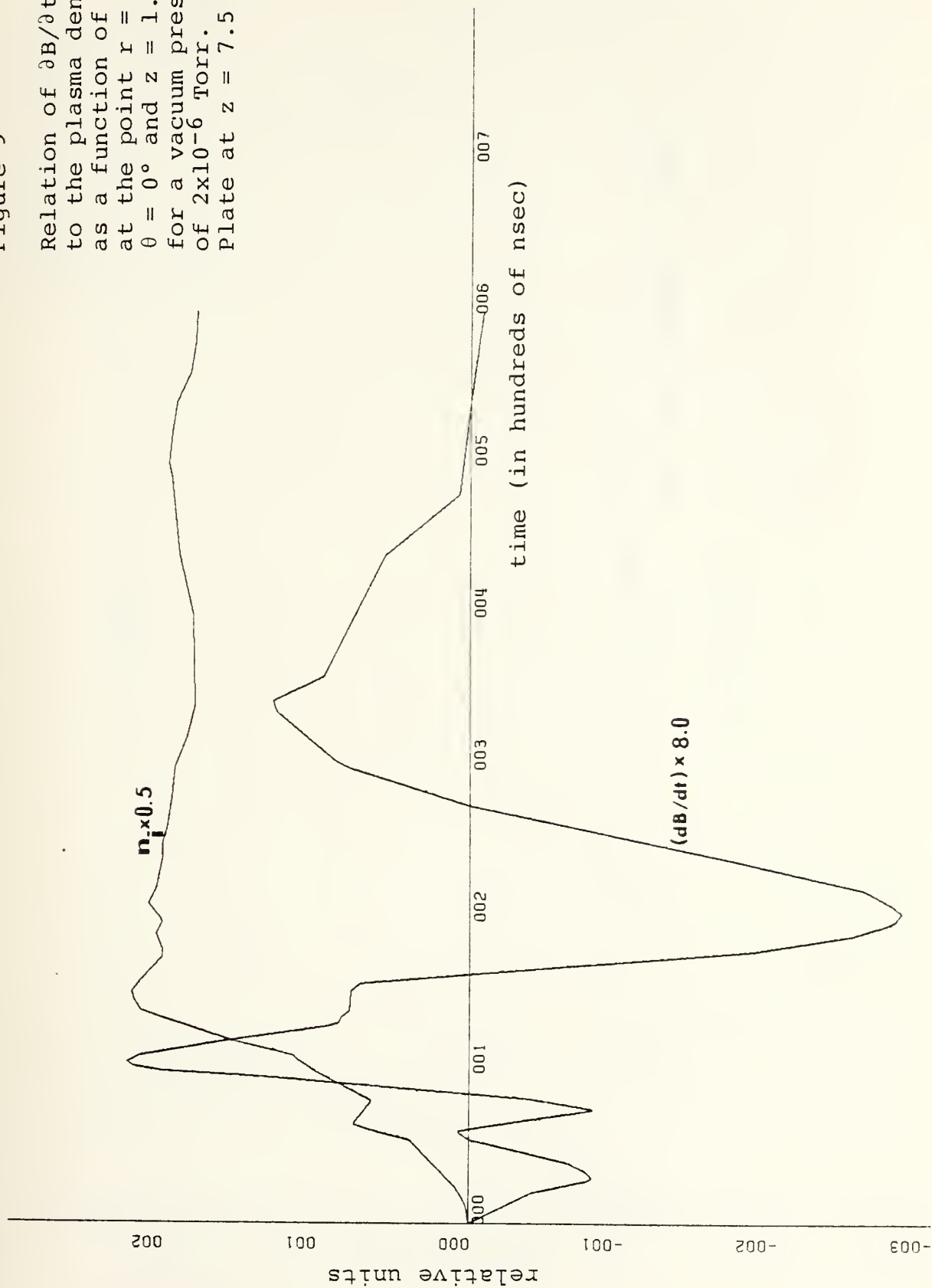




Figure 10

Relation of  $\partial B / \partial t$  to the plasma density as a function of time at the point  $r = 0.4$  cm,  $\theta = 0^\circ$  and  $z = 1.0$  cm for the background pressure of 0.5 Torr  $H_2$ . Plate at  $z = 1.15$  cm.

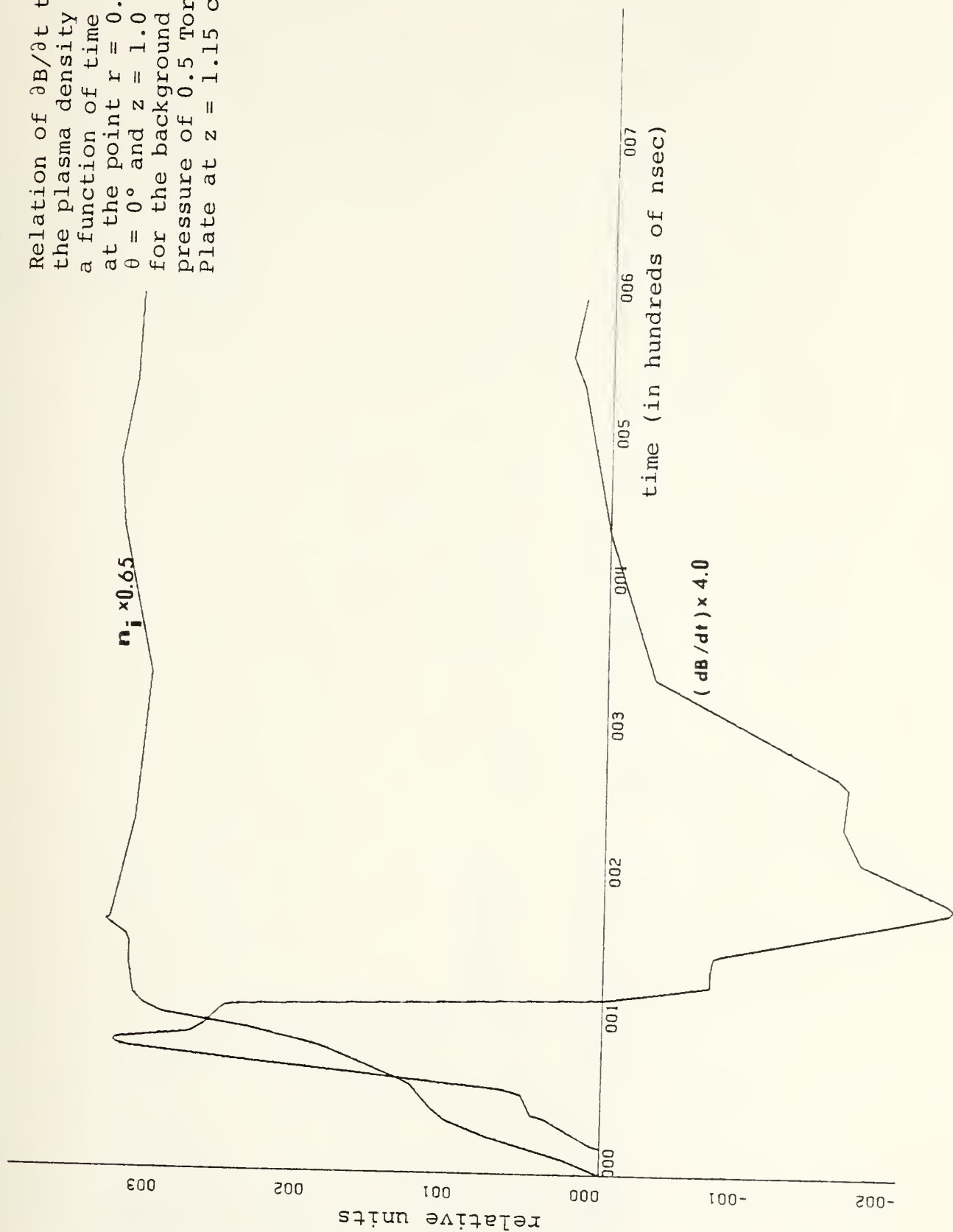




Figure 11

Relation of  $\partial B / \partial t$  to the plasma density as a function of time at the point  $r = 0.4$  cm,  $\theta = 0^\circ$  and  $z = 1.0$  cm for a background pressure of 0.5 Torr  $H_2$ . Plate at  $z = 7.5$  cm.

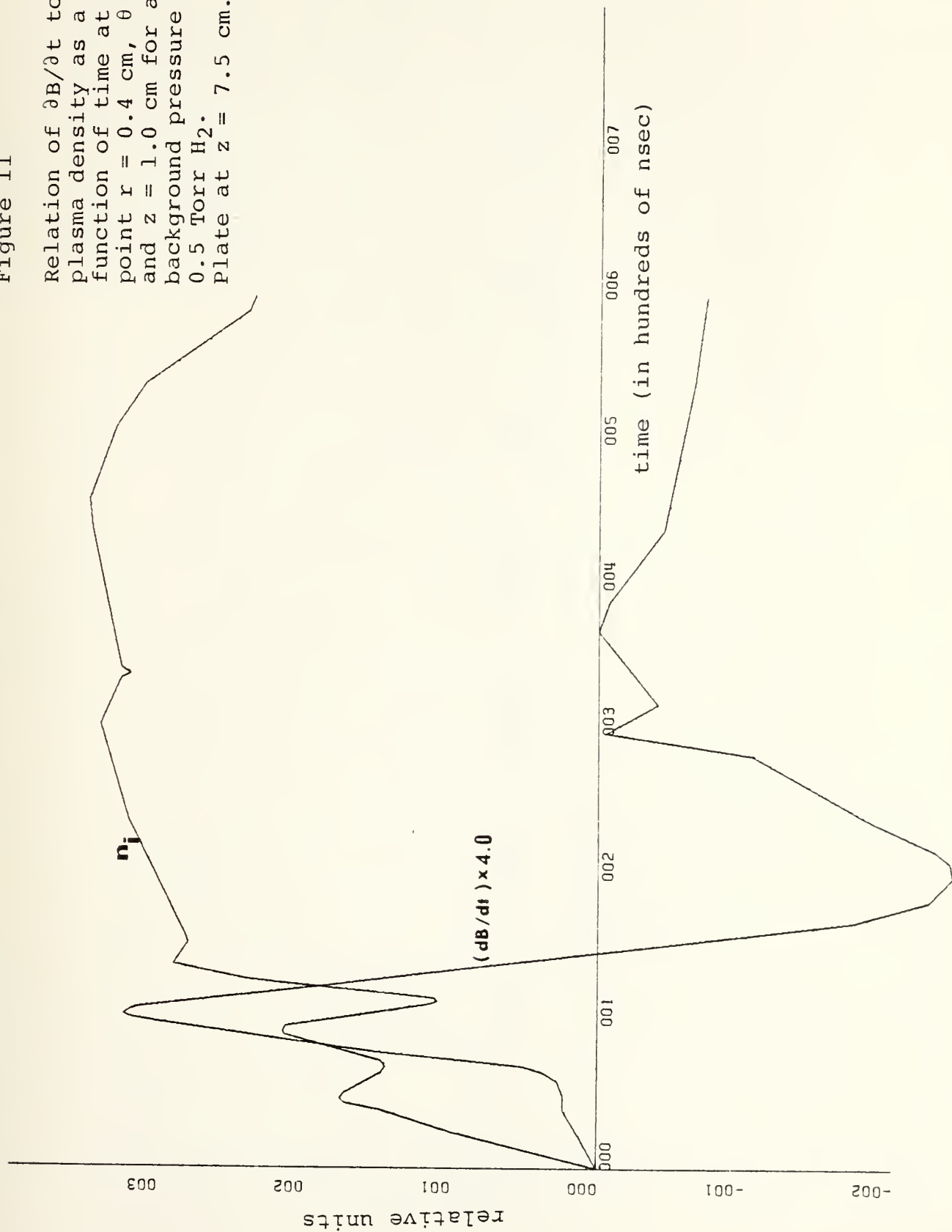






Figure 12

Relation of  $\partial B / \partial t$  to the plasma density as a function of time at the point  $r = 0.4$  cm,  $\theta = 0^\circ$  and  $z = 1.0$  cm for a background pressure of 5.0 Torr  $H_2$ . Plate at  $z = 1.15$  cm.

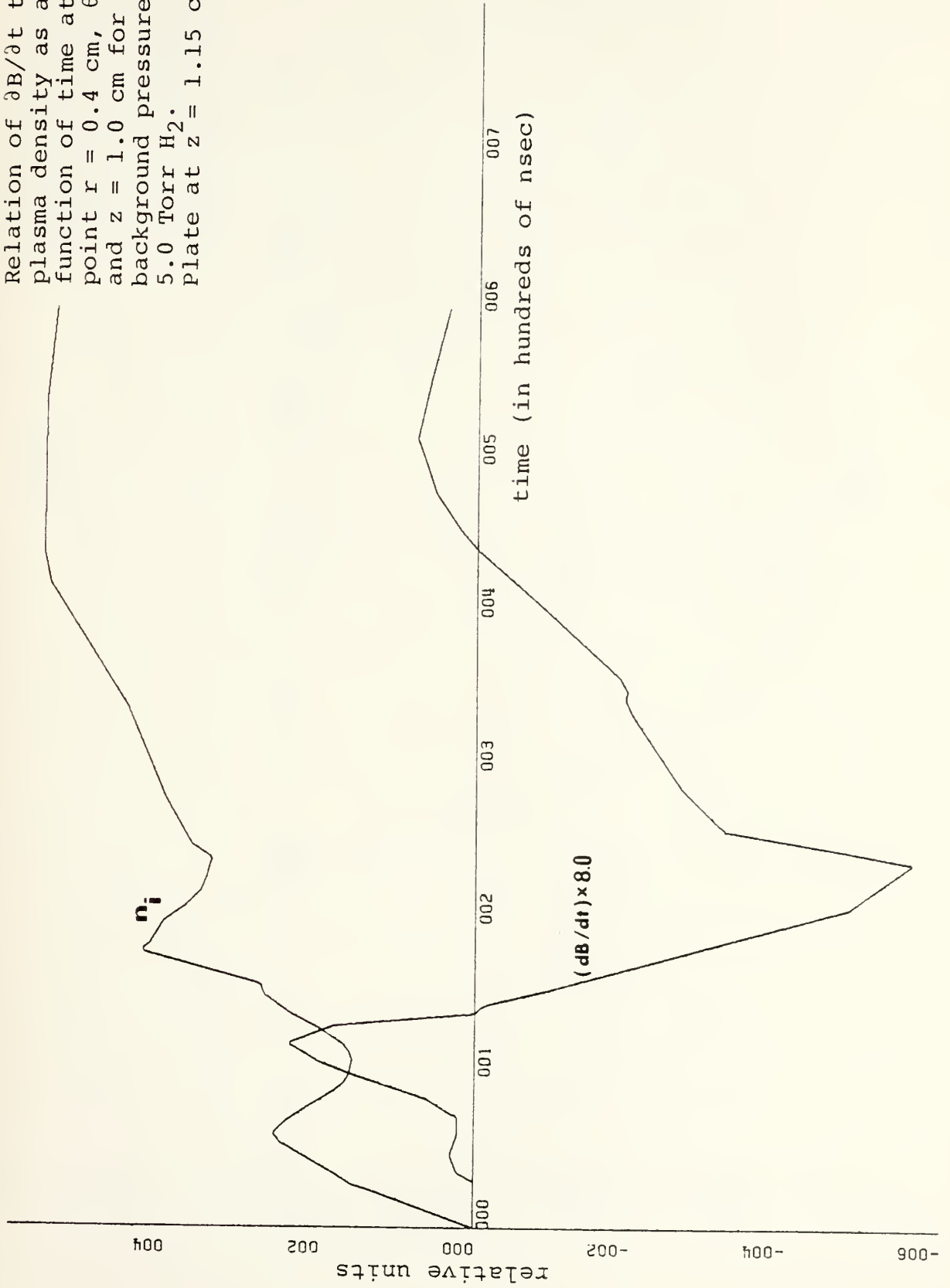




Figure 13

Relation of  $B_\theta$  to the plasma density as a function of time at the point  $r = 0.4$  cm,  $\theta = 0^\circ$  and  $z = 1.0$  cm for a background pressure of 5.0 Torr  $H_2$ .  
Plate at  $z = 1.15$  cm.

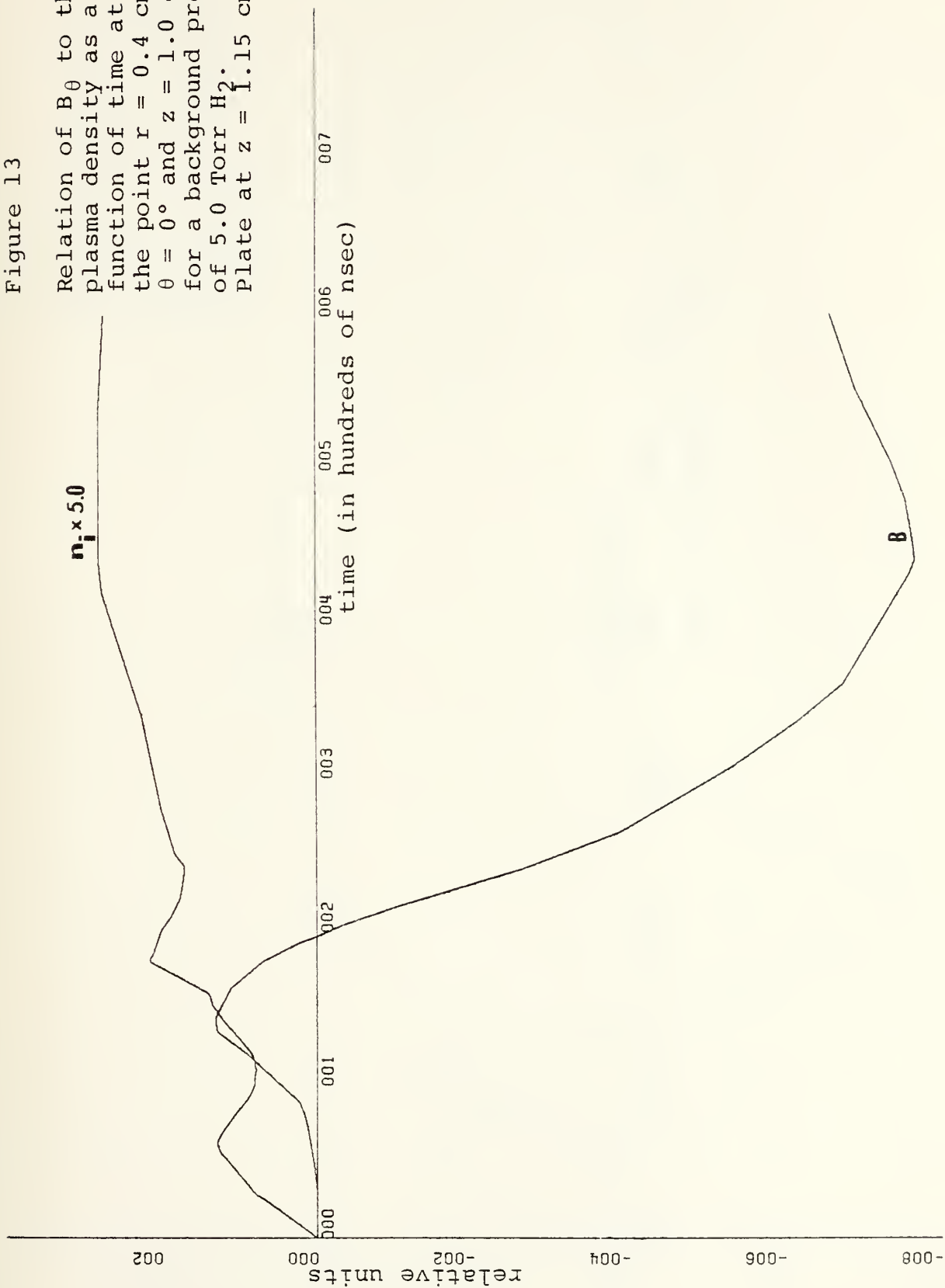




Figure 14

Relation of  $\partial B / \partial t$  to the plasma density as a function of time at the point  $r = 0.4$ ,  $\theta = 0^\circ$  and  $z = 1.0$  cm for the background pressure of 5.0 Torr  $H_2$ . Plate at  $z = 7.5$  cm.

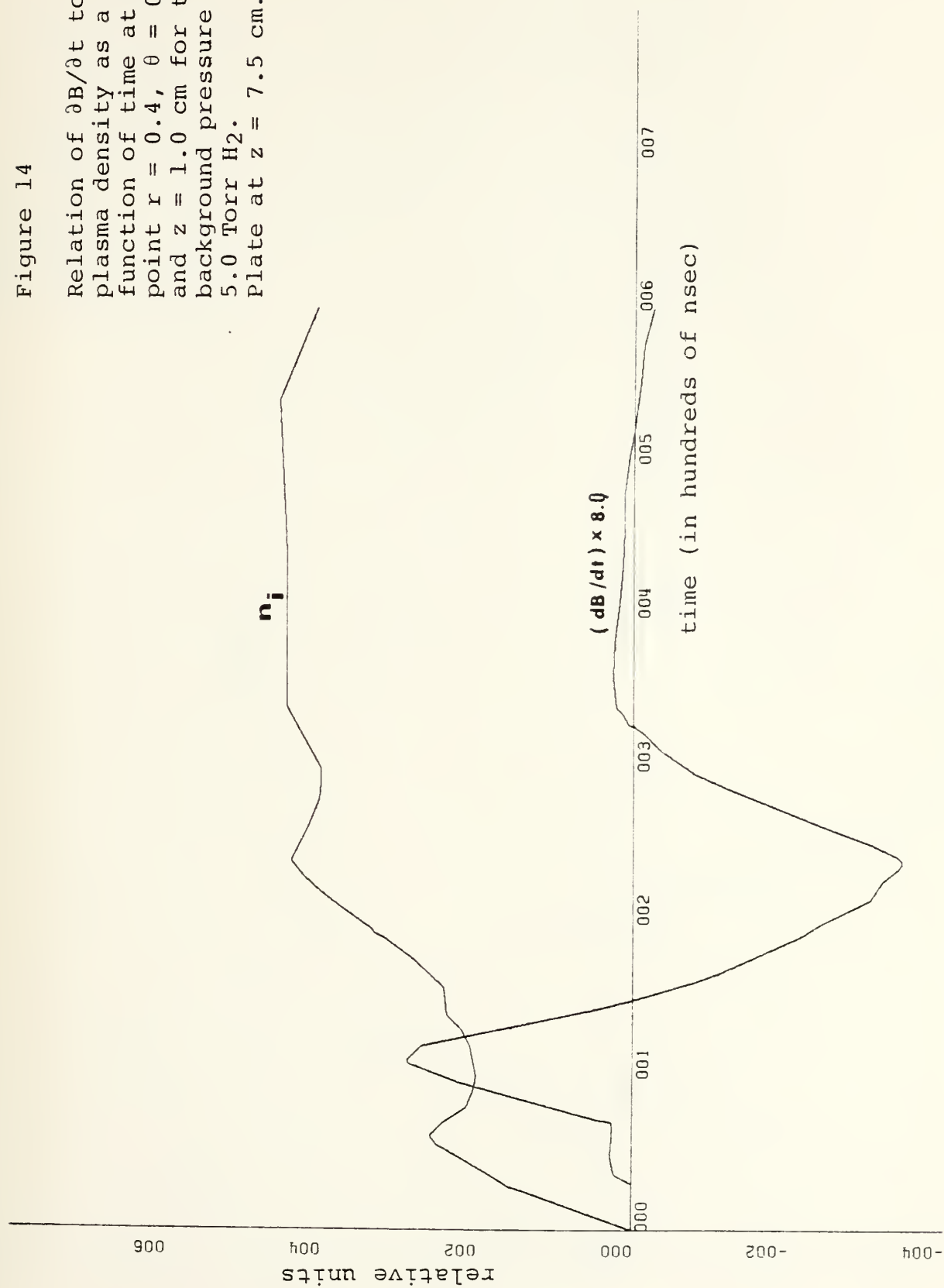




Figure 15

Relation of  $B_\theta$  to the  
plasma density as a  
function of time at the  
point  $r = 0.4$  cm,  $\theta = 0^\circ$   
and  $z = 1.0$  cm for the  
background pressure of  
5.0 Torr  $H_2$ .  
Plate at  $z = 7.5$  cm.

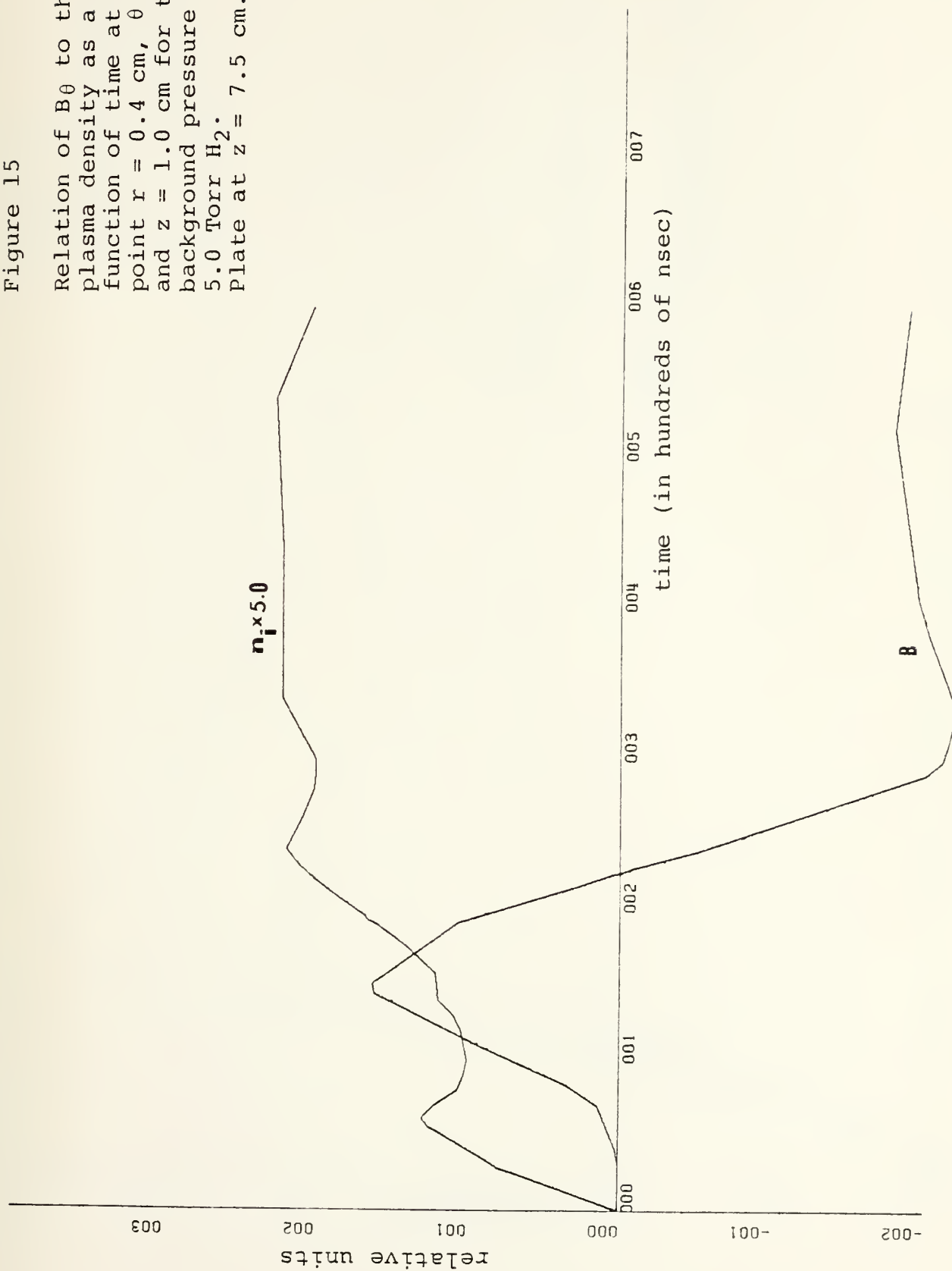
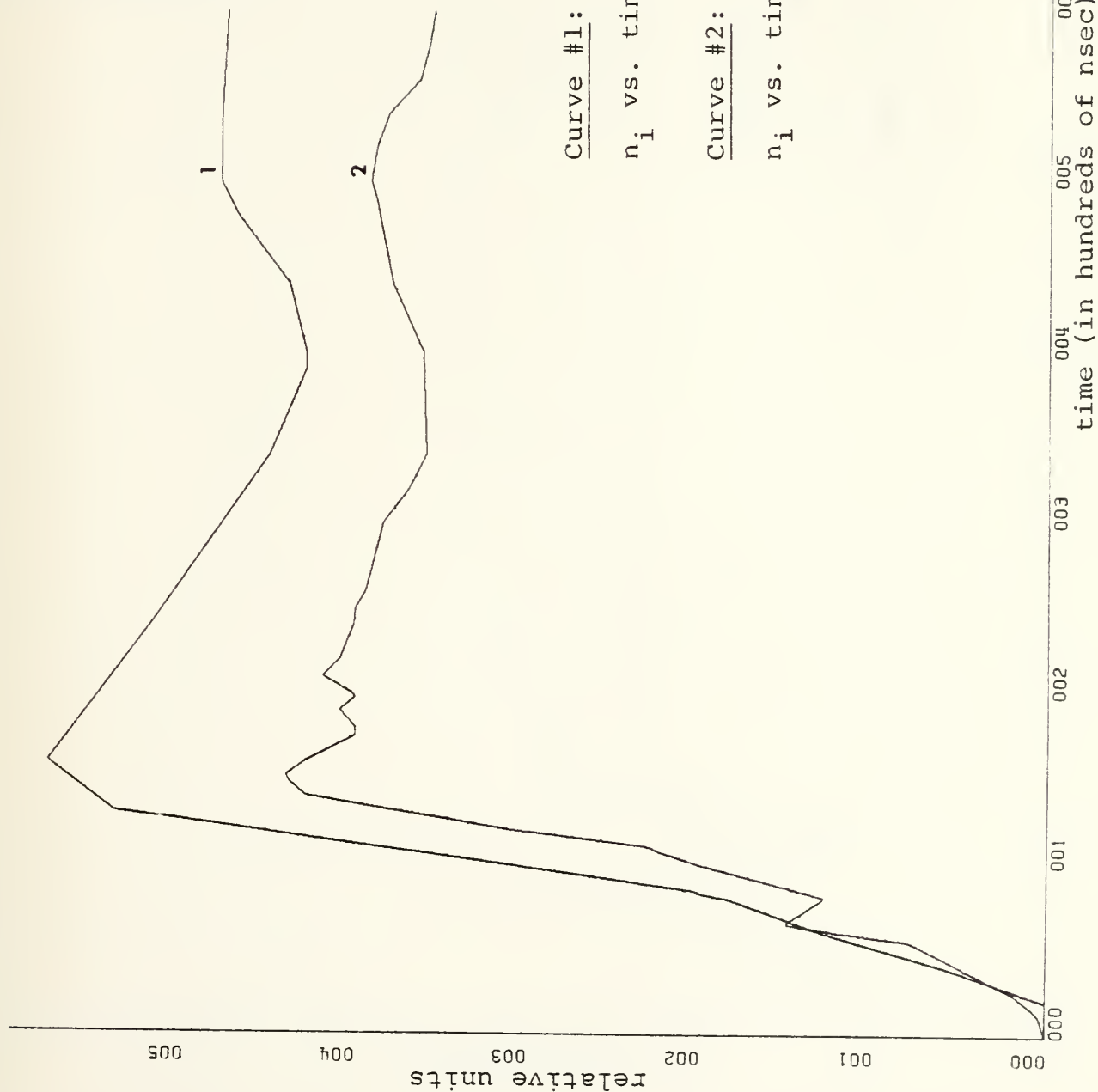






Figure 16

Plasma density as a function of time at the point  $r = 4.0$  cm,  $\theta = 0^\circ$  and  $z = 1.0$  cm for a vacuum pressure of  $2 \times 10^{-6}$  Torr



Curve #1:

$n_i$  vs. time, plate at  $z = 1.15$  cm

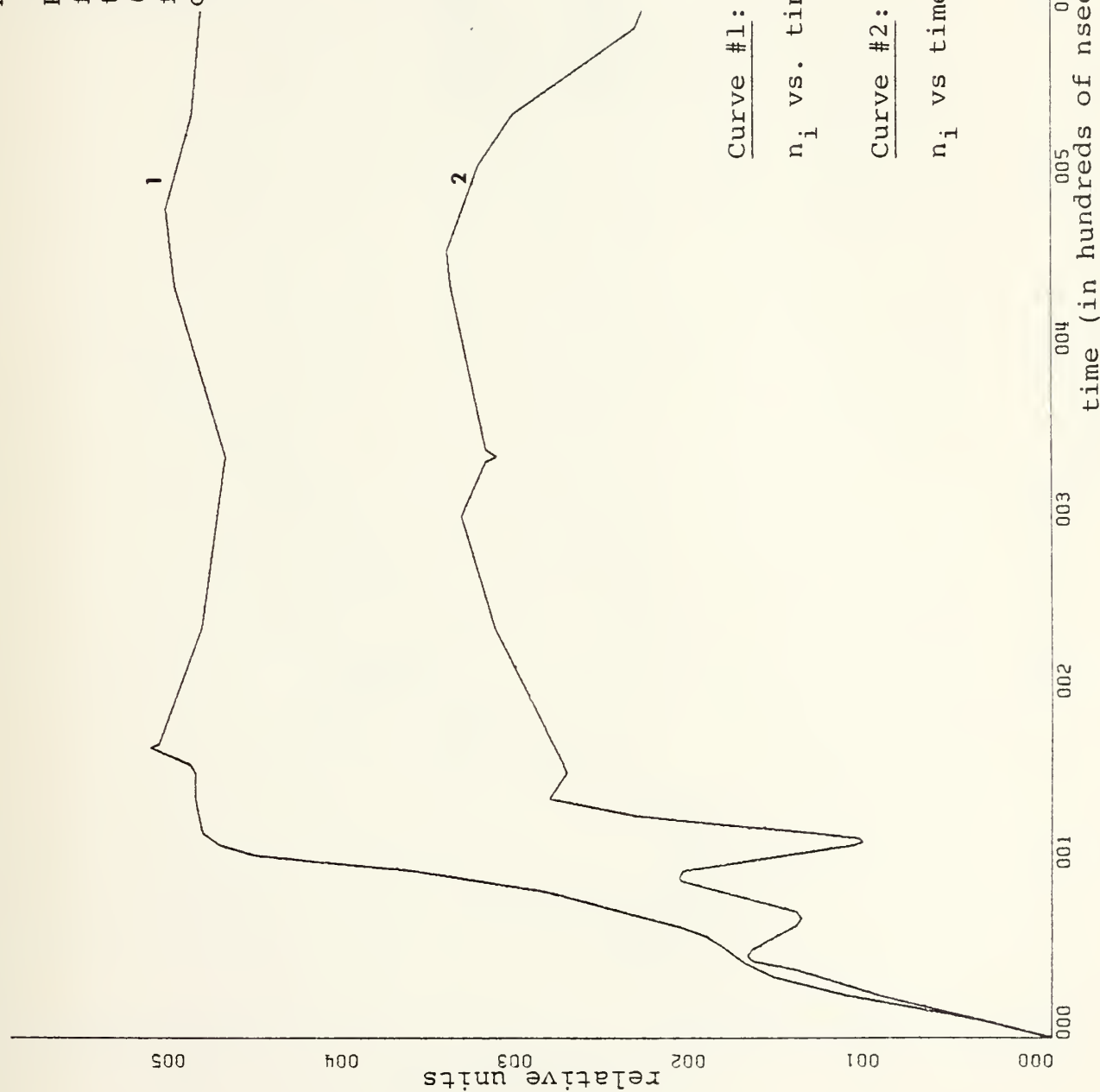
Curve #2:

$n_i$  vs. time, plate at  $z = 7.5$  cm



Figure 17

Plasma density as a function of time at the point  $r = 0.4$  cm,  $\theta = 0^\circ$  and  $z = 1.0$  cm for a background pressure of 0.5 Torr  $H_2$ .



Curve #1:

$n_i$  vs. time, plate at  $z = 1.15$  cm

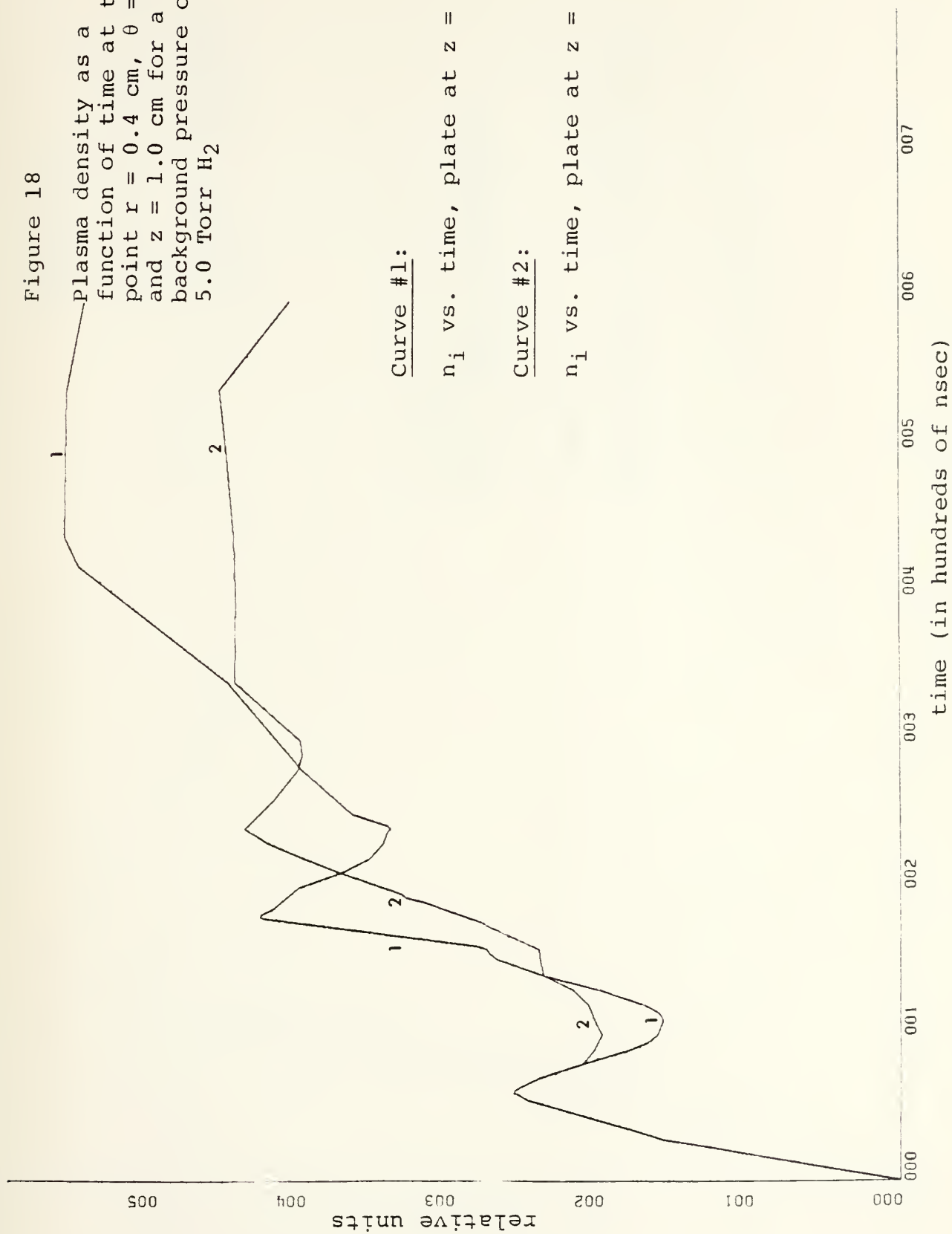
Curve #2:

$n_i$  vs time, plate at  $z = 7.5$  cm



Figure 18

Plasma density as a  
function of time at the  
point  $r = 0.4$  cm,  $\theta = 0^\circ$   
and  $z = 1.0$  cm for a  
background pressure of  
5.0 Torr  $H_2$



Curve #1:

$n_i$  vs. time, plate at  $z = 1.15$  cm

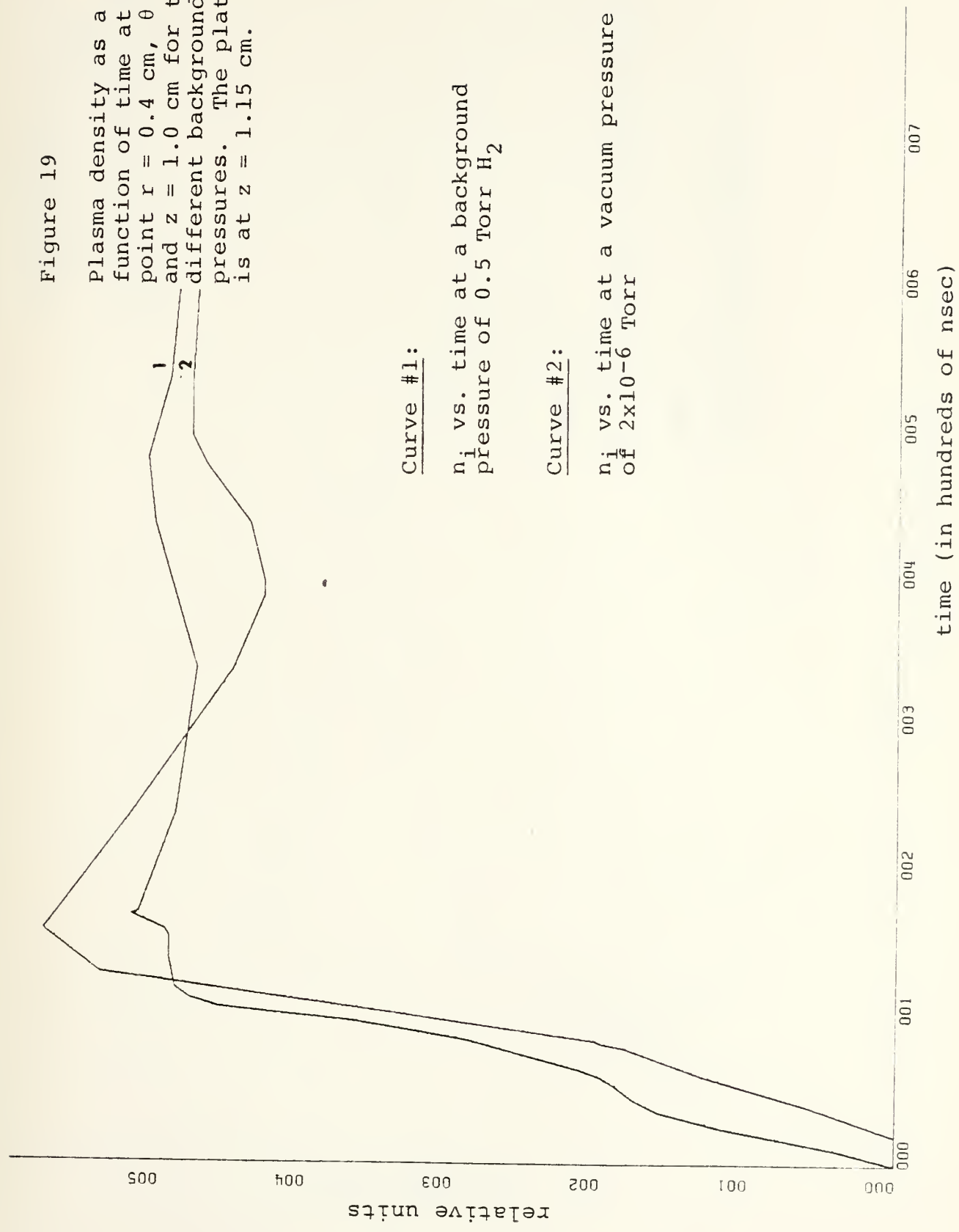
Curve #2:

$n_i$  vs. time, plate at  $z = 7.5$  cm



Figure 19

Plasma density as a function of time at the point  $r = 0.4$  cm,  $\theta = 0^\circ$  and  $z = 1.0$  cm for two different background pressures. The plate is at  $z = 1.15$  cm.



Curve #1:

$n_i$  vs. time at a background pressure of 0.5 Torr H<sub>2</sub>

Curve #2:

$n_i$  vs. time at a vacuum pressure of  $2 \times 10^{-6}$  Torr





Figure 20

Plasma density as a function of time at the point  $r = 0.4$  cm,  $\theta = 0^\circ$  and  $z = 1.0$  cm for two different background pressures. The plate is at  $z = 7.5$  cm.

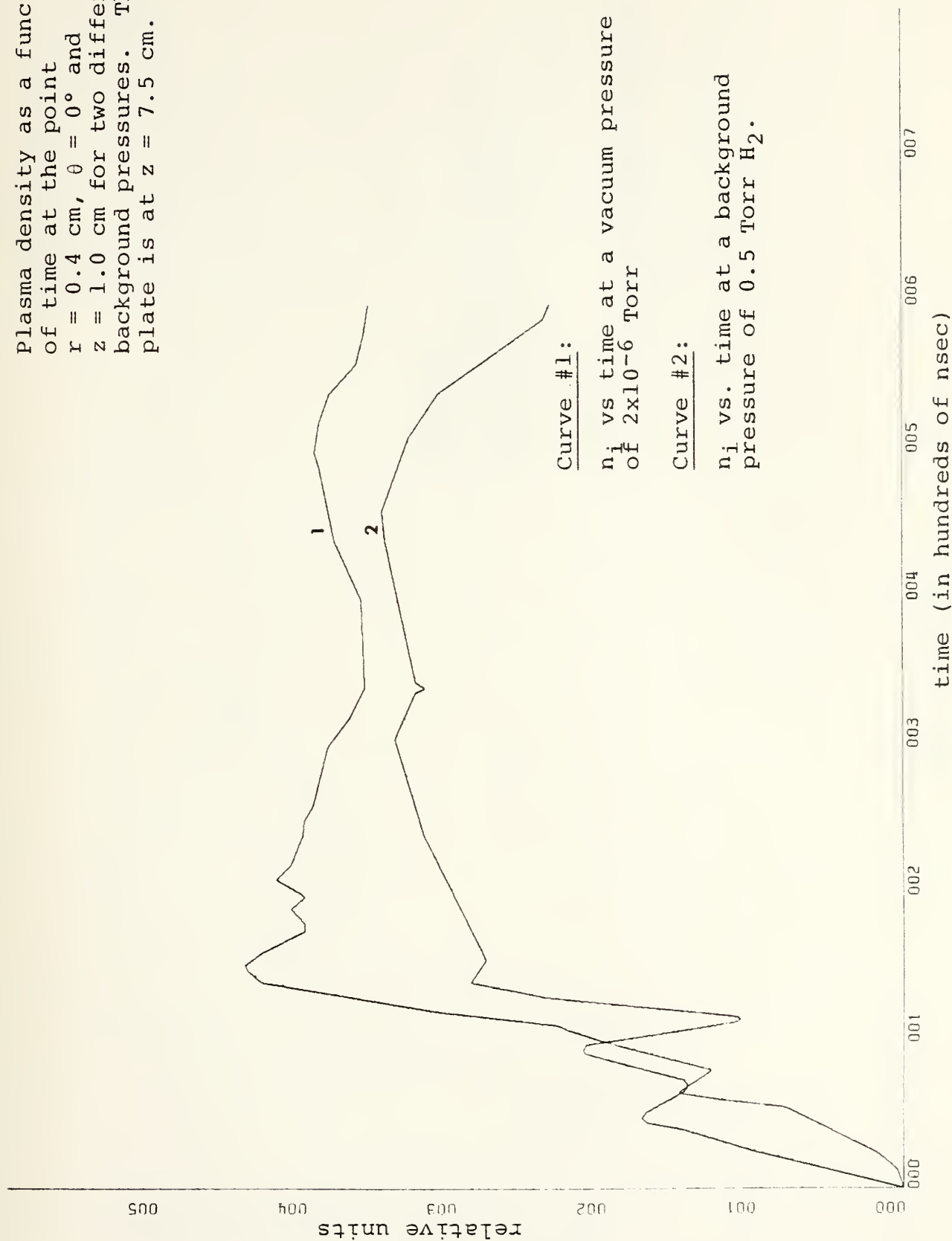




Figure 21

Plasma density as a function of time at the point  $r = 0.4$  cm,  $\theta = 0^\circ$  and  $z = 1.0$  cm for two different background pressures. The plate is at  $z = 1.15$  cm.

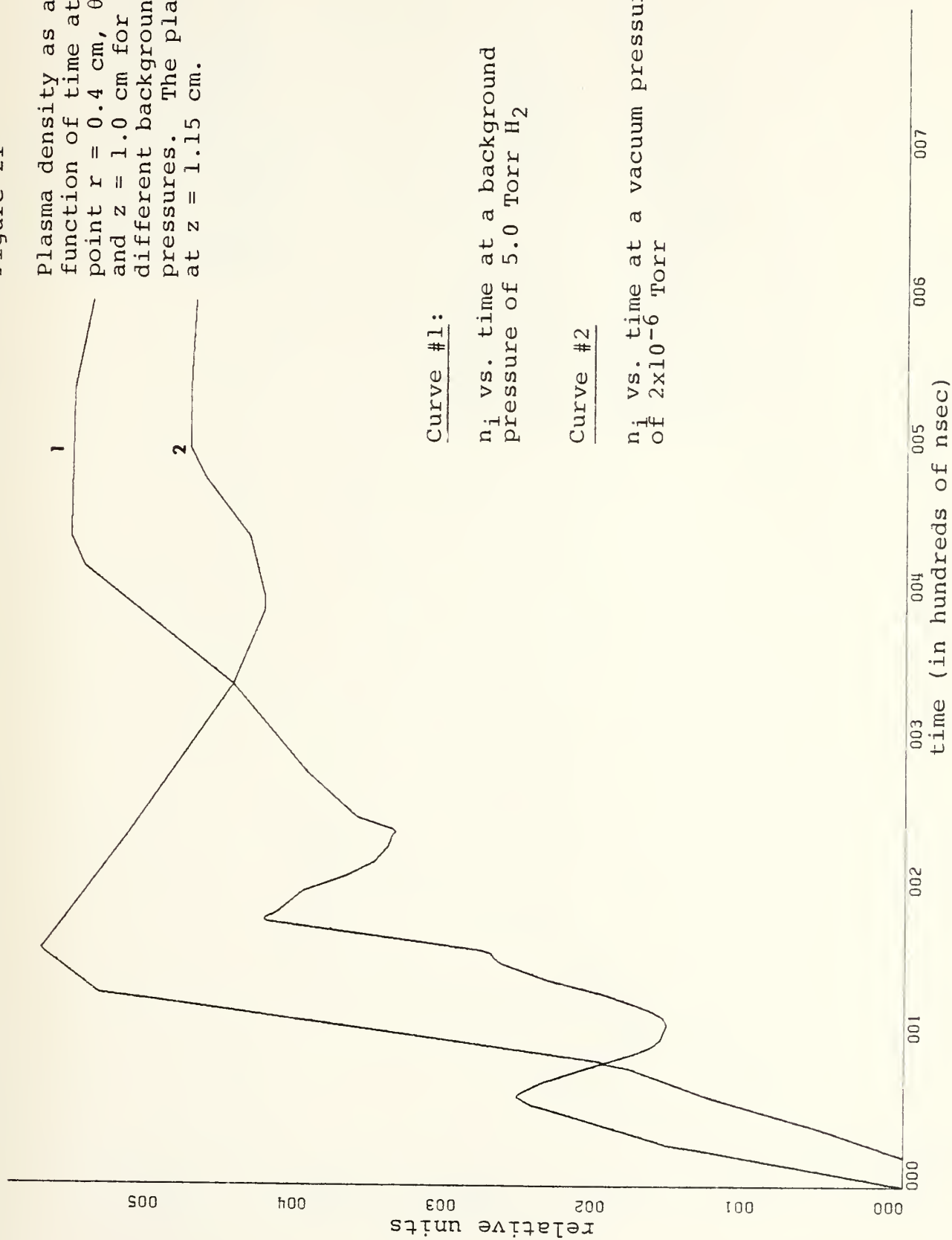




Figure 22

Plasma density as a function of time at the point  $r = 0.4$  cm,  $\theta = 0^\circ$  and  $z = 1.0$  cm for two different background pressures. The plate is at  $z = 7.5$  cm.

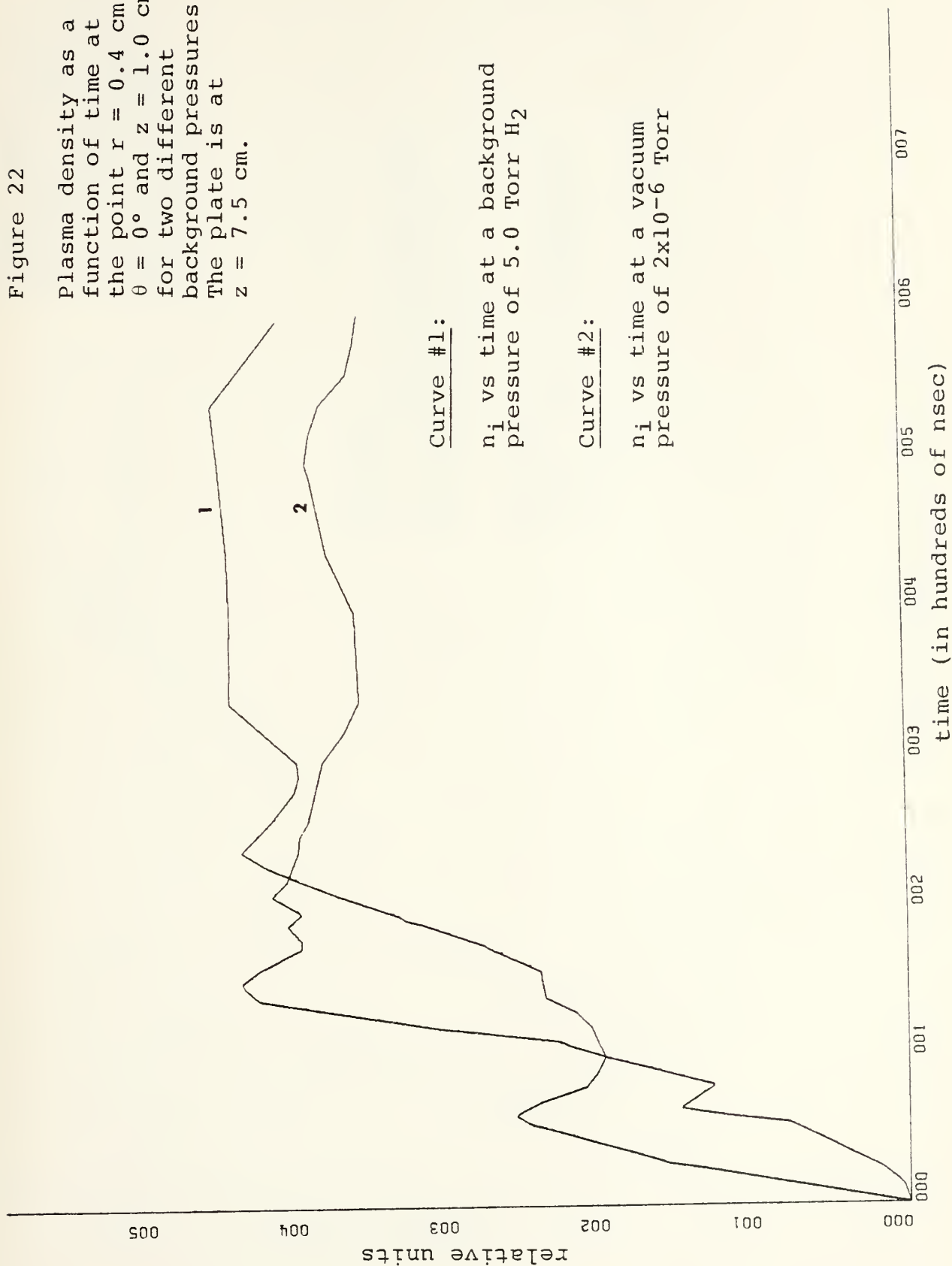




Figure 23

Plasma density as a function of time at the point  $r = 0.4$  cm,  $\theta = 0^\circ$  and  $z = 1.0$  cm for two different background pressures. The plate is at  $z = 1.15$  cm.

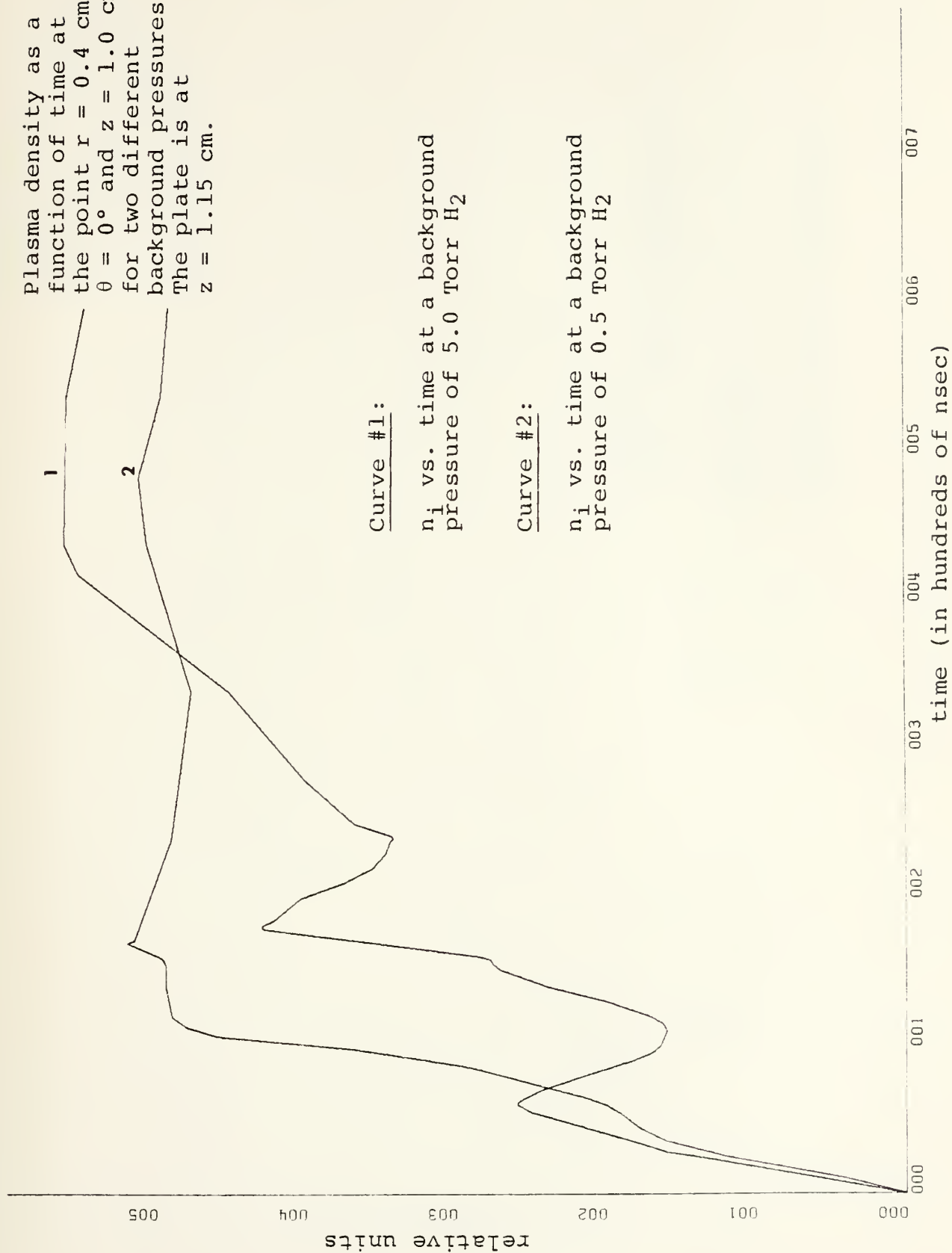






Figure 24

Plasma density as a function of time at the point  $r = 0.4$  cm,  $\theta = 0^\circ$  and  $z = 1.0$  cm for two different background pressures. The plate is at  $z = 7.5$  cm.

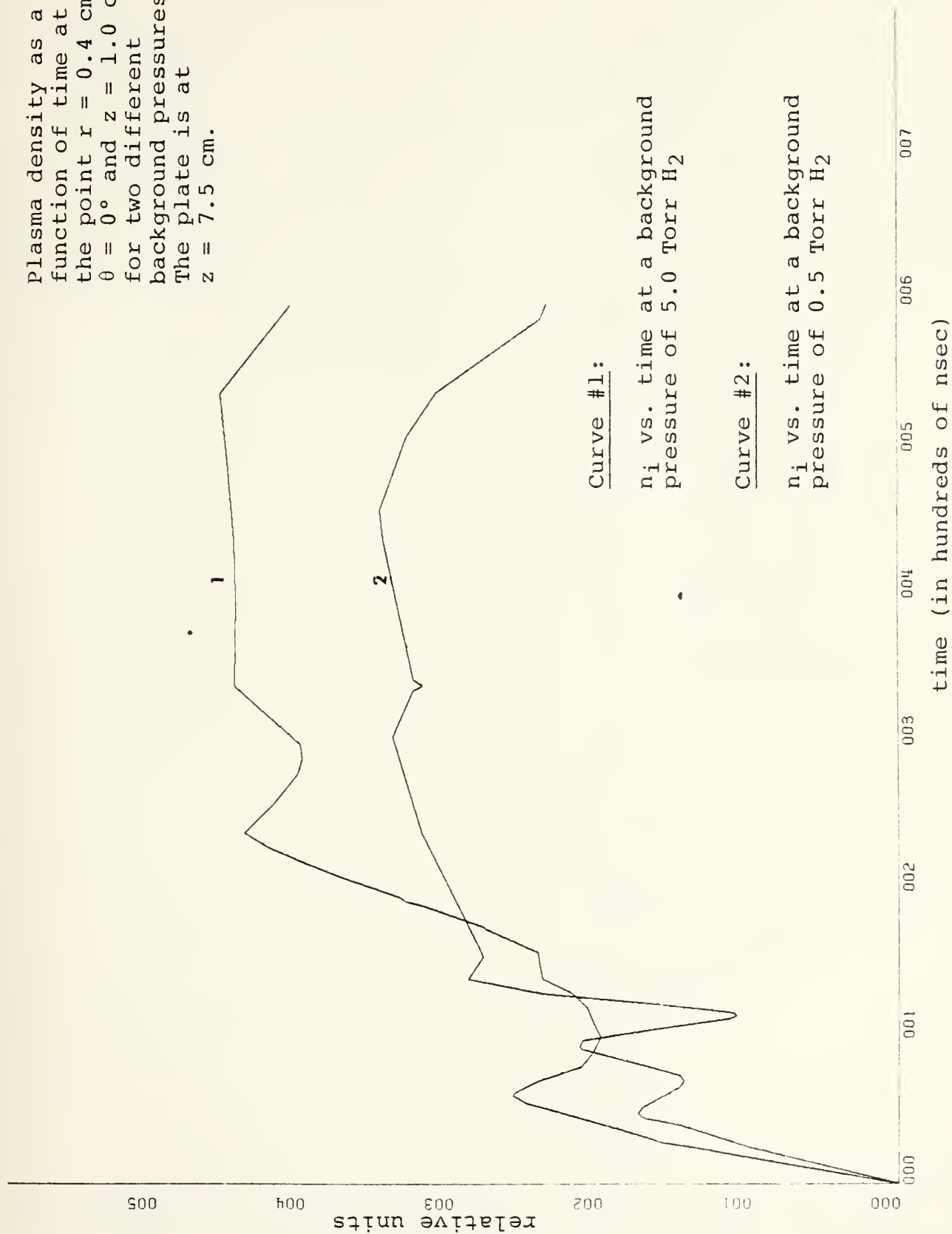




Figure 25

Magnetic Probe Signal  
 $(\partial B / \partial t)$  as a function  
 of time at the point  
 $r = 0.4$  cm,  $\theta = 0^\circ$   
 and  $z = 1.0$  cm for a  
 vacuum pressure of  
 $2 \times 10^{-6}$  Torr

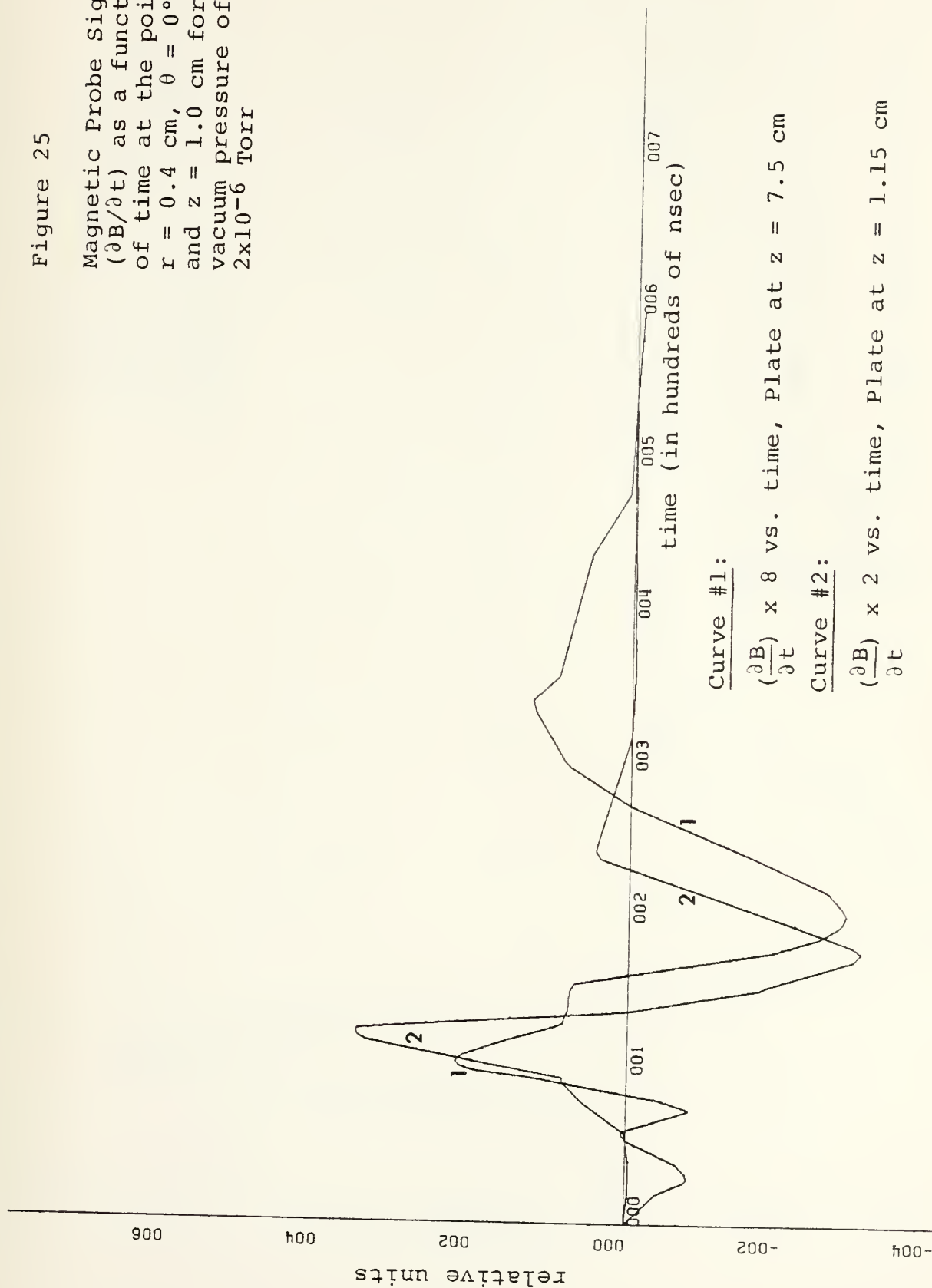




Figure 26

Magnetic probe signal  $(\partial B / \partial t)$  as a function of time at the point  $r = 0.4$  cm,  $\theta = 0^\circ$  and  $z = 1.0$  cm for a background pressure of 0.5 Torr  $H_2$

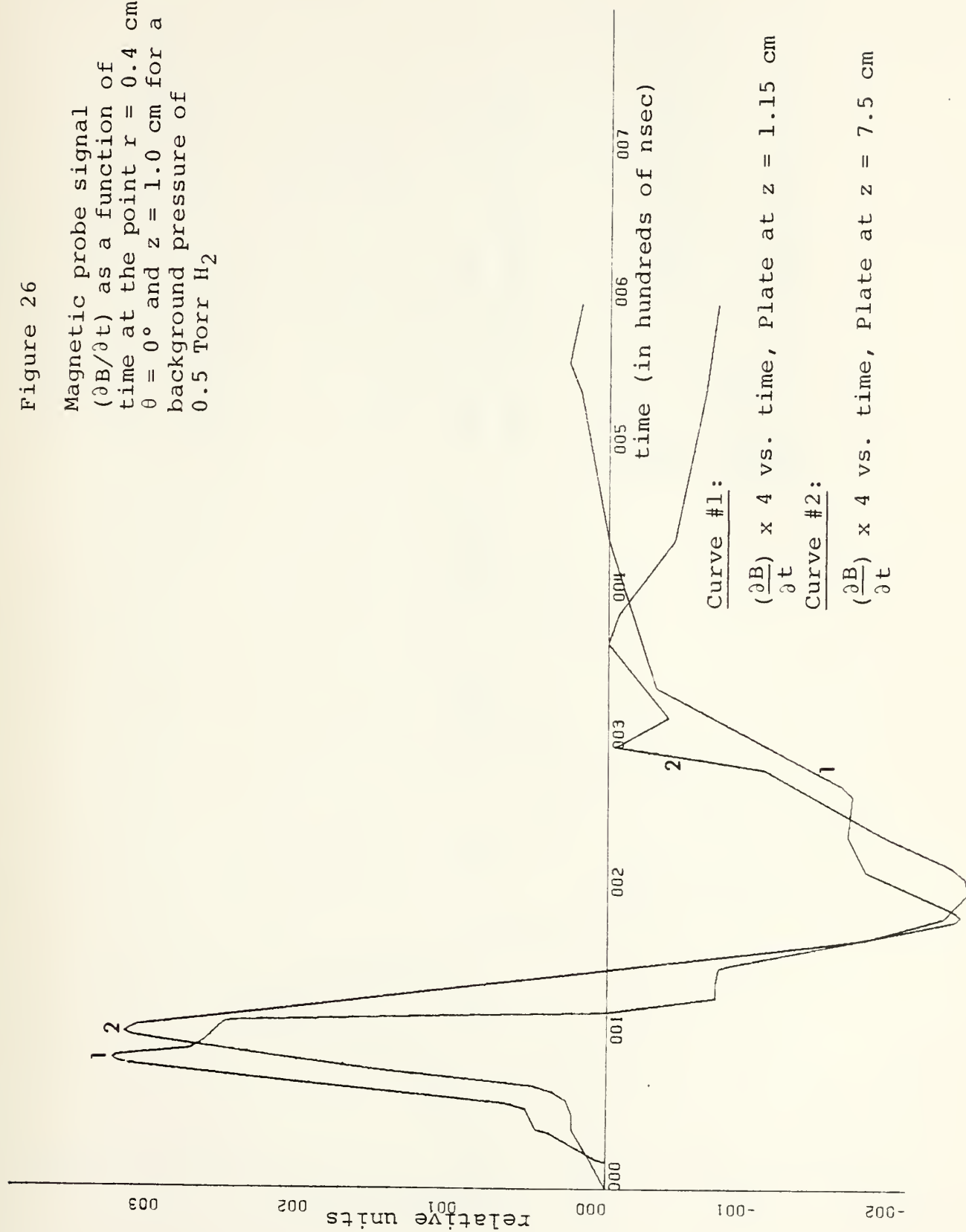




Figure 27

Magnetic probe signal  
 $(\partial B / \partial t)$  as a function of  
time at the point  $r = 0.4$  cm,  
 $\theta = 0^\circ$  and  $z = 1.0$  cm for a  
background pressure of  
5.0 Torr  $H_2$

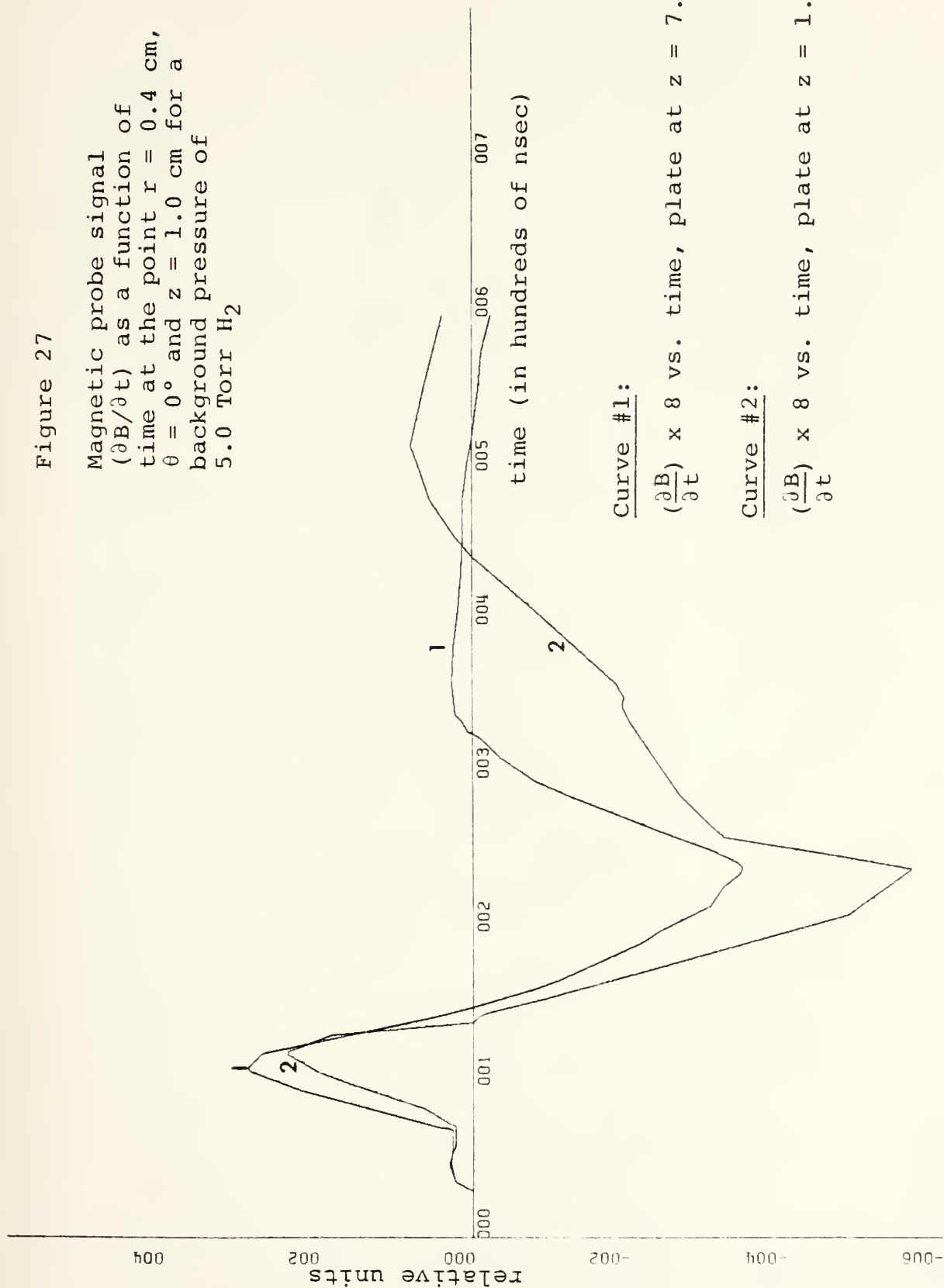






Figure 28

Magnetic field signal ( $B_\theta$ )  
as a function of time at  
the point  $r = 0.4$  cm,  $\theta = 0^\circ$   
and  $z = 1.0$  cm for a  
background pressure of  
5.0 Torr  $H_2$

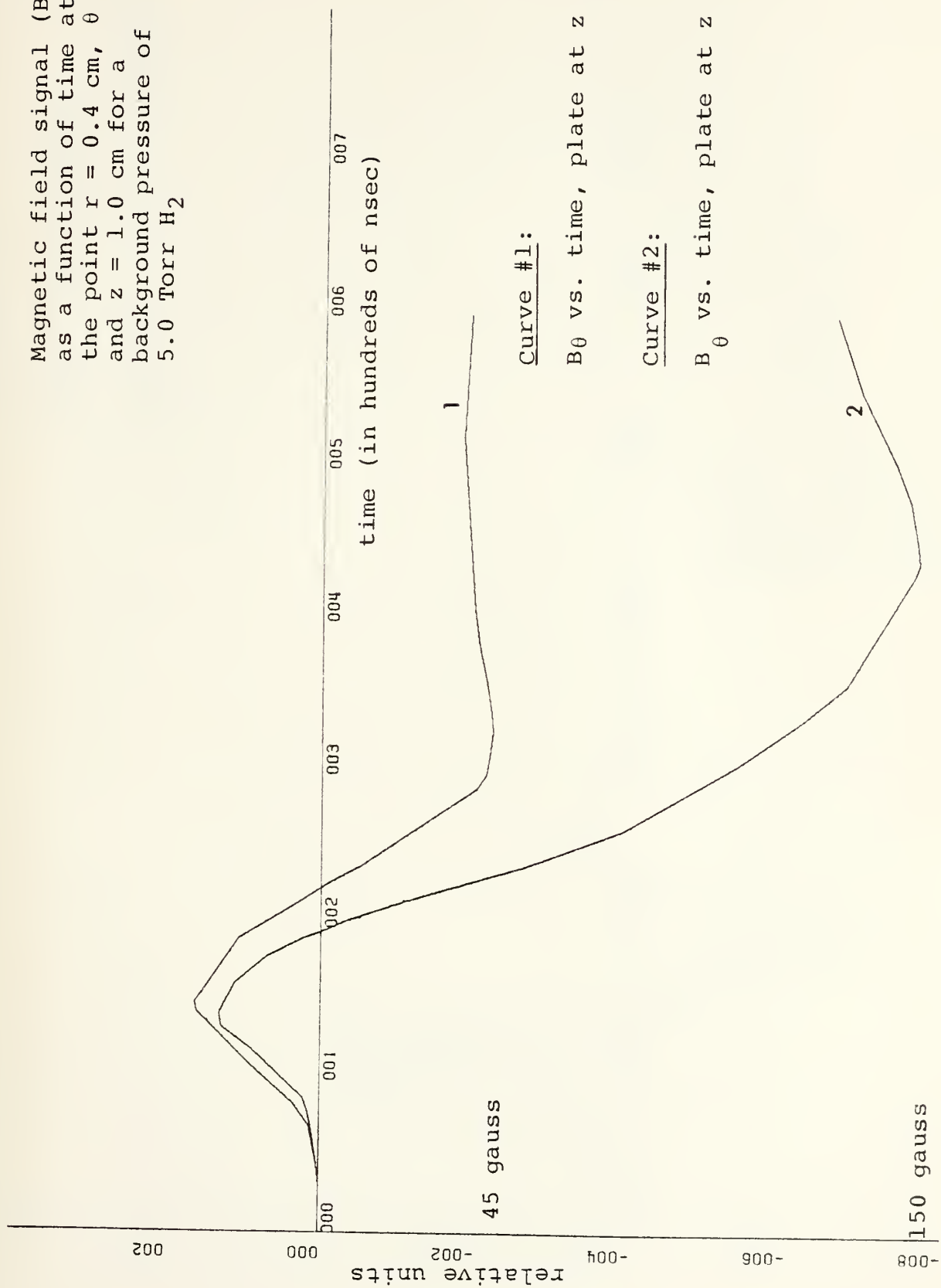




Figure 29

Magnetic probe signal  
 $(\partial B / \partial t)$  as a function  
of time at the point  $r = 0.4$  cm,  
 $\theta = 0^\circ$  and  $z = 1.0$  cm for two  
different background pressures.  
The plate is at  $z = 1.15$  cm.

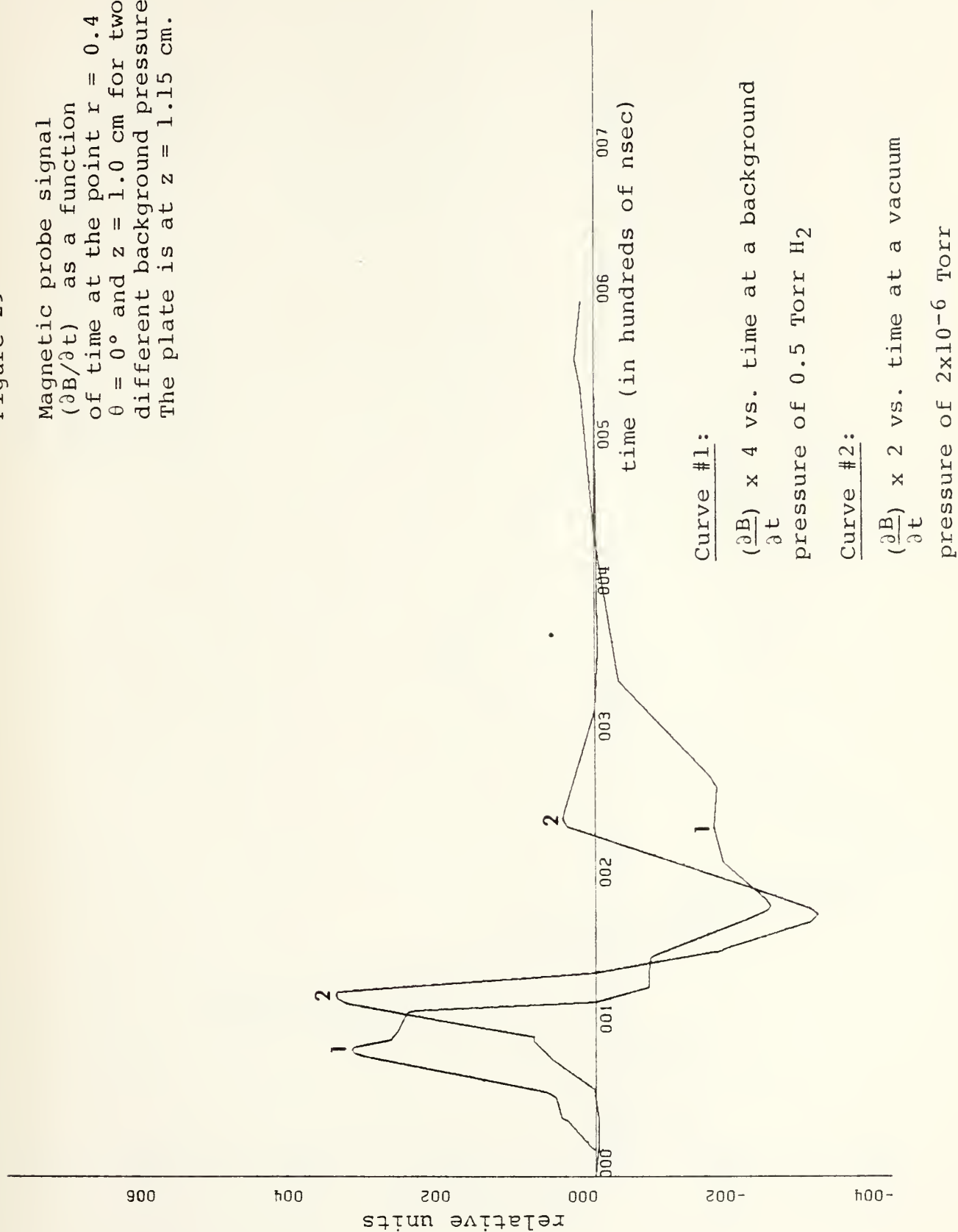




Figure 30

Magnetic probe signal  
 $(\partial B / \partial t)$  as a function of  
 time at the point  $r = 0.4$  cm,  
 $\theta = 0^\circ$  and  $z = 1.0$  cm for two  
 different background pressures.  
 The plate is at  $z = 7.5$  cm

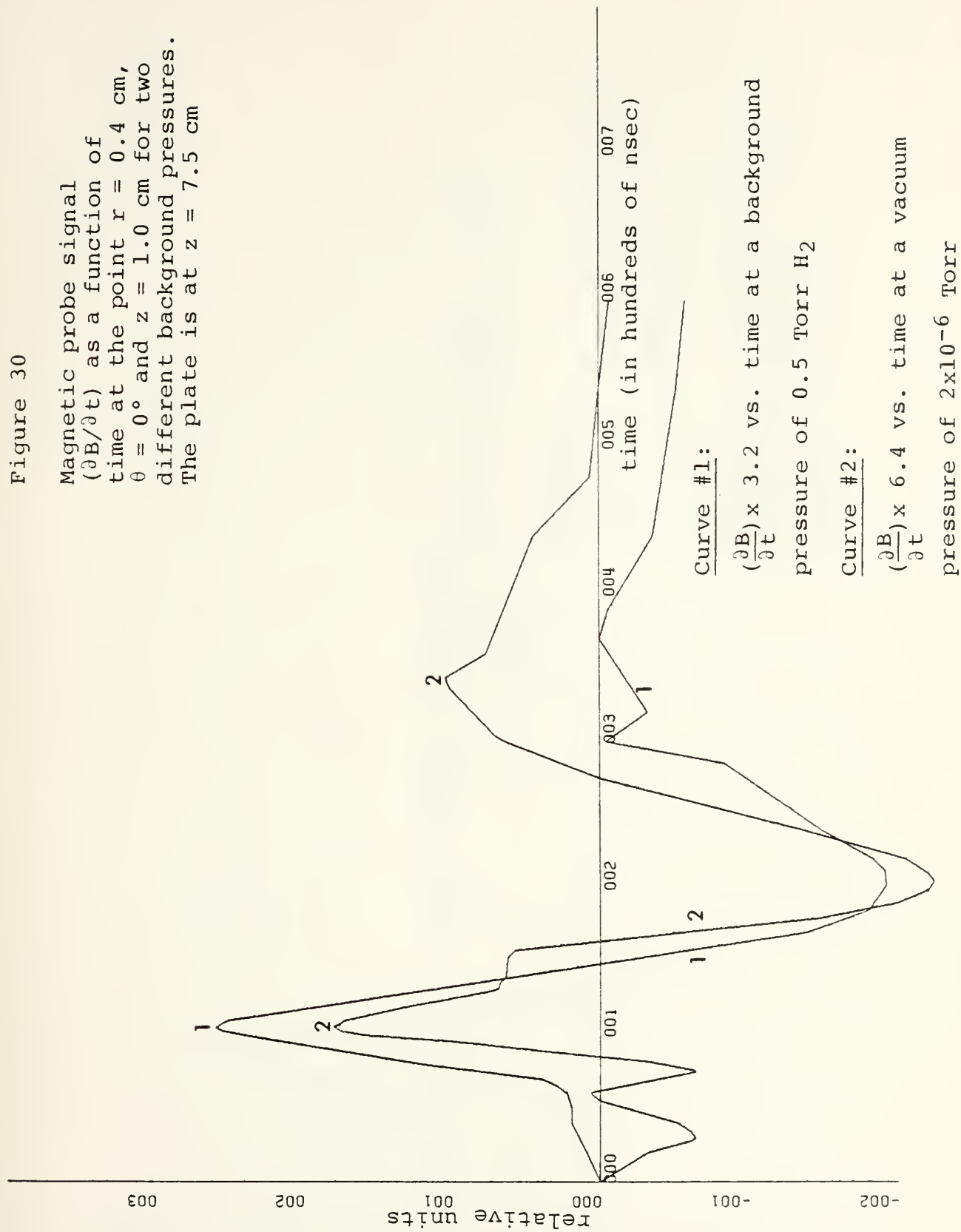




Figure 31

Magnetic probe signal  
 $(\partial B / \partial t)$  as a function of  
time at the point  $r = 0.4$  cm,  
 $\theta = 0^\circ$  and  $z = 1.0$  cm for two  
different background pressures.  
The plate is at  $z = 1.15$  cm.

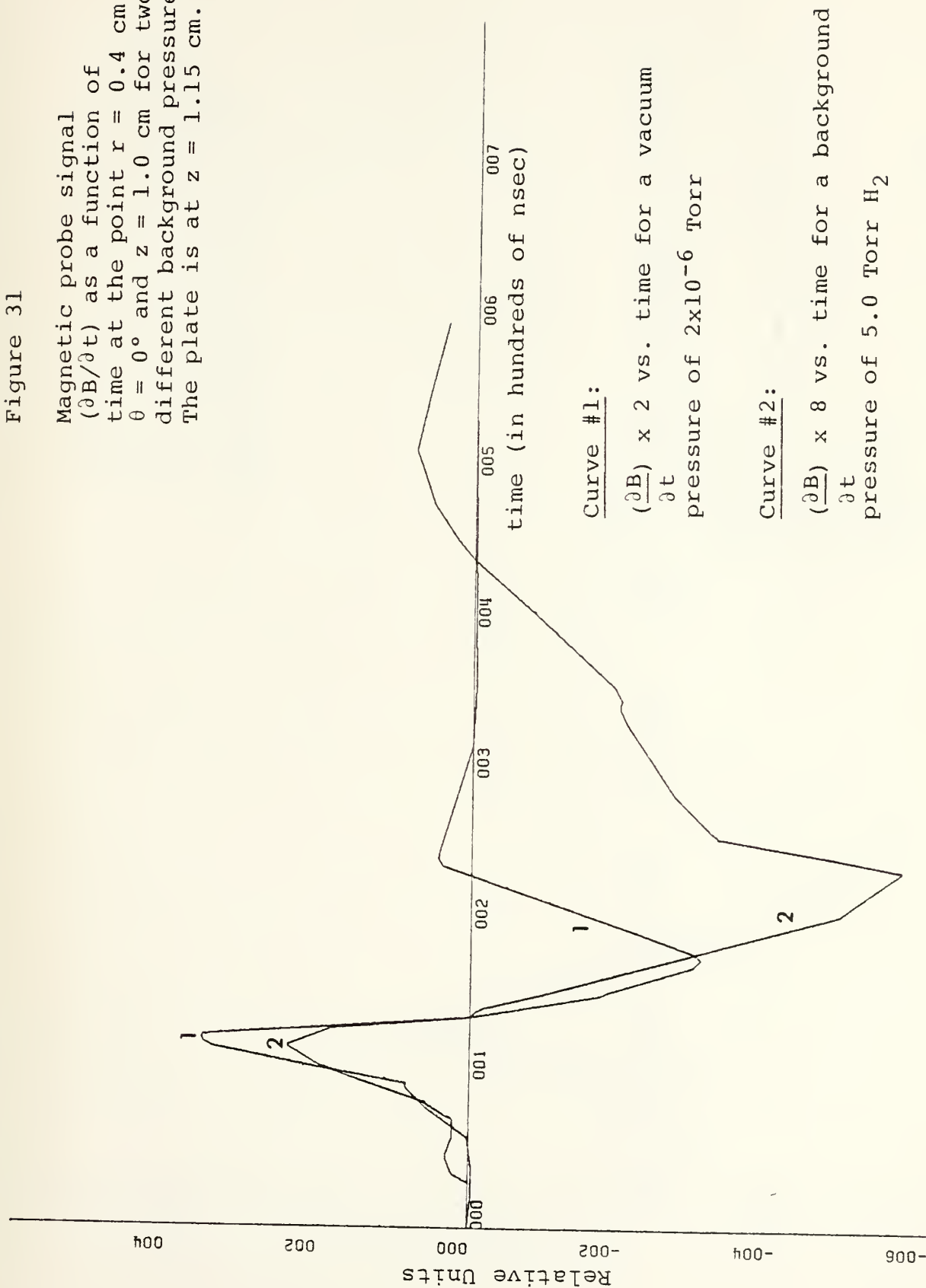






Figure 32

Magnetic probe signal ( $\partial B / \partial t$ ) as a function of time at the point  $r = 0.4$  cm,  $\theta = 0^\circ$  and  $z = 1.0$  cm for two different background pressures. The plate is at  $z = 7.5$  cm

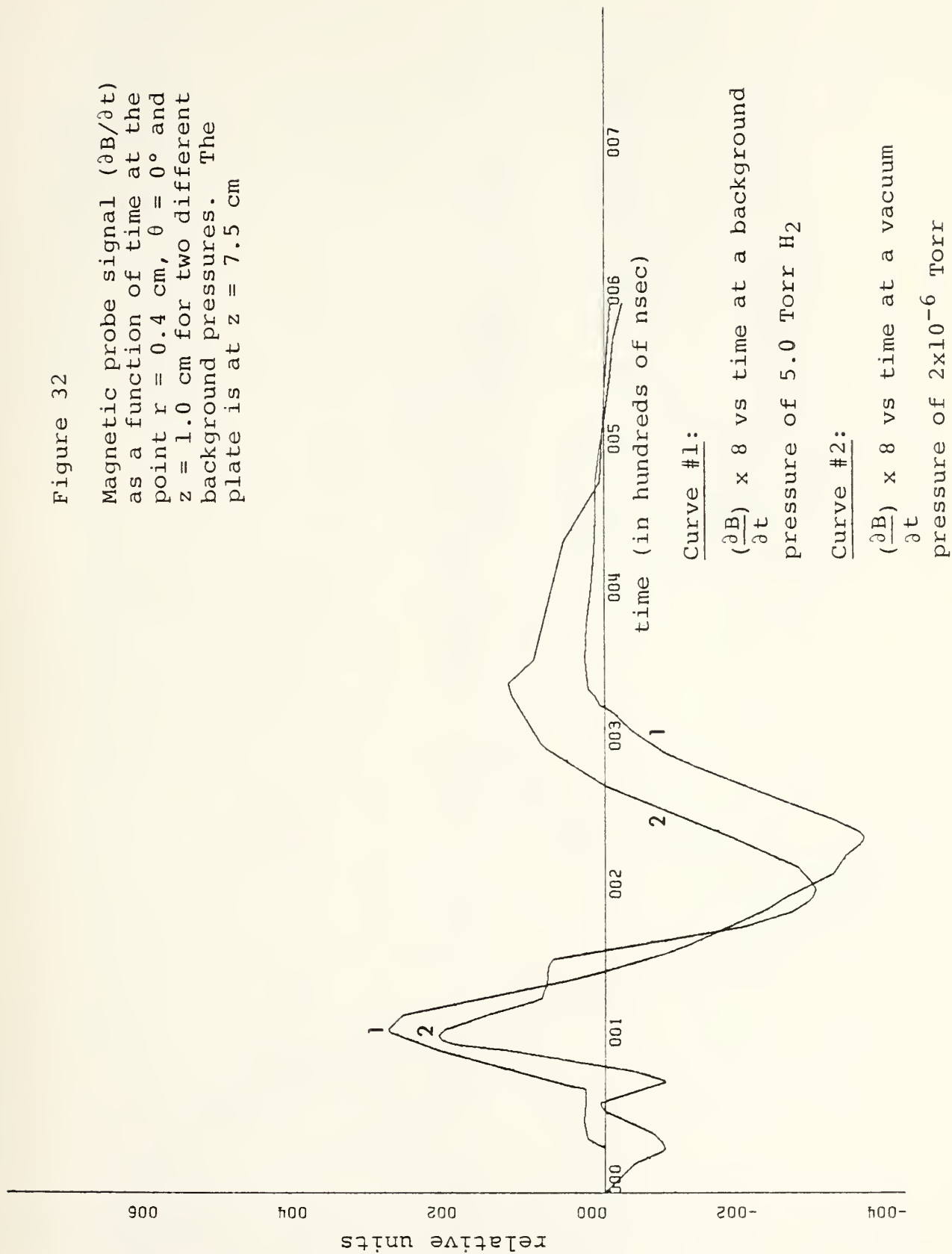




Figure 33

Magnetic probe signal  
 $(\partial B / \partial t)$  as a function of  
time at the point  $r = 0.4$  cm,  
 $\theta = 0^\circ$  and  $z = 1.0$  cm for two  
different background pressures.  
The plate is at  $z = 1.15$  cm.

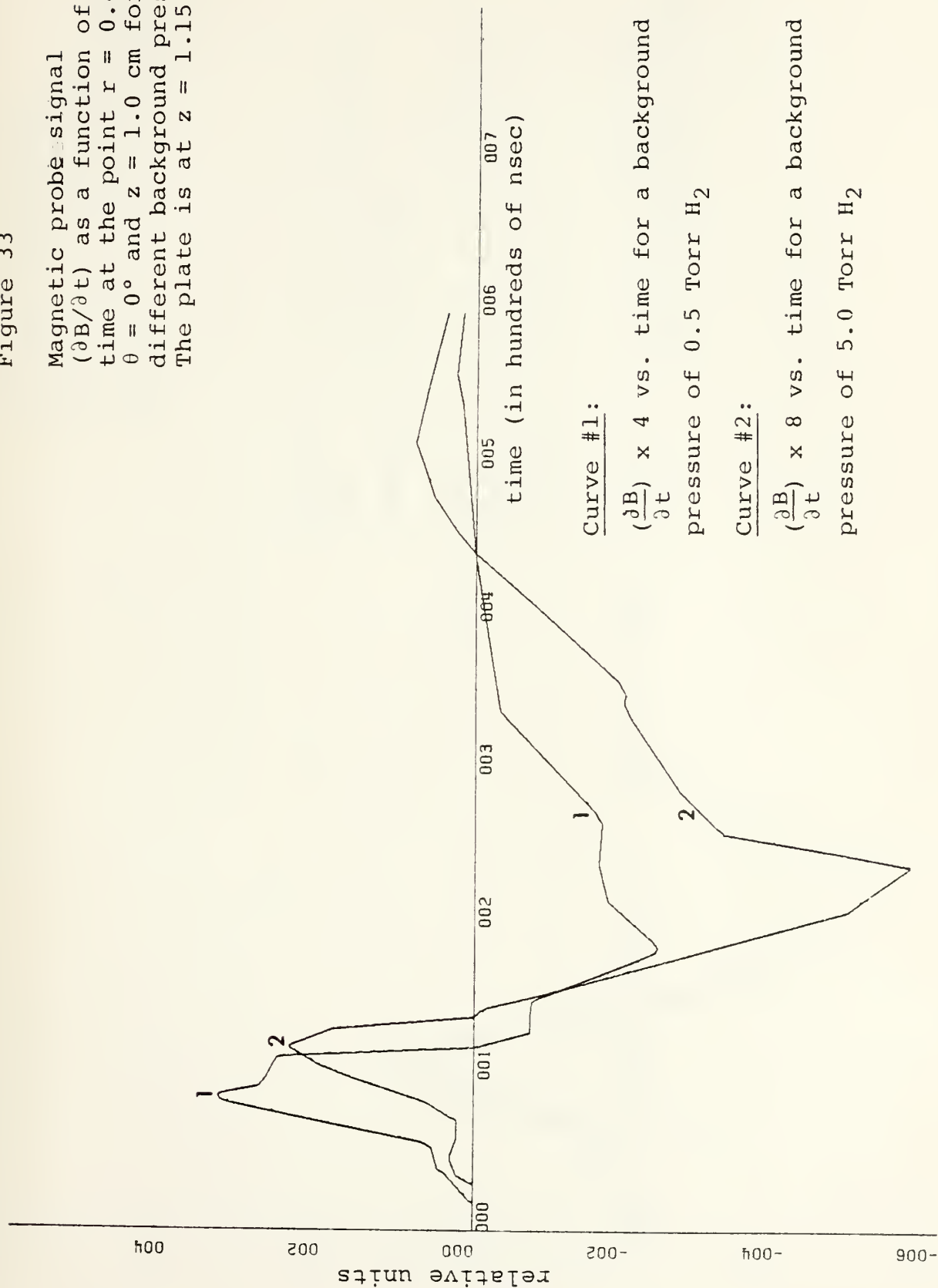




Figure 34

Magnetic probe signal  $(\partial B / \partial t)$  as a function of time at the point  $r = 0.4$  cm,  $\theta = 0^\circ$  and  $z = 1.0$  cm for two different background pressures. The plate is at  $z = 7.5$  cm.

Curve #1:

$(\frac{\partial B}{\partial t}) \times 4$  vs. time at a background pressure of 0.5 Torr  $H_2$

Curve #2:

$(\frac{\partial B}{\partial t}) \times 8$  vs. time at a background pressure of 5.0 Torr  $H_2$

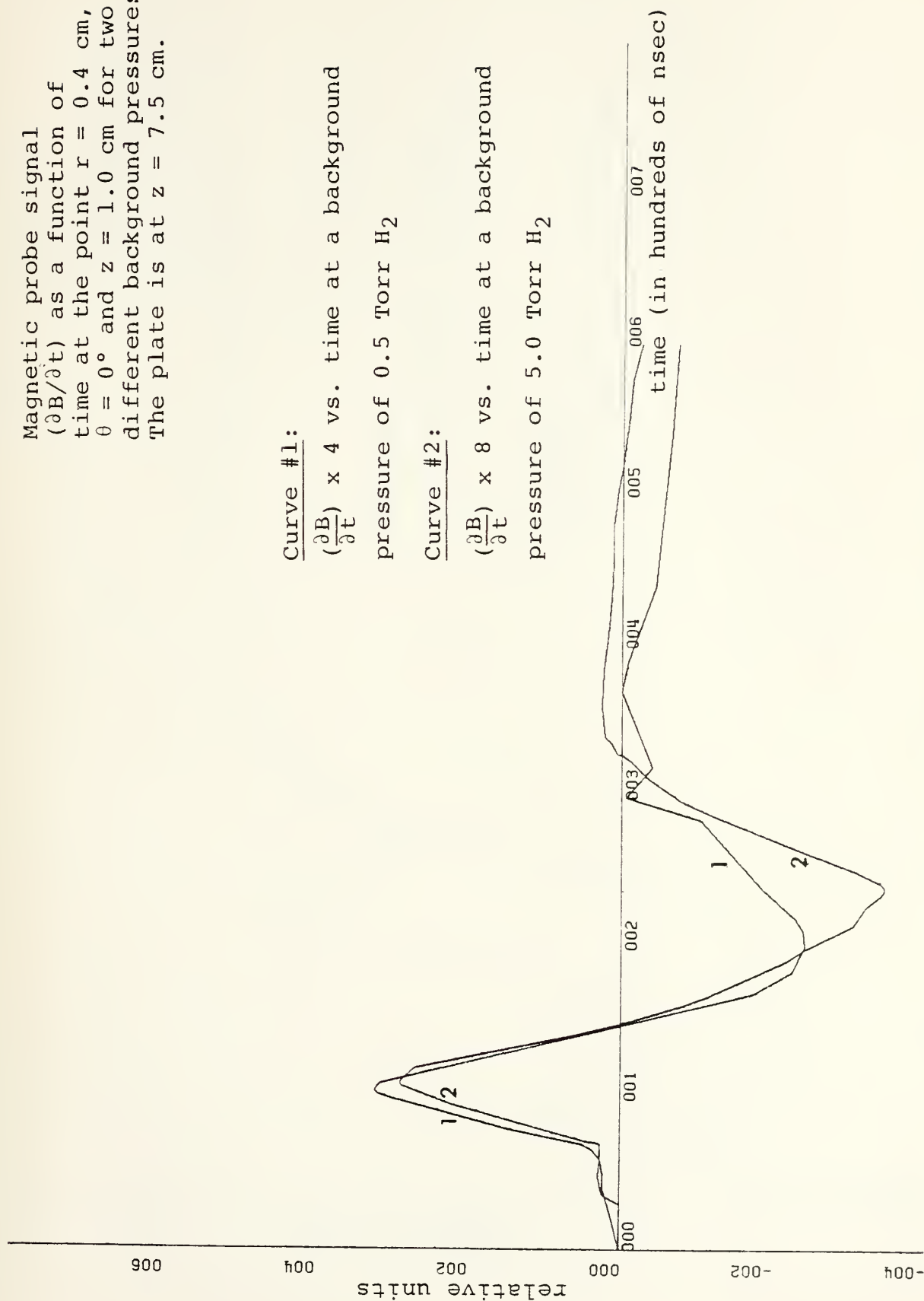
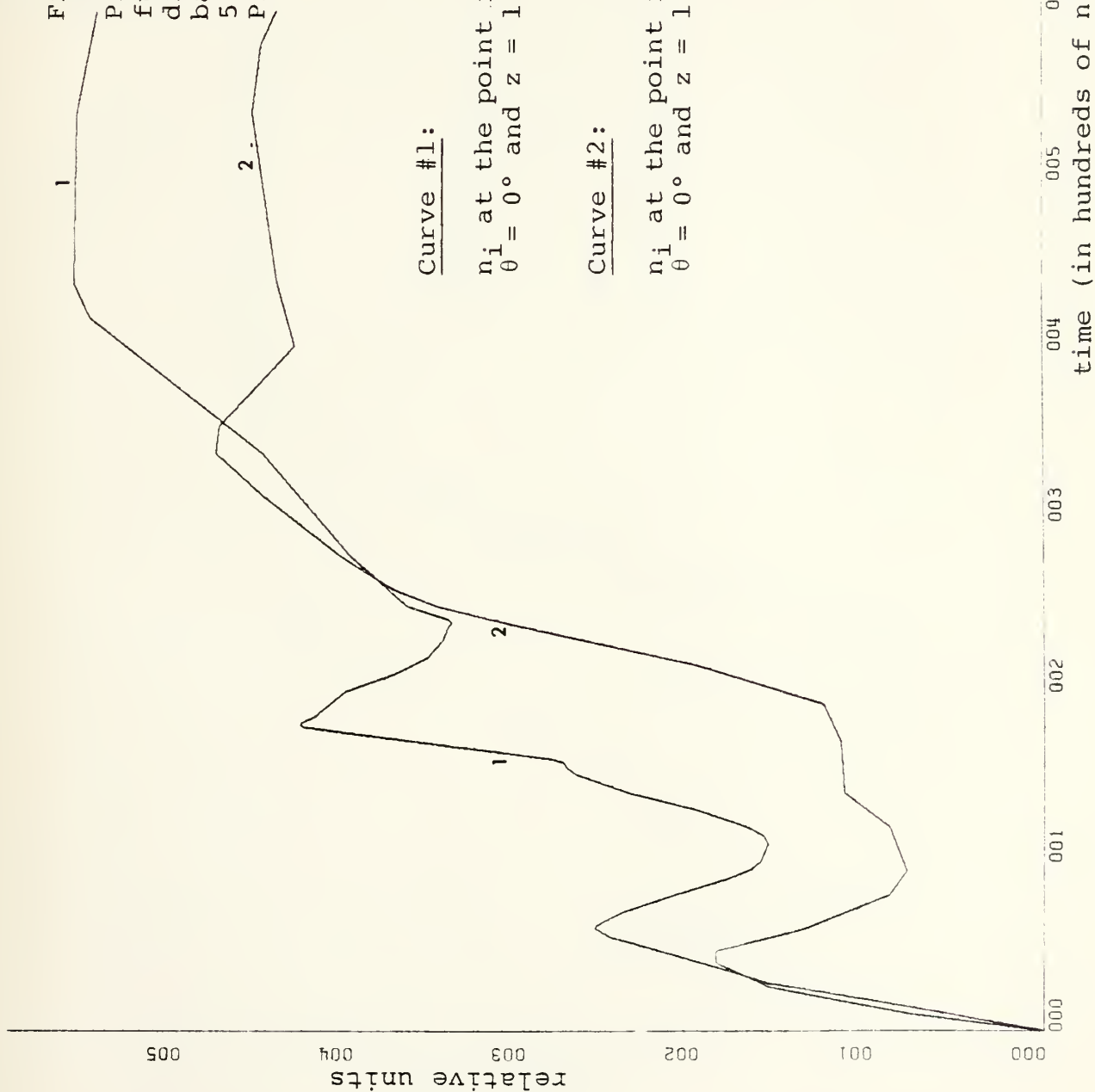




Figure 35

Plasma density as a function of time at two different points for a background pressure of 5.0 Torr H<sub>2</sub>.  
Plate at  $z = 1.15$  cm.



Curve #1:

$n_i$  at the point  $r = 0.4$  cm,  
 $\theta = 0^\circ$  and  $z = 1.0$  cm vs. time

Curve #2:

$n_i$  at the point  $r = 0.8$  cm,  
 $\theta = 0^\circ$  and  $z = 1.0$  cm vs. time





Figure 36

Plasma density as a function of time at two different points for a background pressure of 5.0 Torr  $H_2$ .  
Plate at  $z = 7.5$  cm.

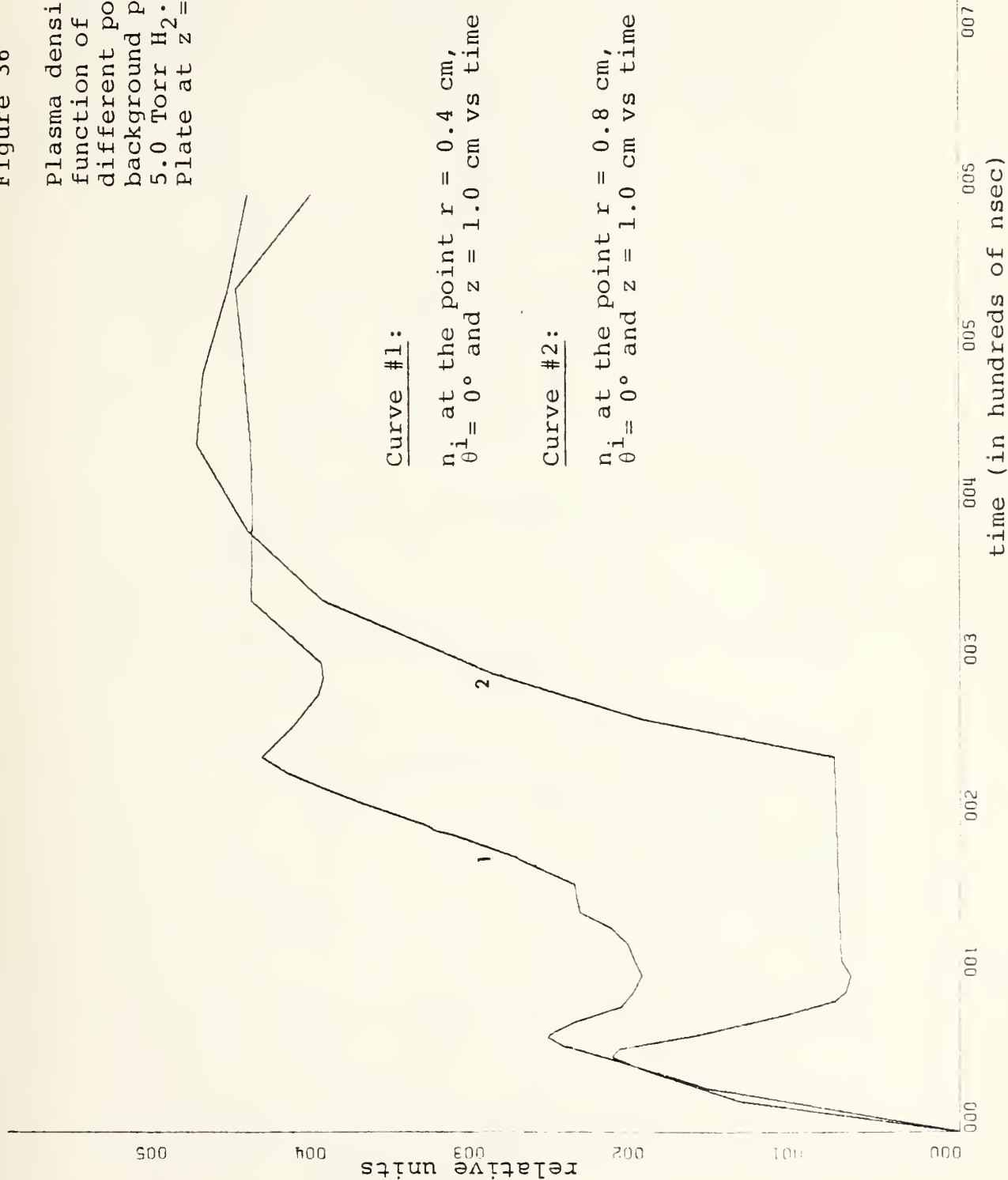
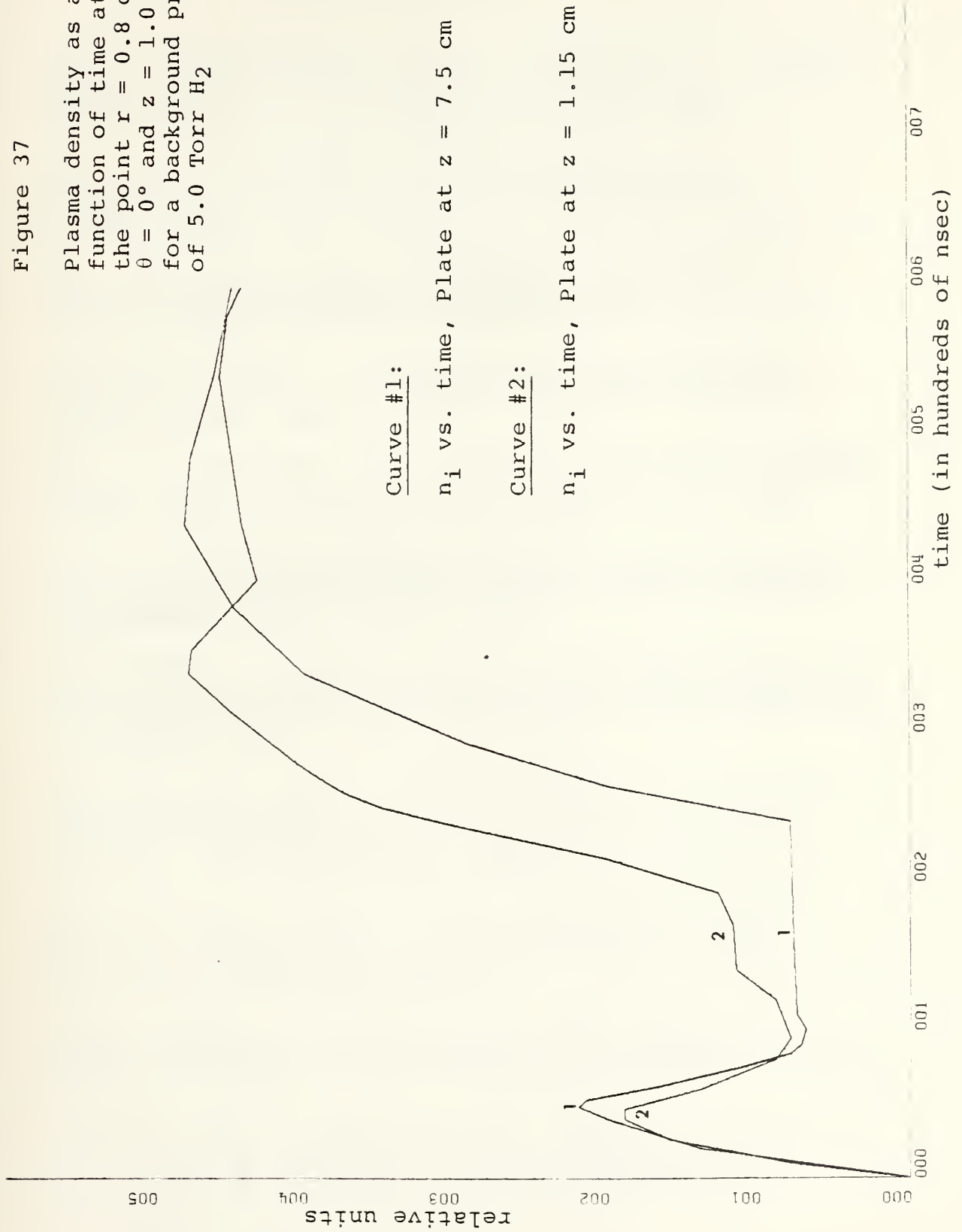




Figure 37

Plasma density as a function of time at the point  $r = 0.8$  cm,  $\theta = 0^\circ$  and  $z = 1.0$  cm for a background pressure of 5.0 Torr  $H_2$





## LIST OF REFERENCES

1. Basov, N.G. and Krokhin, O.N., "The Condition of Plasma Heating by the Optical Generator Radiation," in Quantum Electronics, vol. 3, Grivet, P. and Bloembergen, N., eds., p. 1373, Columbia University Press, 1964.
2. Bobin, J.L. and others, "Shock Wave Generation in Rarefied Gases by Laser Impact on Beryllium Targets," J. Appl. Phys., Vol. 39, No. 9, p. 4184-4189, August 1968.
3. Bird, R.S., The Pressure Dependence of Spontaneous Magnetic Fields in Laser Produced Plasmas, Ph.D. Thesis, Naval Postgraduate School, 1973.
4. Chen, F.F., Chapter in Plasma Diagnostic Techniques, Huddleston, R.H. and Leonard, S.L., eds., p. 178, Academic Press, 1965.
5. Chu, C.K. and Gross, R.A., Chapter in Advances in Plasma Physics, Vol. 2, Simon, A. and Thompson, W.B., eds., p. 139, Interscience Publishers, 1969.
6. Davis, L.J., Self-Generated Magnetic Fields Produced by Laser Bombardment of A Solid Target, MS Thesis, Naval Postgraduate School, 1972.
7. Naval Research Laboratory Report 7301, Demonstration of Collisionless Interactions Between Counterstreaming Ions in a Laser-produced Plasma Experiment, by S.O. Dean, 17 September 1971.
8. Dean, S.O. and others, "Demonstration of Collisionless Interactions Between Interstreaming Ions in a Laser Produced Plasma Experiment," Phys. Rev. Letters, Vol. 27, No. 8, pp. 487-490, 23 August 1971.
9. Dean, S.O. and others, "Reason for the Collisionless Nature of Interactions in a Laser-produced Plasma Experiment," Phys. Rev. Letters, Vol. 29, No. 9, pp. 509-573, 28 August 1972.
10. Everett Research Laboratory Report 363, Collisionless Shocks in Plasmas, by H.W. Friedman and others. December 1970.
11. Friedman, H.W. and Patrick, R.M., "Momentum Transfer in Plasmas at High Alfven Mach Numbers," Phys. Fluids, Vol. 14, No. 9, pp. 1889-1904, September 1971.



12. Hall, R.B., "Laser Production of Blast Waves in Low Pressure Gases," J. Appl. Phys., Vol. 40, No. 4, pp. 1941-1945, March 1969.
13. Hu, P.N., "Structure of a Perpendicular Shock Wave in a Plasma," Phys. Fluids, Vol. 9, No. 1, pp. 89-98, January 1966.
14. Jackson, J.D., Classical Electrodynamics, 2nd edition, p. 473, John Wiley and Sons, Inc., 1975.
15. Jaffrin, M.Y. and Probstein, R.F., "Structure of a Plasma Shock Wave," Phys. Fluids, Vol. 7, No. 10, pp. 1658-1674, October 1964.
16. Koopman, D.W., "Momentum Transfer Interaction of a Laser-produced Plasma with a Low Pressure Background," Phys. Fluids, V. 15, No. 11, pp. 1959-1968, November 1972.
17. Koopman, D.W. and Tidman, D.A., "Possible Observations of Collisionless Electrostatic Shocks in Laser-produced Plasmas," Phys. Rev. Letters, V. 18, No. 14, pp. 533-535, 3 April 1967.
18. McKee, L.L., An Investigation of the Self-Generated Magnetic Fields Associated with a Laser-Produced Plasma, Ph.D. Thesis, Naval Postgraduate School, 1972.
19. McLaughlin, T.A., Inductive Magnetic Probe Diagnostics in a Plasma, MS Thesis, Naval Postgraduate School, 1970.
20. Ready, J.F., Effects of High-Power Laser Radiation, pp. 109-116 and 161-207, Academic Press, 1971.
21. Schwirzke, F., Chapter in Laser Interactions and Related Plasma Phenomena, Schwarz, H.J. and Hora, H. Eds. P. 213. Plenum Press, 1974.
22. Schwirzke, F. and McKee, L.L., Chapter in V European Conference on Controlled Fusion and Plasma Physics, Grenoble (1972), V. 1, p. 63. Grenoble Ass. Euratom-CEA, 1972.
23. Spitzer, L., Jr., Physics of Fully Ionized Gases, 2nd Edition, Interscience Publishers, Inc., 1962.
24. Stamper, J.A. and others, "Spontaneous Magnetic Fields in Laser-Produced Plasmas," Phys. Rev. Letters, V. 26, No. 17, Pp. 1012-1015, 26 April 1971.
25. Stamper, J.A. and others, "Studies of Spontaneous Magnetic Fields in Laser-Produced Plasmas by Faraday Rotation," Phys. Rev. Letters, V. 40, No. 18, pp. 1177-1181, 1 May 1978.





26. Naval Research Laboratory Report 7411 Laser-Induced Sources for Magnetic Fields, by J.A. Stamper, 16 June 1972.
27. Stamper, J.A. and others, Chapter in Laser Interactions and Related Plasma Phenomena, Schwarz, H.J. and Hora, H., eds. V. 2, p. 273, Plenum Press, 1972.
28. Tanenbaum, B.S., Plasma Physics, P. 348, McGraw-Hill, 1967.
29. Tidman, D.A. and Krall, N.A., Shock Waves in Collisionless Plasmas, P. 14, Wiley-Interscience, 1971.
30. Widner, M.M., "Self-Generated Magnetic Fields in Laser Plasmas," to be published.
31. Wright, T.P. and Widner, N.M., "Some Geometrical Effects on the Source of Spontaneous Laser Generated Magnetic Fields," Bull. Am. Phys. Soc., V. 17, P. 1027, 1972.
32. Wright, T.P., "Comments on a Demonstration of Collisionless Interactions Between Interstreaming Ions in a Laser-Produced-Plasma Experiment," Phys. Rev. Letters, V. 28, No. 5, Pp. 268-270, 31 January 1972.
33. Zel'dovich, Y.B. and Raizer, Y.P., Physics of Shock Waves and High-Temperature Hydrodynamic Phenomena, Vol. II, P. 515. Academic Press, 1967.



INITIAL DISTRIBUTION LIST

	No. Copies
1. Defense Documentation Center Cameron Station Alexandria, Virginia 22314	2
2. Library, Code 0142 Naval Postgraduate School Monterey, California 93940	2
3. Chairman, Code 61 Department of Physics and Chemistry Naval Postgraduate School Monterey, California 93940	2
4. Prof. F. Schwirzke, Code 61Sw Department of Physics and Chemistry Naval Postgraduate School Monterey, California 93940	3
5. Professor A. W. Cooper, Code 61Cr Department of Physics and Chemistry Naval Postgraduate School Monterey, California 93940	1
6. Lt. Cem Y. Parlar Göztepe, Kadiraga Sok. Barış Apt. No: 2/1 Daire 2 ISTANBUL- TURKEY	2
7. Deniz Kuvvetleri Komutanlığı Eğitim Şube Bşk. lığı ANKARA - TURKEY	5
8. Deniz Harp Ok. K. Ligi Eğitim şube Bşk. lığı Heybeliada - ISTANBUL TURKEY	1
9. Istanbul Teknik Üniversitesi Fizik Bölümü Kütüphanesi ISTANBUL - TURKEY	1
10. Orta Doğu Teknik Üniversitesi Fizik Bölümü Kütüphanesi ANKARA - TURKEY	1













780151

Thesis  
P185  
c.1

Parlar

Self generated mag-  
netic fields in laser-  
produced shock waves.

780151

Thesis  
P185  
c.1

Parlar

Self generated mag-  
netic fields in laser-  
produced shock waves.

thesP185

Self generated magnetic fields in laser-



3 2768 001 98037 8

DUDLEY KNOX LIBRARY